# THEORETICAL MODELING OF ULTRAFAST OPTICAL-FIELD INDUCED PHOTOELECTRON EMISSION FROM BIASED METAL SURFACES

By

Yi Luo

# A DISSERTATION

Submitted to
Michigan State University
in partial fulfillment of the requirements
for the degree of

Electrical Engineering-Doctor of Philosophy

2021

#### **ABSTRACT**

# THEORETICAL MODELING OF ULTRAFAST OPTICAL-FIELD INDUCED PHOTOELECTRON EMISSION FROM BIASED METAL SURFACES

Bv

#### Yi Luo

Laser-induced electron emission from nanostructures offers a platform to coherently control electron dynamics in ultrashort spatiotemporal scales, making it important to both fundamental research and a broad range of applications, such as to ultrafast electron microscopy, diffraction, attosecond electronics, strong-field nano-optics, tabletop particle accelerators, free electron lasers, and novel nanoscale vacuum devices. This thesis analytically studies nonlinear ultrafast photoelectron emission from biased metal surfaces, by solving the time-dependent Schrödinger equation exactly. Our study provides better understanding of the ultrafast control of electrons and offers useful guidance for the future design of ultrafast nanoelectronics.

First, we present an analytical model for photoemission driven by two-color laser fields. We study the electron energy spectra and emission current modulation under various laser intensities, frequencies, and relative phase between the two lasers. We find strong modulation for both the energy spectra and emission current (with a modulation depth up to 99%) due to the interference effect of the two-color lasers. Using the same input parameter, our theoretical prediction for the photoemission current modulation depth (93.9%) is almost identical to the experimental measurement (94%).

Next, to investigate the role of dc field, we construct an analytical model for two-color laser induced photoemission from dc biased metal surfaces. We systematically examine the combined effects of a dc electric field and two-color laser fields. We find the strong modulation in two-color photoemission persists even with a strong dc electric field. In addition, the dc field opens up more

tunneling emission channels and thus increases the total emission current. Application of our model to time-resolved photoelectron spectroscopy is also demonstrated, showing the dynamics of the *n*-photon excited states depends strongly on the applied dc field.

We then propose to utilize two lasers of the same frequency to achieve the interference modulation of photoemission by their relative phase. This is motivated by the easier access to single-frequency laser pairs than two-color lasers in experiments. We find a strong current modulation (> 90%) can be achieved with a moderate ratio of the laser fields (< 0.4) even under a strong dc bias. Our study demonstrates the capability of measuring the time-resolved photoelectron energy spectra using single-frequency laser pairs.

We further extend our exact analytic model to photoelectron emission induced by few-cycle laser pulses. The single formulation is valid from photon-driven electron emission in low intensity optical fields to field-driven emission in high intensity optical fields, and is valid for arbitrary pulse length from sub-cycle to CW excitation, and for arbitrary pulse repetition rate. We find the emitted charge per pulse oscillatorily increases with pulse repetition rate, due to varying coherent interaction of neighboring laser pulses. For a well-separated single pulse, our results recover the experimentally observed vanishing carrier-envelope phase sensitivity in the optical-field regime. We also find that applying a large dc field to the photoemitter is able to greatly enhance the photoemission current and in the meantime substantially shorten the current pulse.

Finally, we construct analytical models for nonlinear photoelectron emission in a nanoscale metal-vacuum-metal gap. Our results reveal the energy redistribution of photoelectrons across the two interfaces between the gap and the metals. Additionally, we find that decreasing the gap distance tends to extend the multiphoton regime to higher laser intensity. The effect of dc bias is also studied in detail.

Copyright by YI LUO 2021

#### **ACKNOWLEDGMENTS**

First, I would like to express my appreciation to my advisor, Prof. Peng Zhang. During my four-year Ph.D. study at Michigan State University, Prof. Zhang provided me with continuous encouragement and support. His expertise and generous guidance helped me achieve my professional and personal growth during this journey.

Secondly, I wish to thank my thesis committee members: Prof. Qi Hua Fan, Prof. Chong-Yu Ruan and Prof. John Albretch, and I also wish to thank Prof. John Verboncoeur, Dr. John Luginsland and Prof. Sergey Baryshev. Their insightful comments make my research work greatly improved.

Thirdly, I would like to express my thank to my colleagues: Dr. Yangyang Fu, Dr. Deqi Wen, Dr. Patrick Wong, Dr. Sneha Banerjee, Dr. Asif Iqbal, Janez Krek and Yang Zhou, and friends who I met, for their help, support, and contribution. I also would like to acknowledge the support from the funding agencies that made this work possible: the Air Force Office of Scientific Research (YIP Grant No. FA9550-18-1-0061), and the Office of Naval Research (YIP Grant No. N00014-20-1-2681).

Finally, and most importantly, I would like to thank my parents for always loving, understanding, and encouraging me in pursuit of my dream and career aspiration.

# TABLE OF CONTENTS

LIST OF TABLES	viii
LIST OF FIGURES	ix
CHAPTER 1 INTRODUCTION	1
1.1 Background	1
1.2 Photoelectron Emission Mechanisms	2
1.2.1 Multiphoton Over-Barrier Emission	2
1.2.2 Tunneling Emission	
1.2.3 Keldysh Parameter	7
1.3 Theoretical Models for Photoemission from Metal Surfaces	8
1.3.1 Three-Step Model	8
1.3.2 Fowler-Nordheim Equation	10
1.3.3 Quantum Analytical Model	11
1.4 Organization of This Thesis	
CHAPTER 2 TWO-COLOR LASER INDUCED PHOTOEMISSION	16
2.1 Introduction	
2.2 Photoemission Without DC Bias	17
2.2.1 Analytical Model	17
2.2.2 Results and Discussion	
2.2.3 Summary on Photoemission without DC Bias	28
2.3 Photoemission with DC bias	29
2.3.1 Analytical model	29
2.3.2 Results and Discussion	
2.3.3 Application to Time-Resolved Photoelectron Spectroscopy	44
2.3.4 Summary on Photoemission with DC Bias	47
2.5 Conclusion	48
CHAPTER 3 PHOTEMISSION MODULATION BY TWO LASERS OF THE SAM	
FREQUENCY	
3.1 Introduction	
3.2 Analytical model	
3.3 Results and Discussion.	53
3.4 Conclusion	58
CHAPTER 4 FEW-CYCLE LASER PULSES INDUCED PHOTOEMISSION	59
4.1 Introduction	
4.2 Analytical Formulation	60
4.3 Results and Discussion.	65
4.4 Conclusion	72

CHAPTER 5 PHOTOELECTRON EMISSION IN A NANOSCALE GAP	74
5.1 Introduction	74
5.2 Photoelectron Transport without DC Bias	
5.2.1 Analytical Model	75
5.2.2 Results and Discussion	79
5.2.3 Summary on Photoelectron Transport without DC Bias	84
5.3 Photoelectron Transport with DC Bias	85
5.3.1 Analytical model	85
5.3.2 Results and Discussion	
5.3.3 Summary on Photoelectron Transport with DC Bias	98
CHAPTER 6 SUMMARY AND SUGGESTED FUTURE WORK	
6.1 Summary	99
6.2 Suggested future work	101
APPENDICES	102
APPENDIX A: Two-color laser induced photoemission without dc field	103
APPENDIX B: Two-color laser induced photoemission with dc field	103
APPENDIX C: Few-cycle laser pulses induced photoemission	
APPENDIX D: Photoelectron transport in a nanoscale gap without dc bias	104
APPENDIX E: Photoelectron transport in a nanoscale gap with dc bias	105
BIBLIOGRAPHY	107

# LIST OF TABLES

Table 1: List of achieved strong	local dc fields	(after field	enhancement)	of sharp	tips before
breakdown for eight materials	• • • • • • • • • • • • • • • • • • • •				47

# LIST OF FIGURES

Figure 1.1: Multiphoton over-barrier emission. Electron inside the metal is excited to a continuum state by absorbing enough photon energy and then escapes from the metal surface. $W$ and $E_F$ are the work function and Fermi energy of metal, respectively
Figure 1.2: Log-scale plot of photoelectron yield from a sharp gold tip as a function of laser power with 800 V dc bias (red curve) and without dc bias (blue curve) [9]
Figure 1.3: Optical field emission. The potential barrier near the metal surface greatly oscillates with time under the illumination of strong laser field, enabling the electron tunneling emission. $W$ and $E_F$ are the work function and Fermi energy of metal, respectively
Figure 1.4: Log-scale plot of photoelectron yield from sharp gold nanotip as a function of laser energy. The decreasing slope with the increasing incident energy indicates the transition of the dominant emission process from multiphoton over-barrier emission to optical field emission [11].
Figure 1.5: Photon-assisted tunneling emission. The tunneling potential barrier near the metal surface is formed under the strong dc field. Electron tunneling emission is possible even with a weak laser field. $W$ and $E_F$ are the work function and Fermi energy of metal, respectively 6
Figure 1.6: Experimentally measured photoelectron energy spectra from tungsten nanotip with strong dc field [46]
Figure 1.7: Comparison between the experimentally measured QE under low dc electric field (black points) and calculated QE under low (red solid line) and high (blue dashed line) dc electric field [72].
Figure 1.8: (a) Fowler-Nordheim plots of field emission (blue squares) and dc-assisted optical tunneling (red circles) [8]. (b) Fowler-Nordheim fit to the experimental measurements (bright orange dashed line) [19]
Figure 1.9: (a) Photoelectron energy spectra with increasing laser field. Left three plots show the experimental measurements [54]. Right three plots show the calculation from Zhang's quantum analytical model [6]. (b) Photoemission current as a function of applied dc field. Left plot is the experimental result [9]. Right plot is Zhang's quantum analytical results [6]
Figure 2.1: Energy diagram for electron emission through a wiggling potential barrier induced by two-color laser fields across the metal-vacuum interface at $x = 0$ . Electrons with initial energy of

$\varepsilon$ are excited to emit through <i>n</i> -photon absorption, with a transmitted energy of $\varepsilon + nh\omega$ , with <i>n</i> being an integer. The fundamental and the harmonic laser fields are $F_1\cos(\omega t)$ and $F_2\cos(\beta\omega t + \theta)$ , respectively. $E_F$ and $W$ are the Fermi energy and work function of the metal, respectively
Figure 2.2: Photoelectron energy spectra, calculated from Equation (19). (a)-(e) Energy spectra under different combinations of two-color laser fields $F_1$ (at frequency $\omega$ ) and $F_2$ (at frequency $2\omega$ ), for the special case of $\theta=0$ . (f)-(j) Energy spectra for various phase differences $\theta$ . The unit of laser fields $F_1$ and $F_2$ is V/nm in all figures
Figure 2.3: Normalized total time-averaged emission current density for the phase differences $\theta = 0$ and $\pi$ . (a)-(b) total time-averaged current density $\langle w \rangle$ as a function of the second-harmonic laser field $F_2$ , under various fundamental laser fields $F_1$ . (c)-(d) $\langle w \rangle$ as a function of $F_1$ , under various $F_2$ . The laser intensity is related to the laser electric field as $I[W/cm^2] = 1.33 \times 10^{11} \times (F_1[V/nm])^2$ . The dotted lines represent the scale $\langle w \rangle \propto F^{2n}$ .
Figure 2.4: Current modulation depth. (a) Normalized total time-averaged emission current density $\langle w \rangle$ as a function of the phase difference $\theta$ , under different $F_2/F_1$ . (b) Magnification of the bottom area of (a). (c) Semi-log plot of $\langle w \rangle$ in (a). $F_1$ is fixed at 1.6 V/nm in (a)-(c). (d) Electron energy spectra of $\langle w \rangle_{max}$ (point A) and $\langle w \rangle_{min}$ (point B) for $F_2/F_1=0.1375$ in (c). (e) Current modulation depth $\Gamma$ as a function of the field ratio $F_2/F_1$ for different $F_1=0.5$ , 1.6, and 10 V/nm
Figure 2.5: Total time-dependent emission current density for the phase differences $\theta=0$ and $\pi$ . (a)-(b) Total time-dependent emission current density $w(\bar{x},t)$ as a function of the space $\bar{x}$ and time $t$ . (c)-(d) Total emission current density $w(t)$ at $\bar{x}=100$ as a function of time $t$ . Dotted lines in (c) and (d) are for the total time-dependent laser field $F=F_1\cos(\omega t)+F_2\cos(\beta\omega t+\theta)$ . The fundamental laser field $F_1=1.6$ V/nm. The second harmonic ( $\beta=2$ ) laser field $F_2=0.22$ V/nm (experimental laser parameters in Reference [57]). When $\theta=0$ , the normalized time-averaged emission current density $\langle w \rangle = 5.23 \times 10^{-10}$ ; when $\theta=\pi$ , $\langle w \rangle = 7.31 \times 10^{-11}$
Figure 2.6: Effects of the harmonic order. The emission current modulation depth $\Gamma$ , the maximum and minimum time-averaged current density, $\langle w \rangle_{max}$ and $\langle w \rangle_{min}$ as a function of harmonic order $\beta$ . The fundamental laser field $F_1$ and the harmonic laser field $F_2$ are 1.6 V/nm and 0.22 V/nm, respectively (intensity ratio of 2%).
Figure 2.7: Energy diagram for photoemission under two-color laser fields and a dc bias. Electrons with initial energy $\varepsilon$ are emitted from the dc biased metal-vacuum interface at $x=0$ , with the transmitted energy of $\varepsilon + n\hbar\omega$ , due to the $n$ -photon contribution [multiphoton absorption $(n>0)$ , tunneling $(n=0)$ , and multiphoton emission $(n<0)$ ], where $n$ is an integer. The fundamental and harmonic laser fields are $F_1\cos(\omega t)$ and $F_2\cos(\beta\omega t + \theta)$ , respectively. The dc electric field is $F_0$ . The photon energy of the fundamental (harmonic) laser is $\hbar\omega$ $(\beta\hbar\omega)$ . $E_F$ and $W$ are the Fermi energy and work function of the metal, respectively

Figure 2.8: Photoelectron energy spectra under different in-phase (i.e., $\theta=0$ ) laser fields $F_1$ (at frequency $\omega$ ) and $F_2$ (at frequency $2\omega$ ) and dc fields $F_0$ . In (a)-(c) $F_2$ is fixed as 1 V/nm, and in (d)-(f) $F_1$ is fixed as 10 V/nm. The $n$ -photon process (that is the horizontal axis) is given with respect to the fundamental laser frequency, which measures the energy of the emitted electrons. The units of dc field $F_0$ and laser fields $F_1$ and $F_2$ are V/nm in all figures
Figure 2.9: Normalized total time-averaged emission current density $\langle w \rangle$ , for the phase difference between the two-color lasers (a)-(c) $\theta = 0$ , and (d)-(f) $\theta = \pi$ , as a function of the fundamental laser field $F_1$ , under various combinations of the second-harmonic laser field $F_2$ and dc electric field $F_0$ . The laser intensity is related to the laser electric field as $I_{1,2}$ (W/cm <sup>2</sup> ) = 1.33 × 10 <sup>11</sup> × ( $F_{1,2}$ (V/nm)) <sup>2</sup> .
Figure 2.10: Normalized time-averaged emission current density $\langle w_n \rangle$ through the <i>n</i> th channel, for the phase difference between the two-color lasers (a)-(c) $\theta=0$ , and (d)-(f) $\theta=\pi$ , as a function of the fundamental laser field $F_1$ , for various dc electric fields $F_0$ , when the second harmonic laser field $F_2=5$ V/nm. Dotted lines represent the normalized total emission current $\langle w \rangle = \sum_n \langle w_n \rangle$ .
Figure 2.11: Normalized total time-averaged emission current density $\langle w \rangle$ for the phase difference between the two-color lasers (a)-(c) $\theta=0$ , and (d)-(f) $\theta=\pi$ , as a function of the dc electric field $F_0$ , for different fundamental laser fields $F_1$ and second-harmonic laser fields $F_2$ . Intertwined curves in (d)-(f) indicate the strong interference effect of the two lasers
Figure 2.12: Normalized time-averaged emission current density $\langle w_n \rangle$ through the <i>n</i> th channel for the phase difference (a)-(c) $\theta=0$ , and (d)-(f) $\theta=\pi$ , as a function of the dc electric field $F_0$ , for various second-harmonic laser fields $F_2$ , when the fundamental laser field is $F_1=7$ V/nm. Dotted lines represent the normalized total emission current $\langle w \rangle = \sum_n \langle w_n \rangle$
Figure 2.13: Emission current modulation depth. (a) Normalized total time-averaged emission current density $\langle w \rangle$ as a function of the phase difference $\theta$ , for different dc electric fields $F_0$ , with $\omega$ -laser-field $F_1$ and $2\omega$ -laser-field $F_2$ fixed at 1.6 V/nm and 0.22 V/nm respectively (experimental laser parameters in Reference [57]). (b) Energy spectra of the emission current at different $\theta$ for the case of $F_0 = 1$ V/nm in (a). A, B, C, and D denote the cases of $\theta = 0$ , $\pi/2$ , $\pi$ , and $3\pi/2$ in (a), respectively. (c) Current modulation depth $\Gamma$ in (a) as a function of the dc field $F_0$ . The unit of dc field $F_0$ is V/nm in all figures.
Figure 2.14: Normalized total time-averaged emission current density $\langle w \rangle$ as a function of harmonic order $\beta$ , for the phase difference (a) $\theta = 0$ , and (b) $\theta = \pi$ . The fundamental $\omega$ -laser field $F_1 = 1.6$ V/nm, and the harmonic $\beta \omega$ -laser field $F_2 = 0.22$ V/nm
Figure 2.15: Effects of the image-charge-induced barrier lowering on the total emission current $\langle w \rangle$ for various $F_0$ , $F_1$ , $F_2$ , and $\theta$ . The solid (dotted) lines represent the cases with (without) the

image charge effect, calculated using effective work function $W_{eff}$ (work function $W$ ). The gray dashed lines show the scale $\langle w \rangle \propto F_1^{2n}$ .
Figure 2.16: Time-resolved photoelectron energy spectra for the tungsten nanotip. (a) Comparison between the experimentally measured electron counts from Figure 3 in Reference [57] (see solid lines) and fitting results $\langle w_n \rangle$ (see dotted lines). (b) Normalized total time-averaged emission current density $\langle w \rangle$ as a function of the phase difference between the two-color lasers $\theta$ , for different $F_2/F_1$ , with fixed $F_1=1.6$ V/nm. Blue and red lines denote the experimentally observed emission electron current and the sine fit from Figure 2(b) of Reference [57], respectively. (c), (d) Energy spectra for various dc fields $F_0$ when (c) $\theta=0$ , and (d) $\theta=\pi$ . (e), (f) Photoelectron spectra at different phase delays $\theta$ for the dc field (e) $F_0=0.01$ V/nm and (f) $F_0=0.09$ V/nm. (g), (h) Projection of the spectra in (e) and (f) on the $\theta$ plane, respectively. Except (b), the fundamental laser (1560 nm) field $F_1=1.8$ V/nm and the second-harmonic laser field $F_2=0.3$ V/nm for all other figures (experimental laser parameters in Reference [57])
Figure 3.1: Time-resolved photoelectron energy spectra. (a),(b) Energy spectra as a function of the phase difference between the two lasers $\theta$ , for dc field (a) $F_0 = 0$ and (b) $F_0 = 0.8$ V/nm. (c),(d) Projections of the spectra in (a),(b) on the $\theta$ - $\langle w_n \rangle$ plane respectively. (e),(f) Projections of the spectra in (a),(b) on the $n$ - $\langle w_n \rangle$ plane respectively. Here, the laser fields $F_1 = 1.8$ V/nm and $F_2 = 0.3$ V/nm (experimental parameters in Reference [57])
Figure 3.2: Photoemission current modulation. (a) Normalized total time-averaged emission current density $< w >$ as a function of phase difference $\theta$ for different $F_2/F_1$ , when the dc field $F_0 = 0$ . (b) Semilog plot of $< w >$ in (a). (c) Current modulation depth $\Gamma$ (solid lines) as a function of the laser field ratio $F_2/F_1$ for different dc fields $F_0$ . Dotted (dashed) lines in (c) are for the maximum (minimum) emission current density $< w >$ at $\theta = 0$ ( $\theta = \pi$ ). Here, the laser field $F_1$ is fixed as 1.8 V/nm.
Figure 3.3: (a) Emission current modulation depth $\Gamma$ (solid lines) as a function of the dc field $F_0$ with and without the image-charge-induced potential barrier lowering (or the Schottky effect), for laser fields $F_1 = 1.8$ V/nm and $F_2 = 0.3$ V/nm. The case without Schottky effect is calculated by replacing $W_{eff}$ with the nominal work function of metal $W$ in Equation (27). (b) Modulation depth $\Gamma$ (solid lines) as a function of $F_0$ for different laser field ratios $F_2/F_1$ , with the effective work function $W_{eff}$ . $F_1$ is fixed at 1.8 V/nm in (b). In (a),(b), the dotted (dashed) lines are for the maximum (minimum) emission current density $< w >$ at $\theta = 0$ ( $\theta = \pi$ )
Figure 3.4: Normalized total time-averaged emission current density $< w >$ as a function of the phase difference $\theta$ , for various (a) cathode materials and (b) incident wavelengths. In (a), the laser wavelength $\lambda = 800$ nm ( $\hbar \omega = 1.55$ eV). The nominal work function of different materials is $W_{\rm Ag} = 4.26$ eV [107], $W_{\rm w} = 4.31$ eV [57][60], $W_{\rm Mo} = 4.6$ eV [107], $W_{\rm Cu} = 4.65$ eV [107], and $W_{\rm Au} = 5.1$ eV [6][107]. In (b), the metal is tungsten. Here, the dc field $F_0$ is 0.8 V/nm and the laser fields $F_1$ and $F_2$ are fixed at 1.8 and 0.3 V/nm, respectively

Figure 4.1: (a) Sketch of photoelectron emission from a biased emitter under the illumination of a
laser pulse train with a time period $T$ . (b) A single laser pulse with carrier-envelope phase (CEP)
$\phi$ and full width at half maximum (FWHM) of the field envelope $\tau_p$ . The red curve and black
dotted lines denote the time evolution of laser electric field and laser pulse envelope, respectively.

Figure 4.3: CEP modulation in energy spectra with different pulse duration  $\tau_p$ . (a) Laser electric field for different  $\tau_p$  when CEP  $\phi=0$  and  $\pi$ . (b) Energy spectra as a function of  $\phi$  for different  $\tau_p$ . (c) Extracted energy spectra of  $\phi=0$  and  $\pi$  from (b). (d) Linear plot of energy spectrum for  $\tau_p=4.4$  fs in (c). (e) Normalized current modulation magnitude  $\Delta=(< w> - < w>_{ave})/< w>_{ave}$  as a function of  $\phi$  for different  $\tau_p$ . Here,  $< w>_{ave}=(< w>_{max}+< w>_{min})/2$  denotes the averaged value of < w> with respect to  $\phi$ . (f) Current modulation depth  $\Gamma=(< w>_{max}-< w>_{min})/(< w>_{max}+< w>_{min})$  as a function of  $\tau_p$ .

Figure 4.6: Total time-dependent emission current density  $w(\bar{x}, t)$  under the dc field  $F_0 = 1 \times 10^4$  V/m and  $1 \times 10^9$  V/m. (a),(b)  $w(\bar{x}, t)$  including surface oscillation currents as a function of the

Figure 5.2: Normalized time-averaged photoemission current density under various gap sizes and laser fields. (a) Total emission current density  $\langle w \rangle$  as a function of gap distance d for different laser fields  $F_1$ . Dashed lines denote the emission current density from a single surface when the metal on the right-hand side in Figure 5.1 is removed, which is obtained from Reference [6]. (b) Energy spectra for photoelectrons transmitted into the metal on the right-hand side for different d and  $F_1$ . (c) Photoelectron energy spectra for electrons inside the vacuum gap and in the metal on the right-hand side under different  $F_1$  for d=2 nm. For the curves for photoelectrons inside the gap, white-filled diamond markers denote the absolute value of negative emission current density  $\langle w_n \rangle$  through the nth channel.

Figure 5.3: (a) Normalized total time-averaged emission current density  $\langle w \rangle$  and (b) difference between total emission current  $\langle w \rangle$  and emission current from a single surface  $\langle w \rangle_{SS}$  as a function of laser field  $F_1$  for different gap distances d. The single surface case  $\langle w \rangle_{SS}$  is obtained from Reference [6]. The dashed line in (a) denotes the scale of  $\langle w \rangle \propto F_1^{2n}$  with n=4. (c) Emission current density  $\langle w \rangle$  as a function of laser field  $F_1$  for gap spacing d=3, 5, and 11 nm. Here, laser field regimes are labeled with n=4 and n=5 (cf. the areas filled with different colors), which means the dominant emission process in this field regime is four- or five- photon absorption. ...82

Figure 5.6: (a) Schematic of metal-vacuum-metal nanogap with a dc bias $V$ under the illumination of laser field. $d$ is the gap distance. (b) Energy diagram for photoelectron emission from left metal-vacuum interface of the gap in (a). Electrons with the initial energy $\varepsilon$ would see a potential barrier subjected to a positive dc electric field $F_0 = V/d$ (> 0) and laser field $F_1\cos(\omega t)$ . (c) Energy diagram for photoelectron emission from right metal-vacuum interface of the gap in (a). Electrons would see a potential barrier with a negative dc electric field $F_0 = -V/d$ (< 0) and laser field $F_1\cos(\omega t)$ with $F_1$ of opposite sign of that in (b) at any time instant for a given laser field85
Figure 5.7: Photoelectron energy spectra for dc field (a) $F_0 = 1$ and 3 V/nm and (c) $F_0 = -1$ and -3 V/nm. Emission mechanisms when (b) $F_0 = 1$ and 3 V/nm and (d) $F_0 = -1$ and -3 V/nm. Here, laser field $F_1 = 1$ V/nm and gap distance $d = 5$ nm.
Figure 5.8: Normalized total time-averaged emission current density $\langle w \rangle$ as a function of laser field $F_1$ for various dc fields $F_0$ . The gap distance $d$ is fixed at 5 nm. The black dashed lines display the scale $\langle w \rangle \propto F_1^{2n}$ . Here, $n=2.8, 1.9, 6.5$ and 12.4 when $F_0=1, 3, -1$ , and -3 V/nm is consistent with the observed orders of domination multiphoton emission channel in Figures 5.7(a) and 5.7(c).
Figure 5.9: Normalized total time-averaged emission current density $\langle w \rangle$ as a function of gap distance $d$ for different dc fields $F_0$ and laser fields $F_1$ . Dashed lines denote the emission current density from single surface, which is obtained from Reference [6]
Figure 5.10: (a),(b) Normalized total time-averaged emission current density $\langle w \rangle$ as a function of dc field $F_0$ for different laser fields $F_1$ . (c) The dependence of net emission current density $\langle w \rangle$ on the applied dc bias for different laser fields $F_1$ . Here, gap distance $d$ is fixed at 5 nm
Figure 5.11: Time-dependent emission electron density from left metal surface of the nanogap in Figure 5.6(a) as a function of time $t$ and space $x$ under various combinations of dc and laser fields. Solid white lines show the corresponding classical trajectories [76]. Dotted white lines show the laser electric field. Here, gap distance $d$ is fixed at 5 nm. The units of dc field $F_0$ and laser field $F_1$ are V/nm in all figures
Figure 5.12: Time-dependent emission electron density from right metal surface of the nanogap in Figure 5.6(a) as a function of time $t$ and space $x$ under various combinations of dc and laser fields. Here, gap distance $d$ is fixed at 5 nm. The units of dc field $F_0$ and laser field $F_1$ are V/nm in all figures.

#### **CHAPTER 1**

#### INTRODUCTION

# 1.1 Background

Ultrafast science concerns the study of electronic dynamics and motion in ultrashort timescale with the aid of ultrafast lasers. This field has been widely explored in atomic and molecular systems. The main observation includes above-threshold ionization [1][2] and high-order harmonic generation [3]. In recent decade, a new research direction has emerged in the ultrafast science field, which is the study of laser-induced electron emission from solid nanostructures [4]–[6]. Utilizing the solid-state nanostructures [7]–[23], especially those made of metals, enables the nanoscopic confinement of optical fields and the resulting large field enhancement factor on the nanosurface. The former provides the possibility for the control of ultrafast electron emission on the nanometer scale, which is fundamentally important to the development of high-resolution electron microscopy [24]–[27], highly coherent electron sources [28]–[30] and novel nano-vacuum electronic devices [31]–[36]; the latter enables the access to strong-field optics with low laser intensity, which can reduce the requirement for the laser experimental system and avoid thermal damage on the structure when illuminated by strong laser fields [4][37]. Photoemission is also important to the development of vacuum electronics, high power electromagnetic sources and amplifiers, and high current cathodes [38]–[45].

The initial work on ultrafast laser-induced electron emission from nanostructure is reported by Hommelhoff and his colleagues [7]. They demonstrated the nonlinearity of ultrafast photoelectron emission from a tungsten nanotip driven by low-power femtosecond laser. A variety of photoemission properties from metallic nanostructures were subsequently revealed, including the transition from multiphoton emission to strong optical-field emission [11], dc-assisted tunneling

emission [6][8][46], surface-plasmon boosted emission [20][37][47]–[49], dense-arrays enhancement effect [50][51], dependence of emission distribution on optical orientation [52][53], carrier-envelope-phase (CEP) sensitivity [13][54]–[56], modulation effect of two-color lasers [57]–[62], and rectification effect of metal-vacuum-metal nanogap [63]–[66].

#### 1.2 Photoelectron Emission Mechanisms

Photoemission mechanisms in general depend on the local optical field intensity. This section summarizes the photoemission processes from metal surface in different field intensity regimes.

# 1.2.1 Multiphoton Over-Barrier Emission

Under the illumination of a weak laser field, the main photoemission process is multiphoton overbarrier emission, where the electron inside the metal is excited to a continuum state by absorbing a threshold number of photons or more photons and then escapes from the metal surface (see Figure 1.1). The photoemission yield follows a power law in the incident laser intensity, and the exponent denotes the threshold number of photons needed to overcome the potential barrier. Figure 1.2 displays the experimentally measured multiphoton emission current from a sharp gold tip as a function of the incident laser power [9]. For zero dc bias (see the blue line in Figure 1.2), the fourth-order power dependence indicates the electron inside the tip needs to absorb at least four photons for the emission, which is consistent with the ratio of the work function of gold ( $\approx 5 \text{ eV}$ ) over incident single photon energy of 1.5 eV (for 828 nm laser),  $W/\hbar\omega \approx 3.3$ .

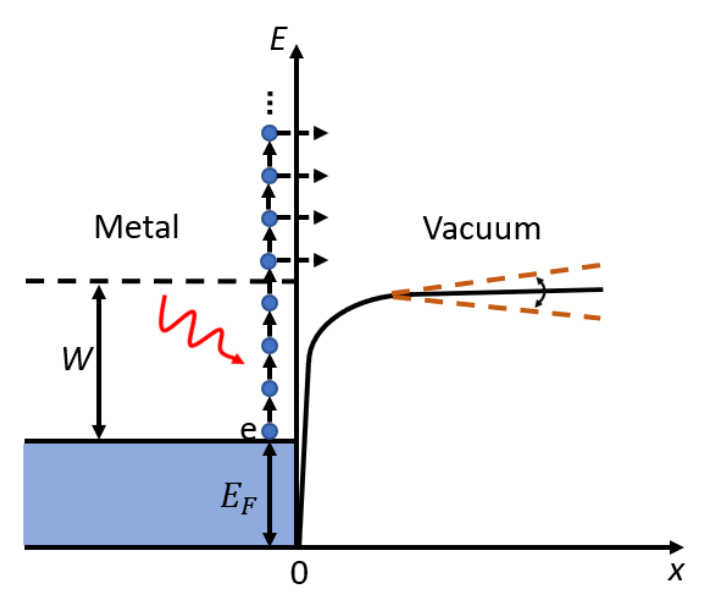


Figure 1.1: Multiphoton over-barrier emission. Electron inside the metal is excited to a continuum state by absorbing enough photon energy and then escapes from the metal surface. W and  $E_F$  are the work function and Fermi energy of metal, respectively.

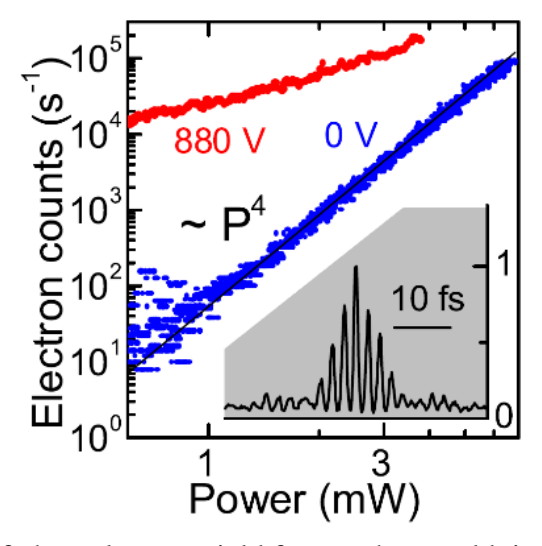


Figure 1.2: Log-scale plot of photoelectron yield from a sharp gold tip as a function of laser power with 800 V dc bias (red curve) and without dc bias (blue curve) [9].

# 1.2.2 Tunneling Emission

## **Optical field emission**

Optical field emission occurs in the strong laser field regime, where the potential barrier near the metal surface greatly oscillates with time, enabling the electron tunneling into the vacuum with less photon absorption than multiphoton over-barrier emission (see Figure 1.3). Optical field

emission only occurs during the positive half laser cycles, as shown in Figure 1.3. Bormann *et al*, [11] firstly reported the optical field emission from nanostructure, and their main experimental observation is displayed in Figure 1.4. With increasing laser energy, the slope of photoemission current decreases, indicating the transition of dominant emission from multiphoton over-barrier emission to optical field emission.

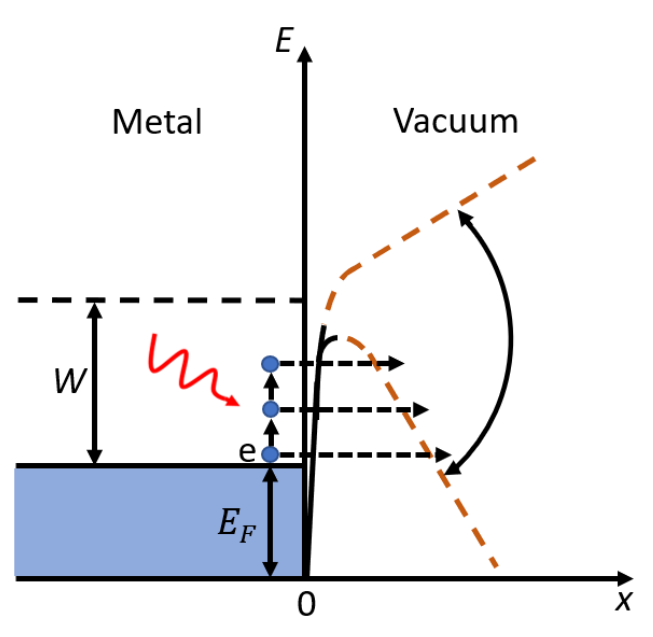


Figure 1.3: Optical field emission. The potential barrier near the metal surface greatly oscillates with time under the illumination of strong laser field, enabling the electron tunneling emission. W and  $E_F$  are the work function and Fermi energy of metal, respectively.

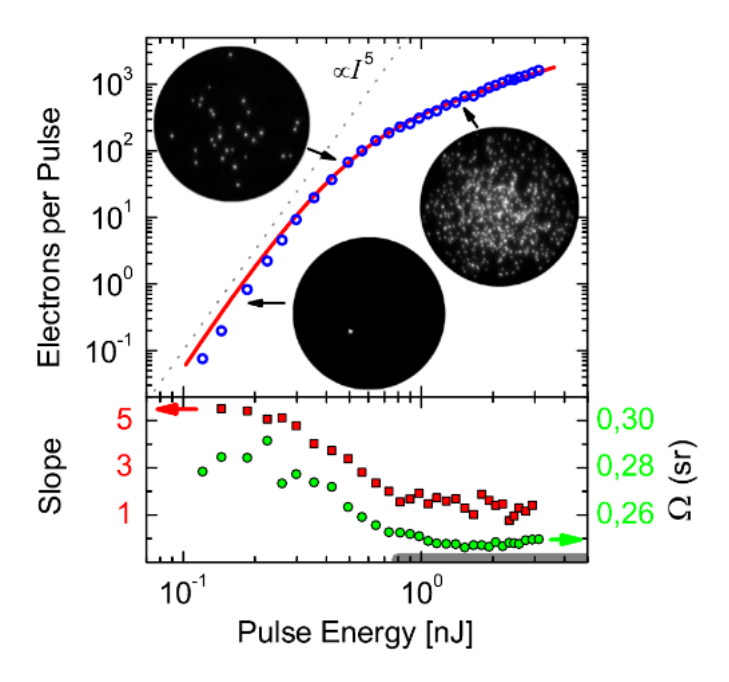


Figure 1.4: Log-scale plot of photoelectron yield from sharp gold nanotip as a function of laser energy. The decreasing slope with the increasing incident energy indicates the transition of the dominant emission process from multiphoton over-barrier emission to optical field emission [11].

# Photon-assisted tunneling emission

For the sharp metallic tip, a strong dc field can be easily obtained at the apex due to strong field enhancement near the tip, inducing a narrow barrier near the metal surface. This makes the electron tunneling emission possible, even in the weak laser field regime (see Figure 1.5), which is referred as photon-assisted tunneling emission (or dc-assisted optical tunneling). Figure 1.6 displays the experimentally measured photoelectron energy spectra from a tungsten nanotip with strong dc field, where the photon-assisted tunneling emission is the main emission process [46].

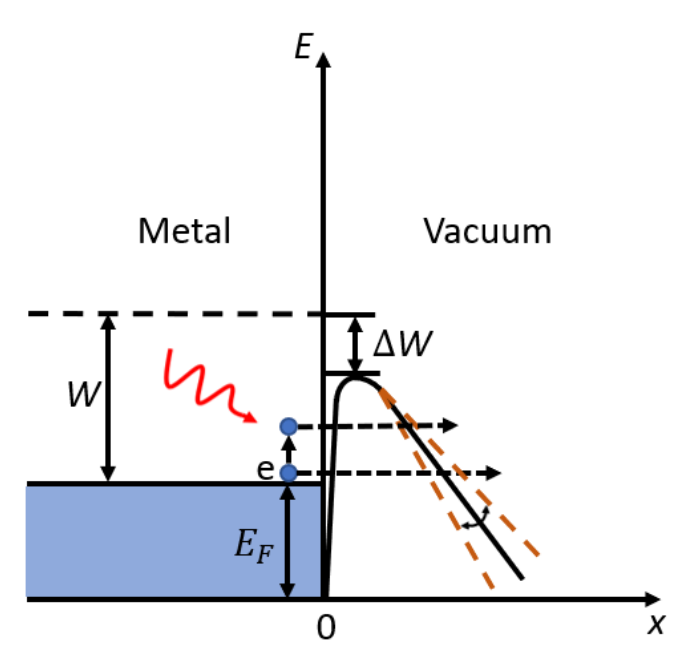


Figure 1.5: Photon-assisted tunneling emission. The tunneling potential barrier near the metal surface is formed under the strong dc field. Electron tunneling emission is possible even with a weak laser field. W and  $E_F$  are the work function and Fermi energy of metal, respectively.

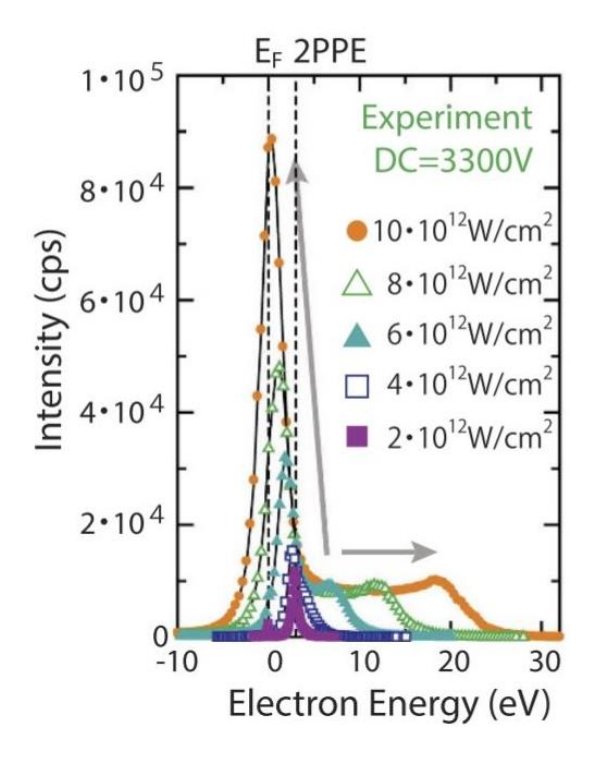


Figure 1.6: Experimentally measured photoelectron energy spectra from tungsten nanotip with strong dc field [46].

In addition, due to the image charge effect (or Schottky effect) induced by the strong dc field, a significant reduction of potential barrier  $\Delta W$  appears at the surface (see Figure 1.5), which is given by,

$$\Delta W = \sqrt{e^3 F_{DC} / 4\pi \varepsilon_0} \tag{1}$$

where e is the elementary charge,  $F_{DC}$  is the local dc field, and  $\varepsilon_0$  is the free space permittivity. The decreased barrier height can greatly increase the photoelectron emission yield.

## 1.2.3 Keldysh Parameter

Keldysh parameter  $\gamma$  is used to define the limit between multiphoton over-barrier emission and optical field emission [67]. It is given by,

$$\gamma = \sqrt{\frac{W}{2U_p}} \tag{2}$$

where W is the work function of metal and  $U_p$  is the ponderomotive energy which describes the time-averaged kinetic energy of an electron with charge -e and mass  $m_e$  in an oscillating electric field with the angular frequency  $\omega$  and field amplitude F,

$$U_P = \frac{e^2 F^2}{4m_e \omega^2} \tag{3}$$

For  $\gamma > 1$  (weak optical field), the dominant emission mechanism is multiphoton over-barrier emission. For  $\gamma < 1$  (strong optical field), the optical field emission dominates. When the Keldysh parameter  $\gamma$  is close to 1, the contribution from multiphoton over-barrier and optical field emission coexists.

#### 1.3 Theoretical Models for Photoemission from Metal Surfaces

A variety of theoretical approaches have been developed to describe and understand the underlying photoelectron emission mechanisms, such as Fowler-Dubridge model [68]–[71], three-step model [72]–[74], perturbative theory [11][75][76], Floquet method [76][77], Fowler-Nordheim tunneling approximation [8][19][55], and directly solving the time-dependent Schrödinger equation (TDSE) [6][7][13][76][78]–[80]. In this section, we introduce the commonly used three-step model, Fowler-Nordheim equation, and quantum analytical model based on the TDSE.

## 1.3.1 Three-Step Model

Three-step model considers photoelectron emission as three sequentially independent processes: (1) Electrons inside the metal are excited to higher energy states by absorbing the incident photon; (2) Excited electrons migrate to the metal surface, where electron-electron scattering effect is included; (3) Electrons with the energy larger than the potential barrier energy escape from the metal surface. The photoemission quantum efficiency (QE), defined as the ratio of the number of emission electrons over that of incident photons, is expressed in terms of the probabilities of these three steps [72][73],

 $QE(\omega)$ 

$$= [1 - R(\omega)] \frac{\int_{E_F + W_{eff} - \hbar\omega}^{\infty} dE[1 - f_{FD}(E + \hbar\omega)] f_{FD}(E) \int_{cos\theta_{max}}^{1} d(cos\theta) F_{e-e}(E, \omega, \theta) \int_{0}^{2\pi} d\Phi}{\int_{E_F - \hbar\omega}^{\infty} dE[1 - f_{FD}(E + \hbar\omega)] f_{FD}(E) \int_{-1}^{1} d(cos\theta) \int_{0}^{2\pi} d\Phi}$$

(4)

where  $R(\omega)$  is the metal surface reflectivity as a function of optical frequency  $\omega$ ,  $f_{FD}(E) = 1/\{1 + \exp[(E - E_F)/k_BT]\}$  is the Fermi-Dirac function, describing the distribution of electron energy states inside the metal,  $E_F$  is the Fermi energy of metal,  $W_{eff}$  is the effective work function

including the Schottky effect,  $F_{e-e}(E,\omega,\theta)$  is the probability an electron reaches the metal surface without electron-electron scattering,  $\theta$  is the angle between the electron velocity and the surface normal,  $\Phi$  is the azimuthal angle,  $\cos\theta_{max} = \sqrt{(E_F + W_{eff})/(E + \hbar\omega)}$ , where  $\theta_{max}$  is the maximum escape angle for electrons with the total energy  $E + \hbar\omega$ .

At low temperature  $(k_BT \ll E_F)$ , the Fermi-Dirac function  $f_{FD}(E)$  can be approximated by Heaviside step function  $H(E_F - E)$ . When the photon energy  $\hbar \omega$  is close to the effective work function of the metal,  $\theta_{max}$  will be nearly normal to the metal surface. Thus, the angle  $\theta$  dependence of  $F_{e-e}(E, \omega, \theta)$  can be ignored. With these assumptions, Equation (4) can be simplified to [72][73],

$$QE(\omega) = [1 - R(\omega)]F_{e-e}(\omega)\frac{E_F + \hbar\omega}{2\hbar\omega} \times \left[1 + \frac{E_F + W_{eff}}{E_F + \hbar\omega} - 2\sqrt{\frac{E_F + W_{eff}}{E_F + \hbar\omega}}\right]. \tag{5}$$

As shown in Figure 1.7, the QE calculated from Equation (5) exhibits good agreement with the experimental measurements for copper surfaces. However, this model is constructed by the classical treatment, thus it only works in the multiphoton over-barrier emission regime instead of the strong optical field regime with quantum mechanical tunneling [74].

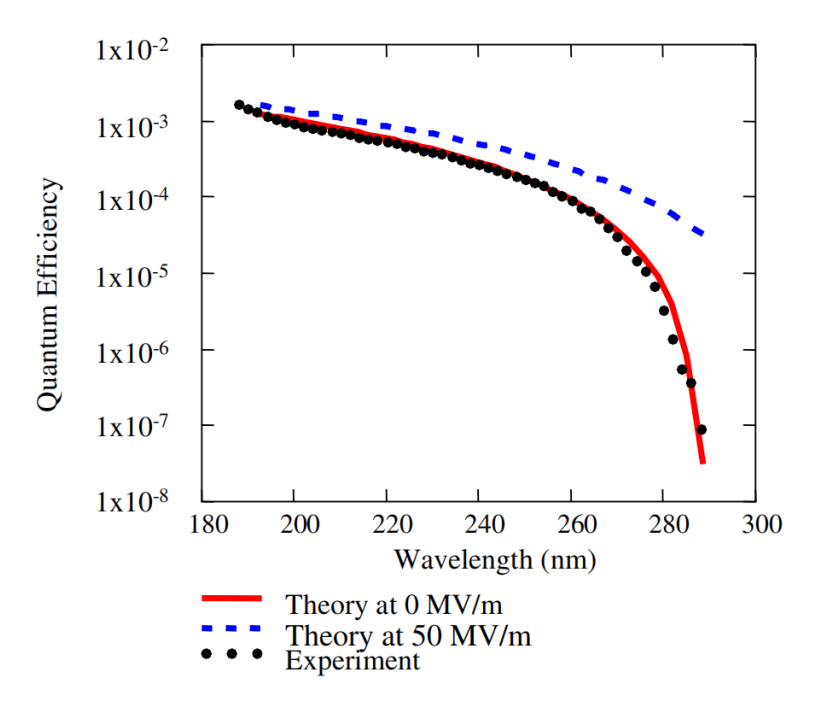


Figure 1.7: Comparison between the experimentally measured QE under low dc electric field (black points) and calculated QE under low (red solid line) and high (blue dashed line) dc electric field [72].

# 1.3.2 Fowler-Nordheim Equation

Fowler-Nordheim equation describes the field emission where electrons tunnel through a narrow potential barrier due to a strong static electric field. The formula is given by [8][81][82],

$$j_{FN} = \frac{e^3 F^2}{8\pi h \Phi t^2(\omega)} \exp\left[-\frac{8\pi \sqrt{2m_e} \Phi^{\frac{3}{2}}}{3heF} v(\omega)\right]$$
 (6)

where  $j_{FN}$  is the field emission current density, e is the elementary charge, F is the local dc electric field, h is the Planck constant,  $\Phi$  is the effective work function,  $t^2(\omega) \approx 1$  for field emission,  $m_e$  is the electron mass, and  $v(\omega) \approx 1 - \omega + \omega \ln \omega / 6$  with  $\omega = e^3 F / 4\pi \varepsilon_0 \Phi$ .

Fowler-Nordheim equation is also frequently used to calculate the photoemission rate *j* for the dc-assisted optical tunneling or strong optical field emission by directly replacing the electric field

F in Equation (6) with the sum of applied dc field  $F_0$  and time-dependent laser electric field  $F_1(t)$  [8][83]

$$j = j_{FN} (F_0 + F_1(t)) \tag{7}$$

Figure 1.8 shows that the experimentally measured field emission, dc-assisted optical tunneling emission and optical field emission can be well described by the Fowler-Nordheim scaling. Nevertheless, Fowler-Nordheim equation is only valid in the strong optical field regime instead of the multiphoton over-barrier emission regime.

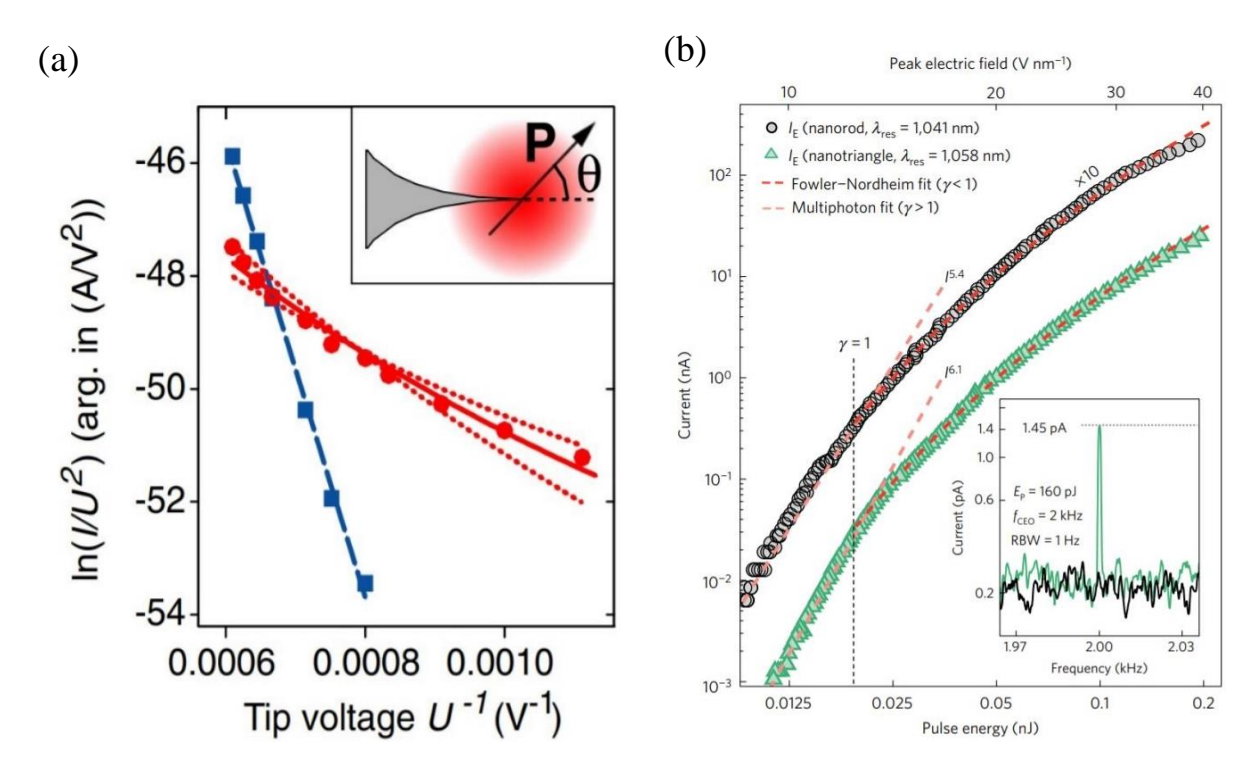


Figure 1.8: (a) Fowler-Nordheim plots of field emission (blue squares) and dc-assisted optical tunneling (red circles) [8]. (b) Fowler-Nordheim fit to the experimental measurements (bright orange dashed line) [19].

## 1.3.3 Quantum Analytical Model

Solving the TSDE is a quantum approach to describe the photoelectron emission, where the interaction between the electrons inside the metal is ignored. In 2016, Zhang and Lau [6] developed

an quantum analytical model for the photoemission due to a combination of a dc field  $F_0$  and a laser field  $F_1 \cos(\omega t)$ , by exactly solving the TDSE,

$$i\hbar \frac{\partial \psi(x,t)}{\partial t} = -\frac{\hbar^2}{2m_e} \frac{\partial^2 \psi(x,t)}{\partial x^2} + \Phi(x,t)\psi(x,t)$$
 (8)

where  $\hbar$  is the reduced Plank constant,  $m_e$  is the electron mass, and  $\Phi(x,t)$  is the time-dependent potential energy being 0 inside the metal (x < 0) and  $E_F + W_{eff} - eF_0x - eF_1x\cos(\omega t)$  in the vacuum  $(x \ge 0)$  respectively, with  $E_F$  being the Fermi energy of the metal,  $W_{eff}$  the effective work function including the Schottky effect and e the elementary charge. Here, both external electric fields are assumed to be perpendicular to the flat metal surface. Based on the triangular potential barrier, the exact solution of electron wavefunction  $\psi_i(x,t)$  inside the metal and  $\psi_t(x,t)$  in the vacuum are obtained [6],

$$\psi_i(x,t) = \exp\left(-\frac{i\varepsilon t}{\hbar} + ik_0 x\right) + \sum_{n=-\infty}^{\infty} R_n \exp\left(-i\frac{\varepsilon + n\hbar\omega}{\hbar}t - ik_n x\right), \quad x < 0$$
 (9)

$$\psi_t(x,t) = \sum_{n=-\infty}^{\infty} T_n[Ai(-\eta_n) - iBi(-\eta_n)] \times \exp\left(-i\frac{\varepsilon}{\hbar}t - in\omega t\right)$$

$$\times \exp\left(\frac{ieF_1\sin(\omega t)}{\hbar\omega}x + \frac{ie^2F_1^2\sin(2\omega t)}{8\hbar m_e\omega^3} - \frac{ie^2F_0F_1\sin(\omega t)}{\hbar m_e\omega^3}\right), \quad x \ge 0 \quad (10)$$

where  $k_0=\sqrt{2m_e\varepsilon/\hbar^2}$  and  $k_n=\sqrt{2m_e(\varepsilon+n\hbar\omega)/\hbar^2}$  are the electron wave number, Ai and Bi are the Airy functions of the first kind and second kind respectively,  $\eta_n=[\frac{E_n}{eF_0}+x+\frac{eF_1\cos(\omega t)}{m_e\omega^2}](\frac{2em_eF_0}{\hbar^2})^{\frac{1}{3}}$ , the drift kinetic energy  $E_n=\varepsilon+n\hbar\omega-E_F-W_{eff}-U_p$ , and the ponderomotive energies  $U_p=e^2F_1^2/4m_e\omega^2$ . The transmission coefficient  $T_n$  can be obtained

from the boundary conditions that both the electron wave function  $\psi(x,t)$  and its derivative  $\partial \psi(x,t)/\partial x$  are continuous at x=0 (see Reference [6]).

Using the probability current density, the time-averaged normalized emission current density, defined as the time-averaged ratio of the transmitted probability current density over the incident probability current density,  $\langle w(\varepsilon, x, t) \rangle = \langle J_t/J_i \rangle$ , can be obtained as,

$$\langle w(\varepsilon) \rangle = \sum_{n=-\infty}^{\infty} \langle w_n(\varepsilon) \rangle, \quad \langle w_n(\varepsilon) \rangle = \frac{(eF_0\hbar/\sqrt{2m_e})^{1/3}}{\pi\sqrt{\varepsilon}} |T_n|^2, \tag{11}$$

where  $\langle w_n \rangle$  denotes the normalized emission current density through the *n*th channel with emitted electron energy  $\varepsilon + n\hbar\omega$  due to the *n*-photon contribution.

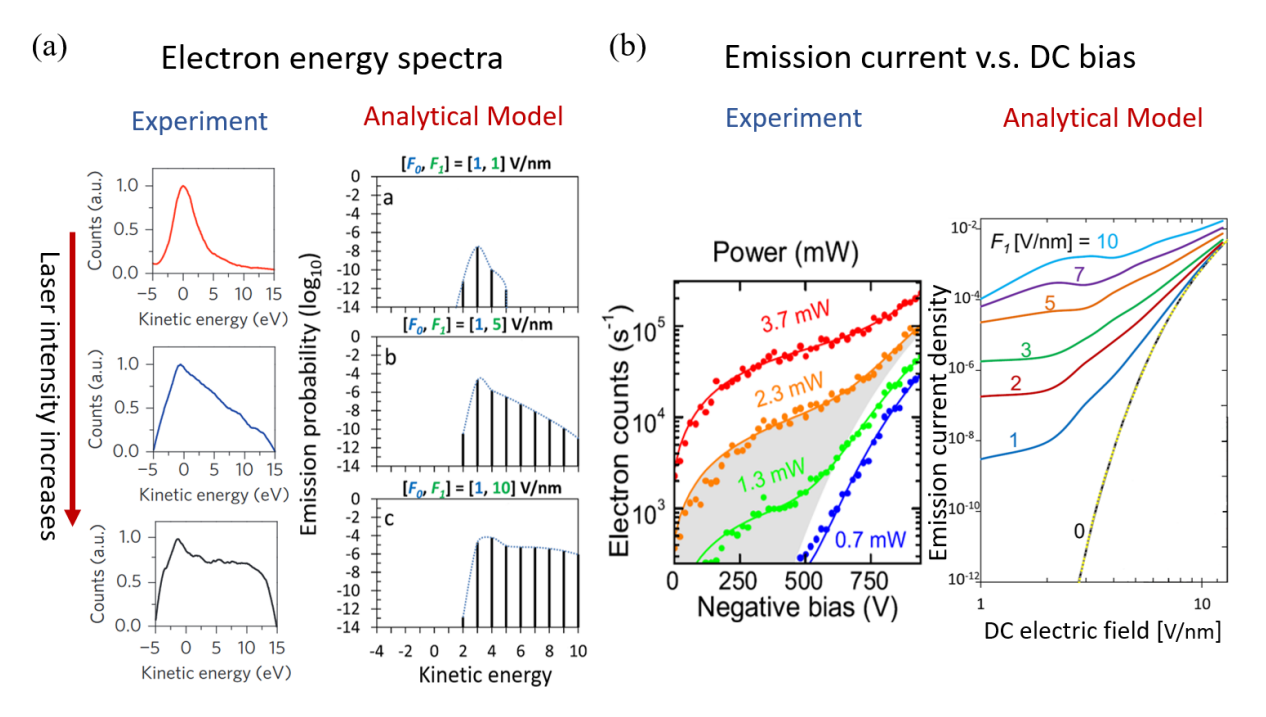


Figure 1.9: (a) Photoelectron energy spectra with increasing laser field. Left three plots show the experimental measurements [54]. Right three plots show the calculation from Zhang's quantum analytical model [6]. (b) Photoemission current as a function of applied dc field. Left plot is the experimental result [9]. Right plot is Zhang's quantum analytical results [6].

As shown in Figure 1.9, the calculation from the quantum model recovers the experimentally measured trends on the energy spectra for the transition from multiphoton to optical field emission

and the voltage and laser power dependence of photoelectron yield. These good agreement with the experimental results display the validity of Schrödinger-based analytical model in both multiphoton over-barrier regime and optical field regime. Our theoretical model in this thesis is also derived from the TDSE.

# **1.4 Organization of This Thesis**

In this thesis, we develop analytical quantum models to study ultrafast optical-field induced photoelectron emission from biased metal surfaces, by solving TDSE *exactly*. We consider two-color laser induced photoelectron emission with and without dc bias, interference modulation of photoemission using two lasers of the same frequency, nonlinear ultrafast photoemission from a dc-biased surface triggered by few-cycle laser pulses, and laser induced photoelectron transport in nanogaps.

Chapter 2 presents analytical models for nonlinear ultrafast photoelectron emission from metal surface induced by two-color laser fields without and with dc bias, by exactly solving the TDSE. The photoelectron energy spectra, emission current density and current modulation under various combinations of laser intensities, frequencies, dc fields, and phase differences of the two-color lasers are analyzed. The application of our model to the time-resolved photoelectron spectroscopy of one dimensional (1D) system is exemplified.

Chapter 3 explores the modulation to photoemission current and dynamics of multiphoton excited states using two lasers of the same frequency. The effects of different laser fields, wavelengths, cathode materials, and dc bias are analyzed in detail. The capability of measuring the time-resolved photoelectron energy spectra using single-frequency laser pairs is demonstrated.

Chapter 4 presents an analytical model for nonlinear ultrafast photoemission from a dc-biased surface triggered by few-cycle laser pulses, by exactly solving the TDSE. Our exact model is valid

for arbitrary pulse length from sub-cycle to CW excitation, and for arbitrary pulse repetition rate. The photoelectron energy spectra, emission current and emission charge density with different combinations of laser pulse repetitions, durations, laser intensities, CEP and dc fields are explored, showing good agreement with the experimental observations. This work offers clear insights to the photoelectron energy distribution and spatiotemporal dynamics of electron emission with different ultrashort pulses and dc fields.

Chapter 5 presents analytical models for ultrafast photoelectron emission in a nanoscale metal-vacuum-metal gap driven by a single-frequency laser field. We study the dependence of photoelectron spectra and emission current on gap distance, laser intensity, wavelength, and metal materials. This work may provide useful guidance for the future design of ultrafast optoelectronic devices, such as photodetectors.

Chapter 6 gives a summary and an outlook to future works.

#### **CHAPTER 2**

## TWO-COLOR LASER INDUCED PHOTOEMISSION

#### 2.1 Introduction

Two-color laser induced photoelectron emission from nanostructure is reported by Förster and his colleagues [57] in 2016. They found a substantial emission current modulation of 94% for tungsten nanotips via the control of the relative phase between a strong fundamental laser and a weak second-harmonic laser, due to the interference effect between quantum emission pathways. This provides a new platform for coherently controlling electron dynamics in ultrashort spatiotemporal scales by the phase difference between the two-color lasers. By optimizing the employed laser and dc electric fields, Paschen *et al* [59] reported a nearly perfect two-color emission current modulation of up to 97.5% for tungsten nanotip in 2017. Other aspects of two-color photoemission from metallic nanostructures are also studied, including laser polarization dependence [58], interaction of two-color lasers with free electron beams [84] and plasmon-assisted emission [85]. Despite these recent studies on two-color photoemission from metallic nanostructure, the correlation between laser fields, applied dc bias and various underlying emission processes is still not well understood. The parametric dependence of the photoelectron emission needs substantial further study.

In this chapter, we present quantum analytical models for nonlinear ultrafast photoelectron emission from metal surface induced by two-color laser fields without and with dc bias, by exactly solving the TDSE [61][62]. Our models are valid for arbitrary laser intensities, harmonic orders, phase differences between the two lasers, dc bias and metal work function and Fermi level. Various emission processes, including multiphoton over-barrier emission, dc-assisted tunneling emission and optical field emission, are all included in the single formulation. We comprehensively analyze

the photoelectron emission properties, including energy spectra, emission current density, and current modulation, under various combinations of laser intensities and frequencies, dc fields, and relative phase of the two-color lasers. We study the effects of image charge induced by the dc field on the emission current, which gives an examination on the sensitivity of photoemission to the shape of potential barrier. The application of our analytical model to the time-resolved photoelectron spectroscopy of one dimensional (1D) system is also demonstrated. The material of this chapter is based on our published papers References [61] and [62], and is presented with permission from the copyright holders.

#### 2.2 Photoemission Without DC Bias

### 2.2.1 Analytical Model

Our one-dimensional (1D) model (see Figure 2.1) considers electrons with initial energy  $\varepsilon$  are excited to the higher energy state by absorbing photon energy and then get emitted from the metal-vacuum interface at x=0, under the illumination of two-color laser fields,  $F_1\cos(\omega t)$  and  $F_2\cos(\beta\omega t+\theta)$ , where  $F_1$  and  $F_2$  are the magnitudes of the laser fields,  $\omega$  is the fundamental laser frequency,  $\beta$  is a positive integer, and  $\theta$  is the relative phase. We assume both laser fields are perpendicular to the metal surface, and cut off abruptly at the surface. The sudden screening of external fields is justified [6], because the laser penetration depth (i.e., skin depth) is typically much smaller than the laser wavelength (e.g., for the gold, the skin depth of 800 nm laser wavelength is around 4 nm).

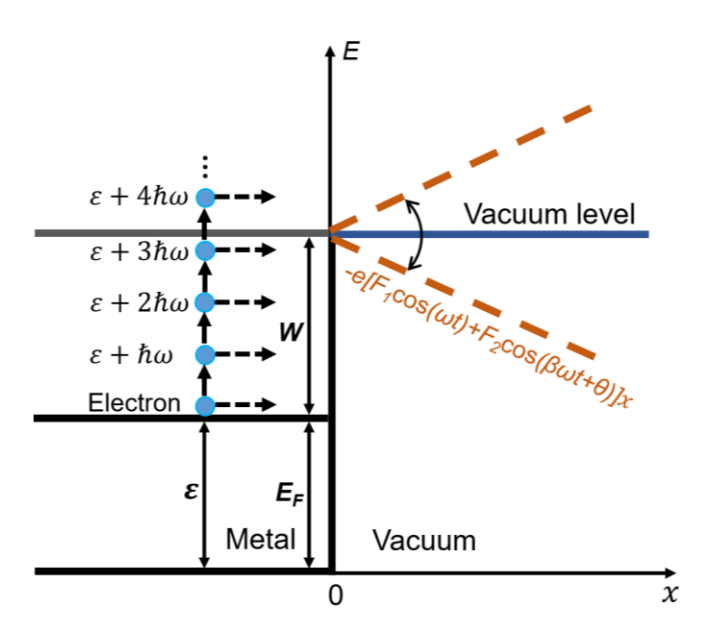


Figure 2.1: Energy diagram for electron emission through a wiggling potential barrier induced by two-color laser fields across the metal-vacuum interface at x = 0. Electrons with initial energy of  $\varepsilon$  are excited to emit through n-photon absorption, with a transmitted energy of  $\varepsilon + n\hbar\omega$ , with n being an integer. The fundamental and the harmonic laser fields are  $F_1\cos(\omega t)$  and  $F_2\cos(\beta\omega t + \theta)$ , respectively.  $E_F$  and W are the Fermi energy and work function of the metal, respectively.

A time-varying potential barrier would be created at the metal-vacuum interface x = 0,

$$\Phi(x,t) = \begin{cases} 0, & x < 0 \\ V_0 - eF_1 x \cos(\omega t) - eF_2 x \cos(\beta \omega t + \theta), & x \ge 0, \end{cases}$$
 (12)

where  $V_0 = E_F + W$ ,  $E_F$  and W are the Fermi energy and work function of the metal respectively, and e is the elementary charge. To make the analytical treatment possible, image charge effects are not included in Equation (12). However, our previous work [6] demonstrated a very good approximation to include the image charge potential in our model, by simply replacing the work function W with the effective work function due to Schottky barrier lowering.

The electron wave function  $\psi(x,t)$  is solved from the TDSE,

$$i\hbar \frac{\partial \psi(x,t)}{\partial t} = -\frac{\hbar^2}{2m_e} \frac{\partial^2 \psi(x,t)}{\partial x^2} + \Phi(x,t)\psi(x,t), \tag{13}$$

where  $\hbar$  is the reduced Plank constant,  $m_e$  is the electron mass, and  $\Phi(x, t)$  is the potential energy given in Equation (12).

An exact solution to Equation (13) for  $x \ge 0$  is obtained [61] (see Appendix A for the method),

$$\psi(x,t) = \sum_{n=-\infty}^{\infty} T_n \exp(-i\varepsilon t/\hbar - in\omega t) \times \exp\left(i\xi\sqrt{2m_e E_n/\hbar^2}\right)$$

$$\times \exp\left(\frac{ie}{\hbar}Lx + \frac{ie^2}{8\hbar m_e}M - \frac{ie^2F_1F_2}{2\beta\hbar m_e\omega^2}N\right), \quad x \ge 0 \tag{14}$$

where 
$$\xi = x + \frac{eF_1\cos(\omega t)}{m_e\omega^2} + \frac{eF_2\cos(\beta\omega t + \theta)}{m_e\beta^2\omega^2}$$
,  $L = \frac{F_1\sin(\omega t)}{\omega} + \frac{F_2\sin(\beta\omega t + \theta)}{\beta\omega}$ ,  $M = \frac{F_1^2\sin(2\omega t)}{\omega^3} + \frac{F_2\sin(2\omega t)}{\omega^3}$ 

 $\frac{F_2^2 \sin(2\beta\omega t + 2\theta)}{\beta^3\omega^3}$ ,  $N = \frac{\sin[(\beta-1)\omega t + \theta]}{(\beta-1)\omega} - \frac{\sin[(\beta+1)\omega t + \theta]}{(\beta+1)\omega}$ ,  $T_n$  is the transmission coefficient, the drift kinetic energy  $E_n = \varepsilon + n\hbar\omega - E_F - W - U_{p1} - U_{p2}$ , the ponderomotive energies  $U_{p1} = e^2 F_1^2 / 4m_e\omega^2$ , and  $U_{p2} = e^2 F_2^2 / 4m_e\beta^2\omega^2$ , and  $\varepsilon$  is the electron initial energy. Because of the time periodicity, Equation (14) represents the superposition of transmitted electron plane waves with energies  $\varepsilon + n\hbar\omega$ , due to multiphoton absorption (n > 0), tunneling (n = 0), and multiphoton

For x < 0, the solution to Equation (13) is [61],

emission (n < 0) [6][76].

$$\psi(x,t) = \exp\left(-\frac{i\varepsilon t}{\hbar} + ik_0 x\right) + \sum_{n=-\infty}^{\infty} R_n \exp\left(-i\frac{\varepsilon + n\hbar\omega}{\hbar}t - ik_n x\right), \quad x < 0$$
 (15)

which denotes the superposition of an incident wave and a set of reflected waves, where  $k_0 = \sqrt{2m_e\varepsilon/\hbar^2}$ ,  $k_n = \sqrt{2m_e(\varepsilon + n\hbar\omega)/\hbar^2}$ , and  $R_n$  is the reflection coefficient. It has been verified that most of the reflected current is through the initial energy level (n = 0) [6].

By matching the solutions in Equations (14) and (15) from the boundary conditions that both  $\psi(x,t)$  and  $\partial \psi(x,t)/\partial x$  are continuous at x=0, and taking Fourier transform, we obtain, in nondimensional quantities [6],  $\bar{\varepsilon}=\varepsilon/W$ ,  $\bar{\omega}=\omega\hbar/W$ ,  $\bar{t}=tW/\hbar$ ,  $\bar{E}_F=E_F/W$ ,  $\bar{x}=x/\lambda_0$ ,  $\lambda_0=\sqrt{\hbar^2/2m_eW}$ ,  $\bar{F}_1=F_1e\lambda_0/W$ ,  $\bar{F}_2=F_2e\lambda_0/W$ ,  $\bar{U}_{p1}=U_{p1}/W$ ,  $\bar{U}_{p2}=U_{p2}/W$ , the following equation,

$$2\sqrt{\bar{\varepsilon}}\delta(l) = \sum_{n=-\infty}^{\infty} T_n \left[ \sqrt{\bar{\varepsilon} + l\bar{\omega}} P_{n(n-l)} + Q_{n(n-l)} \right], \tag{16}$$

where  $\delta(l)$  is the Dirac delta function, and  $P_{n(n-l)}$ , and  $Z_{n(n-l)}$  are given by,

$$P_{nl} = \frac{1}{2\pi} \int_{0}^{2\pi} p_{n}(\overline{\omega}\overline{t}) e^{-il\overline{\omega}\overline{t}} d(\overline{\omega}\overline{t}), \quad Q_{nl} = \frac{1}{2\pi} \int_{0}^{2\pi} p_{n}(\overline{\omega}\overline{t}) z_{n}(\overline{\omega}\overline{t}) e^{-il\overline{\omega}\overline{t}} d(\overline{\omega}\overline{t}), \quad (17a)$$

$$p_n(\bar{\omega}\bar{t}) = q(\bar{\omega}\bar{t})f(\bar{\omega}\bar{t}), \ z_n(\bar{\omega}\bar{t}) = \sqrt{\bar{E}_n} + \frac{\bar{F}_1}{\bar{\omega}}\sin(\bar{\omega}\bar{t}) + \frac{\bar{F}_2}{\beta\bar{\omega}}\sin(\beta\bar{\omega}\bar{t} + \theta), \tag{17b}$$

$$q(\bar{\omega}\bar{t}) = e^{i2\sqrt{\bar{E}_n}\left[\frac{\bar{F}_1\cos(\bar{\omega}\bar{t})}{\bar{\omega}^2} + \frac{\bar{F}_2\cos(\beta\bar{\omega}\bar{t} + \theta)}{\beta^2\bar{\omega}^2}\right]},$$
(17c)

$$f(\overline{\omega}\overline{t}) = e^{i\left[\frac{\overline{F}_{1}^{2}\sin(2\overline{\omega}\overline{t})}{4\overline{\omega}^{3}} + \frac{\overline{F}_{2}^{2}\sin(2\beta\overline{\omega}\overline{t} + 2\theta)}{4\beta^{3}\overline{\omega}^{3}}\right]}$$

$$\times e^{-\frac{i\overline{F}_{1}\overline{F}_{2}}{\beta\overline{\omega}^{2}}\left\{\frac{\sin[(\beta-1)\overline{\omega}\overline{t} + \theta]}{(\beta-1)\overline{\omega}} - \frac{\sin[(\beta+1)\overline{\omega}\overline{t} + \theta]}{(\beta+1)\overline{\omega}}\right\}},$$
(17d)

with  $\bar{E}_n = \bar{\varepsilon} + n\bar{\omega} - \bar{E}_F - \bar{U}_{p1} - \bar{U}_{p2} - 1$ . Since Equation (17) is derived from the conditions that electron wave function and its first derivative are continuous at the metal-vacuum interface (x = 0),  $p_n$  and  $z_n$  in Equation (17b) denote the phase factor of the wave function in the nth state and of its spatial derivative at  $\bar{x} = 0$ , respectively.  $P_{nl}$  and  $Q_{nl}$  are the lth Fourier coefficients of  $p_n$  and the product of  $p_n$  and  $z_n$ , respectively. The transmission coefficient  $T_n$  (and therefore the reflection coefficient  $R_n$ ) is obtained from Equation (16). The emission current density is then calculated from the probability current density  $J(x,t) = (i\hbar/2m)(\psi\partial\psi^*/\partial x - \psi^*\partial\psi/\partial x) = (i\hbar/2m_e)\sum_{n=-\infty}^{\infty}\sum_{l=-\infty}^{\infty}(\psi_n\,\partial\psi_l^*/\partial x - \psi_n^*\,\partial\psi_l\partial x)$ , where  $\psi(x,t) = \sum_{n=-\infty}^{\infty}\psi_n(x,t)$  is obtained from Equation (14).

The normalized emission current density, defined as the ratio of the transmitted probability current density over the incident probability current density,  $w(\varepsilon, x, t) = J_t(\varepsilon, x, t)/J_i(\varepsilon, x, t)$ , is found in nondimensional form as,

$$w(\bar{\varepsilon}, \bar{x}, \bar{t}) = \frac{1}{\sqrt{\bar{\varepsilon}}} \sum_{n=-\infty}^{\infty} \sum_{l=-\infty}^{\infty} Re \left[ e^{i(l-n)\bar{\omega}\bar{t}} T_n T_l^* e^{i\Theta} D \right], \tag{18}$$

where 
$$\Theta = \left[\sqrt{\overline{E}_n} - \left(\sqrt{\overline{E}_l}\right)^*\right] \left[\bar{x} + \frac{2\bar{F}_1}{\bar{\omega}^2}\cos(\bar{\omega}\bar{t}) + \frac{2\bar{F}_2}{\beta^2\bar{\omega}^2}\cos(\beta\bar{\omega}\bar{t} + \theta)\right]$$
, and  $D = \left(\sqrt{\overline{E}_l}\right)^* + \frac{2\bar{F}_2}{\beta^2\bar{\omega}^2}\cos(\beta\bar{\omega}\bar{t} + \theta)$ 

 $\frac{\overline{F_1}}{\overline{\omega}}\sin(\overline{\omega}\overline{t}) + \frac{\overline{F_2}}{\beta\overline{\omega}}\sin(\beta\overline{\omega}\overline{t} + \theta)$ . The normalized time-averaged emission current density is found to be,

$$\langle w(\bar{\varepsilon}) \rangle = \sum_{n=-\infty}^{\infty} \langle w_n(\bar{\varepsilon}) \rangle, \quad \langle w_n(\bar{\varepsilon}) \rangle = \text{Re}\left( |T_n|^2 \sqrt{\bar{E}_n/\bar{\varepsilon}} \right),$$
 (19)

where  $\langle w_n \rangle$  represents the emission current density through the *n*th channel, with emitted electrons of energy  $\varepsilon + n\hbar\omega$  due to the *n*-photon contribution.

#### 2.2.2 Results and Discussion

In this chapter, unless mentioned otherwise, the default values for the calculation are as follows: the wavelength of the fundamental laser field  $F_1$  is 800 nm ( $\hbar\omega=1.55$  eV), the harmonic laser field  $F_2$  is with the frequency of  $2\omega$  (i.e.  $\beta=2$ ), the metal is assumed to be gold [6][11][56][61][62][76], with Fermi energy  $E_F$ =5.33 eV and the work function W=5.1 eV, and since most of the emission electrons from sources are located near the Fermi level [6][61][62][76][86][87], we choose the electron initial energy  $\varepsilon=E_F$  for simplicity.

First, in order to understand the detailed underlying emission processes, the photoelectron energy spectra, under different two-color laser fields  $F_1$  (at frequency  $\omega$ ) and  $F_2$  (at second harmonic  $2\omega$ ), for various phase differences  $\theta$  between two laser fields are displayed in Figure

2.2. It can be seen that the dominant emission process is the four-photon absorption (n = 4) for the fundamental laser (or two-photon absorption for the second-harmonic laser), where electrons at the Fermi level need to absorb at least four photons to overcome the potential barrier  $(W/\hbar\omega =$ 3.29) (see Figure 2.1). The tunneling emission channels (n < 4) is closed. When the two laser fields are in phase ( $\theta = 0$ ), the photoelectron emission spectrum becomes broader and the total emission current density  $\langle w \rangle = \sum_n \langle w_n \rangle$  increases when either  $F_1$  or  $F_2$  increases, since more channels open up for electron emission. When  $F_1$  is small (see Figure 2.2(a)), the emission spectrum is very close to that driven by the second harmonic laser  $F_2$  alone, indicating  $F_2$ dominates the emission process. As  $F_1$  increases (from Figure 2.2(a) to 2.2(e)), the emission spectrum gradually transits to that driven by  $F_1$  alone, indicating the laser field dominating the emission process changes from  $F_2$  to  $F_1$ . During the transition process, the competition between  $F_1$  and  $F_2$  for dominating the electron emission process causes the dip in Figure 2.2(c). In Figures 2.2(d) and 2.2(e), the dip shifts to larger n as  $F_1$  increases, due to the channel closing effect [6][76]. When either  $F_1 = 0$  or  $F_2 = 0$ , the results recover those of single frequency laser induced photoemission [6][76]. Figures 2.2(f)-(j) show that the emission spectra can be greatly modified as  $\theta$  changes, due to the interference effect between two lasers. For example, when  $\theta$  changes from  $\pi/2$  to  $3\pi/2$ , the emission process with the highest probability shifts from the four-photon (n = 4) to five-photon (n = 5) absorption.

Figure 2.3 shows the normalized total time-averaged emission current density  $\langle w \rangle$  under various combinations of  $F_1$  and  $F_2$ , for the phase difference  $\theta = 0$  and  $\pi$ . In Figures 2.3(a) and 2.3(b), when  $F_2$  is small  $(F_1/F_2 > 10)$ ,  $\langle w \rangle$  is insensitive to  $F_2$ , because the fundamental laser  $F_1$  dominates the emission process. As  $F_2$  increases, the current density gradually approaches the scale  $\langle w \rangle \propto F_2^{2n}$  with n=2 (see Figures 2.3(a) and 2.3(b)), indicating two-photon absorption for the second-

harmonic laser (or four-photon with respect to the fundamental laser) is the main emission process. The gradual change of the slope of  $\langle w \rangle$  is due to the opening of higher emission channels, as seen in Figure 2.2. When  $\theta=\pi$  (see Figure 2.3 (b)), a series of new dips appear in the curves as compared to those when  $\theta=0$  (see Figure 2.3 (a)), indicating strong interference effects between the two lasers. The interference effect is also reflected in that the total current density  $\langle w \rangle$  with  $F_1=1$  V/nm changes from being larger than  $\langle w \rangle$  with  $F_1=0$  to being smaller (see the green and dark blue lines in Figures 2.3(a) and 2.3(b)). The sharp drops of  $\langle w \rangle$  at  $F_2=13$  V/nm in Figures 2.3 (a) and 2.3(b) are due to the channel closing effect [6][76],which is accurately predicted by taking  $E_4=\varepsilon+4\hbar\omega-E_F-W-U_{p1}-U_{p2}=0$ , giving  $F_2=12.4$  V/nm. Similar behaviors of  $\langle w \rangle$  as a function of  $F_1$  are observed in Figures 2.3 (c) and 2.3(d).

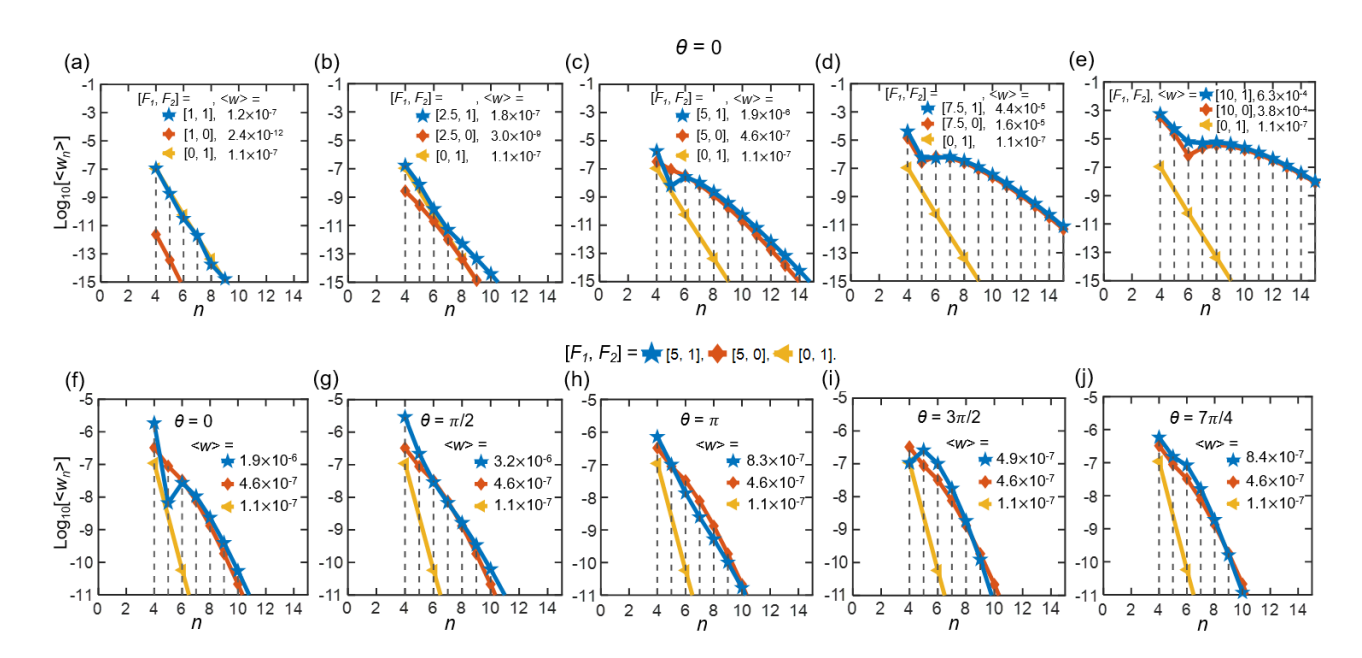


Figure 2.2: Photoelectron energy spectra, calculated from Equation (19). (a)-(e) Energy spectra under different combinations of two-color laser fields  $F_1$  (at frequency  $\omega$ ) and  $F_2$  (at frequency  $2\omega$ ), for the special case of  $\theta = 0$ . (f)-(j) Energy spectra for various phase differences  $\theta$ . The unit of laser fields  $F_1$  and  $F_2$  is V/nm in all figures.

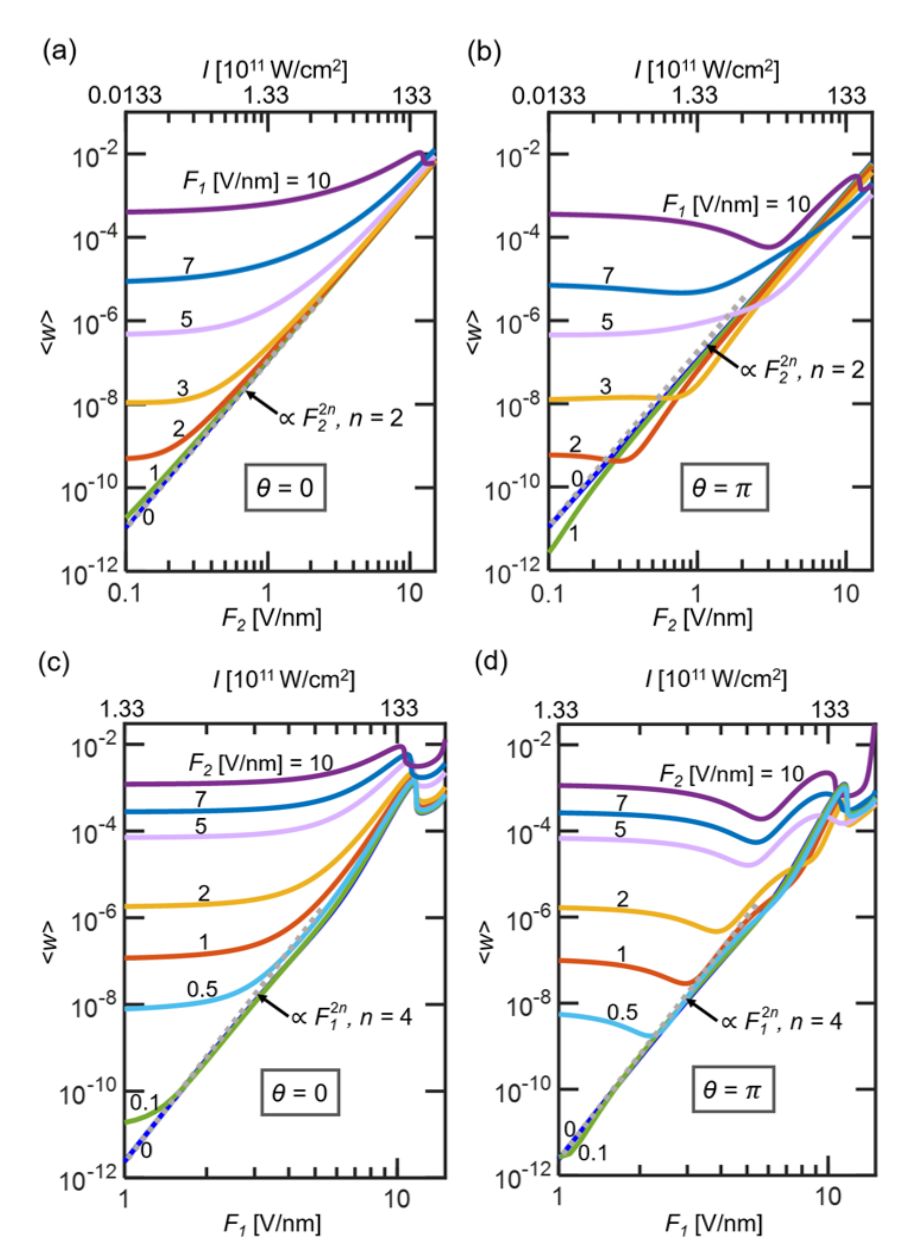


Figure 2.3: Normalized total time-averaged emission current density for the phase differences  $\theta = 0$  and  $\pi$ . (a)-(b) total time-averaged current density  $\langle w \rangle$  as a function of the second-harmonic laser field  $F_2$ , under various fundamental laser fields  $F_1$ . (c)-(d)  $\langle w \rangle$  as a function of  $F_1$ , under various  $F_2$ . The laser intensity is related to the laser electric field as  $I[W/cm^2] = 1.33 \times 10^{11} \times (F_1[V/nm])^2$ . The dotted lines represent the scale  $\langle w \rangle \propto F^{2n}$ .

The total time-averaged emission current density  $\langle w \rangle$  as a function of  $\theta$  is shown in Figures 2.4(a)-2.4(c), for various  $2\omega$  laser fields  $F_2$  with fixed  $F_1=1.6$  V/nm. The total emission current density  $\langle w \rangle$  oscillates as a sinusoidal function of  $\theta$ , showing striking resemblance to the experimentally measured emission current (see Figure 2(b) in Reference [57]). As  $F_2$  decreases,

the maximum and minimum of  $\langle w \rangle$  both decrease, but the corresponding  $\theta$  for the maximum and minimum  $\langle w \rangle$  remain almost unchanged. The modulation depth, defined as  $\Gamma = (\langle w \rangle_{max} - \langle w \rangle_{max})$  $\langle w \rangle_{min} / (\langle w \rangle_{max} + \langle w \rangle_{min})$ , reaches a maximum value of approximately 99% when  $F_2/F_1 =$ 0.1375 (or intensity ratio of 2%). For tungsten and the fundamental laser wavelength of 1560 nm as in Reference [57], we obtain the modulation depth of 95.5% and of 93.9%, when setting the work function in Equation (12) to be 4.3 eV and 3.6 eV (effective work function with Schottky effect), respectively. The latter is almost identical to the experimentally measured modulation depth of 94% in Reference [57]. Despite the excellent agreement between the theoretical predictions and experimental results, we should stress that our model assumed one-dimensional flat metal surface, whereas the experiment used nanometer scale sharp emitter [57]. The sharpness of the emitter may introduce varying field enhancement and Schottky lowering factor along the emission surface, nonuniform off-tip electron emission [53], and even quantized energy levels inside the emitter [88]. In addition, our model neglects the image charge potential, laser pulse shape, laser penetration depth, incident electron energy distribution inside the meal, and surface effects (e.g., local surface roughness, grain boundaries, and different crystal plane terminations). As  $F_2$  further decreases,  $\Gamma$  drops. When  $F_2$  reaches 0,  $\langle w \rangle$  becomes a constant, with zero  $\Gamma$  as expected, as shown in Figure 2.4(c). Figure 2.4(d) compares the electron energy spectra at the peak and valley of the current modulation for  $F_2/F_1 = 0.1375$ , where the dominant emission process shifts from four-photon to five-photon absorption. Figure 2.4(e) summarizes the modulation depth  $\Gamma$  as a function of  $F_2/F_1$ , for different strengths of the fundamental  $\omega$  laser field  $F_1$ . As the  $\omega$  laser field  $F_1$  increases, the location of the peak modulation depth shifts to larger  $F_2/F_1$ , since a larger  $2\omega$  laser field  $F_2$  is needed to balance the increase of  $F_1$  for achieving the same modulation depth.

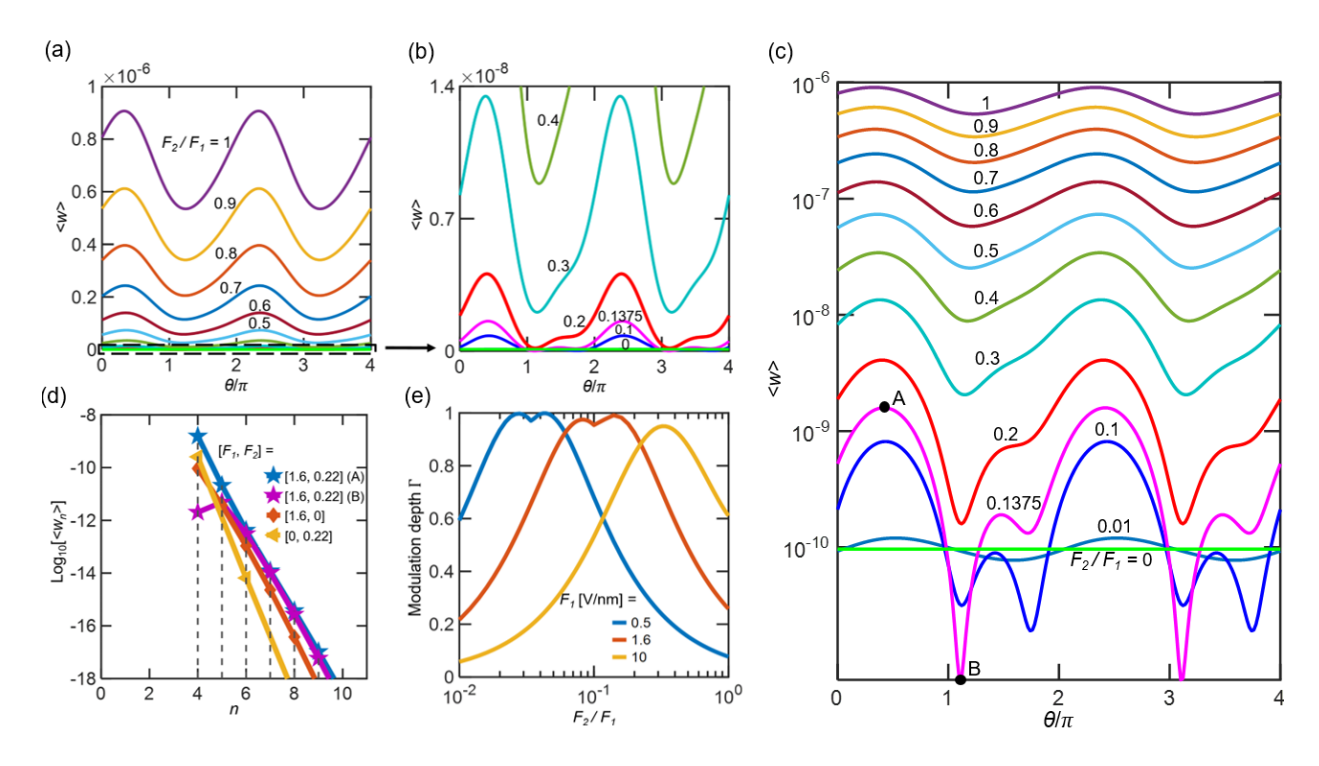


Figure 2.4: Current modulation depth. (a) Normalized total time-averaged emission current density  $\langle w \rangle$  as a function of the phase difference  $\theta$ , under different  $F_2/F_1$ . (b) Magnification of the bottom area of (a). (c) Semi-log plot of  $\langle w \rangle$  in (a).  $F_1$  is fixed at 1.6 V/nm in (a)-(c). (d) Electron energy spectra of  $\langle w \rangle_{max}$  (point A) and  $\langle w \rangle_{min}$  (point B) for  $F_2/F_1=0.1375$  in (c). (e) Current modulation depth  $\Gamma$  as a function of the field ratio  $F_2/F_1$  for different  $F_1=0.5$ , 1.6, and 10 V/nm.

Figure 2.5 shows the time-dependent electron emission current density  $w(\bar{x}, t)$  as a function of the space  $\bar{x}$  and time t, for  $\omega$  laser field  $F_1 = 1.6$  V/nm and  $2\omega$  laser field  $F_2 = 0.22$  V/nm (experimental laser parameters in Reference [57]). When  $\bar{x}$  is greater than 20 (beyond the strong surface current oscillation region), the emission current keeps the same temporal profile with only a phase shift as  $\bar{x}$  increases (see Figures 2.5(a) and 2.5(b)), which is primarily due to the drift and acceleration motion of electrons under the influence of laser fields. As the phase difference  $\theta$  varies from 0 to  $\pi$ ,  $w(\bar{x}, t)$  becomes significantly smaller, due to the interference effect of two lasers, which also causes the total time-averaged emission current density  $\langle w \rangle$  to decrease from  $5.23 \times 10^{-10}$  to  $7.31 \times 10^{-11}$ . Figures 2.5(c) and 2.5(d) show the total emission current density w(t) at  $\bar{x} = 100$  as a function of time t. It is shown that w(t) and the total laser field F(t) have a

clear phase shift, which means the peak value of time-dependent total emission current density does not occur at the peak value of the total incident laser field. As the phase difference  $\theta$  changes, the temporal profile of emission current density  $w(\bar{x},t)$  for a fixed  $\bar{x}$  also has a phase shift due to the interference effect between the two lasers. The full width at half maximum (FWHM) of the modulation of the ultrafast current pulses in Figure 2.5 is approximately 0.62 fs, which is significantly shorter than the period of the fundamental laser period of 2.67 fs.

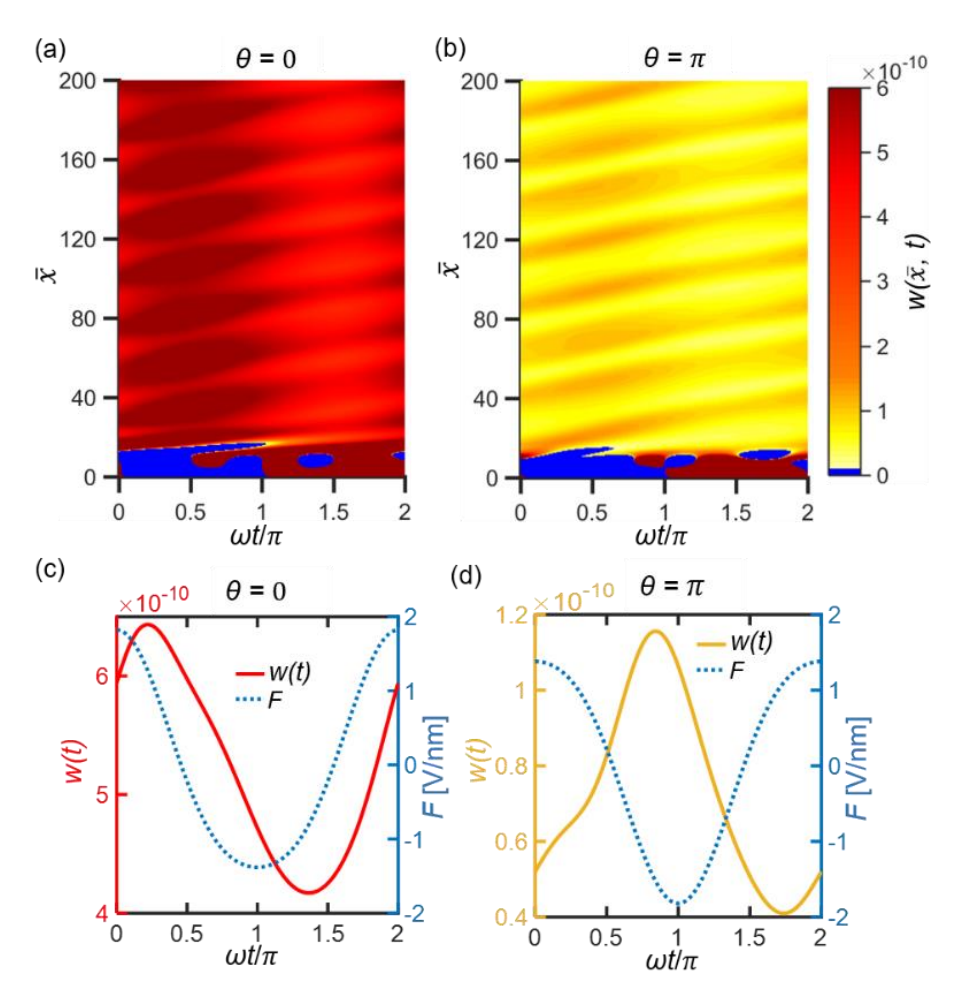


Figure 2.5: Total time-dependent emission current density for the phase differences  $\theta=0$  and  $\pi$ . (a)-(b) Total time-dependent emission current density  $w(\bar{x},t)$  as a function of the space  $\bar{x}$  and time t. (c)-(d) Total emission current density w(t) at  $\bar{x}=100$  as a function of time t. Dotted lines in (c) and (d) are for the total time-dependent laser field  $F=F_1\cos(\omega t)+F_2\cos(\beta\omega t+\theta)$ . The fundamental laser field  $F_1=1.6$  V/nm. The second harmonic ( $\beta=2$ ) laser field  $F_2=0.22$  V/nm (experimental laser parameters in Reference [57]). When  $\theta=0$ , the normalized time-averaged emission current density  $\langle w \rangle = 5.23 \times 10^{-10}$ ; when  $\theta=\pi$ ,  $\langle w \rangle = 7.31 \times 10^{-11}$ .

The effects of harmonic number  $\beta$  on the emission current modulation  $\Gamma$  are shown in Figure 2.6. As  $\beta$  increases, modulation depth  $\Gamma$  decreases, due to the reduced interference between the two-color lasers. Note that superimposing the fourth harmonic laser ( $\beta = 4$ ) on the fundamental laser leads to the largest  $\langle w \rangle_{max}$  and  $\langle w \rangle_{min}$ . This is in agreement with the prediction [6] that the maximum emission current occurs when the single photon energy (that is the fourth harmonic photon here) roughly equals the potential barrier,  $4\hbar\omega/W \approx 1$ .

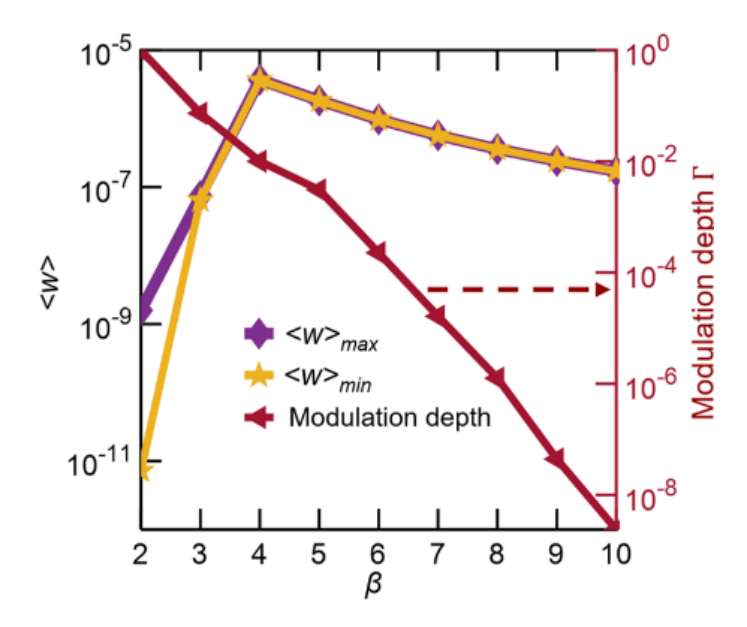


Figure 2.6: Effects of the harmonic order. The emission current modulation depth  $\Gamma$ , the maximum and minimum time-averaged current density,  $\langle w \rangle_{max}$  and  $\langle w \rangle_{min}$  as a function of harmonic order  $\beta$ . The fundamental laser field  $F_1$  and the harmonic laser field  $F_2$  are 1.6 V/nm and 0.22 V/nm, respectively (intensity ratio of 2%).

# 2.2.3 Summary on Photoemission without DC Bias

In this section, an analytical model for ultrafast electron emission from a metal surface due to two-color lasers is constructed, by solving the TDSE exactly. Our model demonstrates great tunability on the photoelectron spectra, emission current, and current modulation, via the control of the phase delay, relative intensity, and harmonic order of the two-color lasers. We identify the condition for the maximum emission current modulation depth (99%) by superimposing a weak harmonic laser

on a fundamental laser. Using the same input parameters, our theoretical prediction for the photoemission current modulation depth (93.9%) is almost identical to the experimental results (94%). Such two-color induced photoemission may inspire new route towards the design of future ultrafast nanoelectronics.

#### 2.3 Photoemission with DC bias

# 2.3.1 Analytical model

The addition of dc bias to the metal makes the potential barrier near the metal-vacuum interface at x = 0 narrower, compared to the case without dc bias (see Figure 2.7). The time-dependent potential barrier near the interface reads [62],

$$\Phi(x,t) = \begin{cases} 0, & x < 0 \\ V_0 - eF_0x - eF_1x\cos(\omega t) - eF_2x\cos(\beta \omega t + \theta), & x \ge 0, \end{cases}$$
 (20)

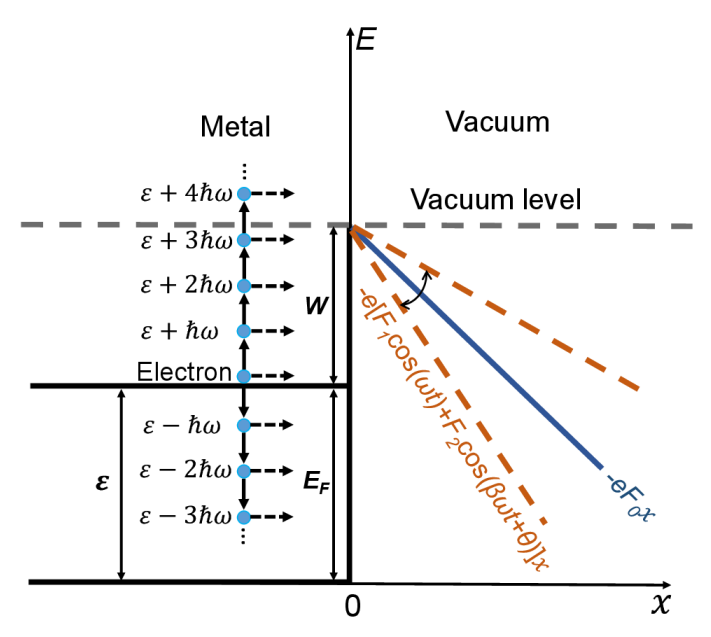


Figure 2.7: Energy diagram for photoemission under two-color laser fields and a dc bias. Electrons with initial energy  $\varepsilon$  are emitted from the dc biased metal-vacuum interface at x=0, with the transmitted energy of  $\varepsilon+n\hbar\omega$ , due to the n-photon contribution [multiphoton absorption (n>0), tunneling (n=0), and multiphoton emission (n<0)], where n is an integer. The fundamental and harmonic laser fields are  $F_1\cos(\omega t)$  and  $F_2\cos(\beta\omega t+\theta)$ , respectively. The dc electric field is  $F_0$ . The photon energy of the fundamental (harmonic) laser is  $\hbar\omega$   $(\beta\hbar\omega)$ .  $E_F$  and W are the Fermi energy and work function of the metal, respectively.

where  $F_0$  is the applied dc electric field which is assumed to be perpendicular to the flat metal surface. Other parameters have the same definition as that in Equation (12).

By solving the TDSE subjected to the potential energy given in Equation (20), the exact solution for  $x \ge 0$  is found to be [62] (see Appendix B for the method),

$$\psi(x,t) = \sum_{n=-\infty}^{\infty} T_n[Ai(-\eta_n) - iBi(-\eta_n)] \times \exp\left(-i\frac{\varepsilon}{\hbar}t - in\omega t\right)$$

$$\times \exp\left(\frac{ie}{\hbar}Lx + \frac{ie^2}{8\hbar m_e}M - \frac{ie^2F_1F_2}{2\beta\hbar m_e\omega^2}N - \frac{ie^2F_0}{\hbar m_e}Q\right), \quad x \ge 0$$
 (21)

$$\text{where} \quad L = \frac{F_1 \sin(\omega t)}{\omega} + \frac{F_2 \sin(\beta \omega t + \theta)}{\beta \omega} \ , \quad M = \frac{F_1^2 \sin(2\omega t)}{\omega^3} + \frac{F_2^2 \sin(2\beta \omega t + 2\theta)}{\beta^3 \omega^3} \ , \quad N = \frac{\sin[(\beta - 1)\omega t + \theta]}{(\beta - 1)\omega} - \frac{\sin[(\beta - 1)\omega t + \theta]}{(\beta - 1$$

$$\frac{\sin[(\beta+1)\omega t+\theta]}{(\beta+1)\omega} \qquad , \qquad Q = \frac{F_1\sin(\omega t)}{\omega^3} + \frac{F_2\sin(\beta\omega t+\theta)}{\beta^3\omega^3} \qquad , \qquad \eta_n = \big[\frac{E_n}{eF_0} + x + \frac{eF_1\cos(\omega t)}{m_e\omega^2} + \frac{eF_1\cos(\omega t)$$

 $\frac{eF_2\cos(\beta\omega t+\theta)}{m_e\beta^2\omega^2}](\frac{2em_eF_0}{\hbar^2})^{\frac{1}{3}}$ , the drift kinetic energy  $E_n=\varepsilon+n\hbar\omega-E_F-W-U_{p1}-U_{p2}$ , the ponderomotive energies  $U_{p1}=e^2F_1^2/4m_e\omega^2$ , and  $U_{p2}=e^2F_2^2/4m_e\beta^2\omega^2$ , Ai and Bi are the Airy functions of the first kind and second kind respectively, showing an outgoing wave traveling to the +x direction (see Figure 2.7) [6][62][82][86],  $T_n$  represents the transmission coefficient, and  $\varepsilon$  is the initial energy of the electron. It is easy to find that Equation (21) is periodic with the time period of  $2\pi/\omega$ , therefore Equation (21) is readily to be recast into a Fourier series, which denotes the superposition of transmitted traveling electron waves with energies  $\varepsilon+n\hbar\omega$ . These ladder eigenenergies are made possible by multiphoton absorption (n>0), tunneling (n=0), and multiphoton emission (n<0) [6][61][62][76].

The exact solution of electron wavefunction for x < 0 is,

$$\psi(x,t) = \exp\left(-\frac{i\varepsilon t}{\hbar} + ik_0 x\right) + \sum_{n=-\infty}^{\infty} R_n \exp\left(-i\frac{\varepsilon + n\hbar\omega}{\hbar}t - ik_n x\right), \quad x < 0$$
 (22)

which denotes the superposition of an incident plane wave and a set of reflected waves with reflection coefficient  $R_n$  and energies  $\varepsilon + n\hbar\omega$ , where  $k_0 = \sqrt{2m\varepsilon/\hbar^2}$ , and  $k_n = \sqrt{2m(\varepsilon + n\hbar\omega)/\hbar^2}$ .

Applying the boundary conditions that both  $\psi(x,t)$  and  $\partial \psi(x,t)/\partial x$  are continuous at x=0, Fourier transform yields, in nondimensional quantities [6][61][62],  $\bar{\varepsilon}=\varepsilon/W$ ,  $\bar{\omega}=\omega\hbar/W$ ,  $\bar{t}=tW/\hbar$ ,  $\bar{E}_F=E_F/W$ ,  $\bar{x}=x/\lambda_0$ ,  $\lambda_0=\sqrt{\hbar^2/2m_eW}$ ,  $\bar{F}_0=F_0e\lambda_0/W$ ,  $\bar{F}_1=F_1e\lambda_0/W$ ,  $\bar{F}_2=F_2e\lambda_0/W$ ,  $\bar{U}_{p1}=U_{p1}/W$ ,  $\bar{U}_{p2}=U_{p2}/W$ , the following equations,

$$2\sqrt{\bar{\varepsilon}}\delta(l) = \sum_{n=-\infty}^{\infty} T_n \left[ \sqrt{\bar{\varepsilon} + l\bar{\omega}} P_{n(n-l)} + Q_{n(n-l)} \right], \tag{23}$$

where  $\delta(l)$ ,  $P_{n(n-l)}$ , and  $Q_{n(n-l)}$  are given by,

$$\delta(l) = \begin{cases} 1, & l = 0, \\ 0, & l \neq 0, \end{cases} \tag{24a}$$

$$P_{nl} = \frac{1}{2\pi} \int_0^{2\pi} p_n(\overline{\omega}\overline{t}) e^{-il\overline{\omega}\overline{t}} d(\overline{\omega}\overline{t}), \quad Q_{nl} = \frac{1}{2\pi} \int_0^{2\pi} q_n(\overline{\omega}\overline{t}) e^{-il\overline{\omega}\overline{t}} d(\overline{\omega}\overline{t}), \quad (24b)$$

$$p_n(\overline{\omega}\overline{t}) = \phi(\overline{\omega}\overline{t})[Ai(\alpha_n) - iBi(\alpha_n)], \tag{24c}$$

$$q_n(\overline{\omega}\overline{t}) = \phi(\overline{\omega}\overline{t})z_n(\overline{\omega}\overline{t}), \tag{24d}$$

$$\phi(\bar{\omega}\bar{t}) = e^{i\bar{M} - \frac{i\bar{F}_1\bar{F}_2}{\beta\bar{\omega}^2}\bar{N}} \times e^{-i2\bar{F}_0\bar{Q}},$$
(24e)

$$z_n(\overline{\omega}\overline{t}) = \overline{L}[Ai(\alpha_n) - iBi(\alpha_n)] + \frac{\overline{F_0}^{1/3}}{\lambda_0}[iAi'(\alpha_n) + Bi'(\alpha_n)], \tag{24f}$$

with 
$$\bar{L} = \frac{\bar{F}_1}{\bar{\omega}} \sin(\bar{\omega}\bar{t}) + \frac{\bar{F}_2}{\beta\bar{\omega}} \sin(\beta\bar{\omega}\bar{t} + \theta)$$
,  $\bar{M} = \frac{\bar{F}_1^2 \sin(2\bar{\omega}\bar{t})}{4\bar{\omega}^3} + \frac{\bar{F}_2^2 \sin(2\beta\bar{\omega}\bar{t} + 2\theta)}{4\beta^3\bar{\omega}^3}$ ,  $\bar{N} = \frac{\sin[(\beta - 1)\bar{\omega}\bar{t} + \theta]}{(\beta - 1)\bar{\omega}} - \frac{\sin[(\beta - 1)\bar{\omega}\bar{t} + \theta]}{(\beta - 1)\bar{\omega}}$ 

$$\frac{\sin[(\beta+1)\bar{\omega}\bar{t}+\theta]}{(\beta+1)\bar{\omega}}\quad,\quad \bar{Q}=\frac{\bar{F}_1}{\bar{\omega}^3}\sin(\bar{\omega}\bar{t})+\frac{\bar{F}_2}{\beta^3\bar{\omega}^3}\sin(\beta\bar{\omega}\bar{t}+\theta)\quad,\quad \alpha_n=-\bar{F}_0^{\frac{1}{3}}[\frac{\bar{E}_n}{\bar{F}_0}+\frac{2\bar{F}_1}{\bar{\omega}^2}\cos(\bar{\omega}\bar{t})+\frac{2\bar{F}_2}{\bar{G}_0}\sin(\beta\bar{\omega}\bar{t})+\frac{2\bar{G}_0}{\bar{G}_0}\sin(\beta\bar{\omega}\bar{t})+\frac{2\bar{G}_0}{\bar{G}_0}\sin(\beta\bar{\omega}\bar{t})+\frac{2\bar{G}_0}{\bar{G}_0}\sin(\beta\bar{\omega}\bar{t})+\frac{2\bar{G}_0}{\bar{G}_0}\sin(\beta\bar{\omega}\bar{t})+\frac{2\bar{G}_0}{\bar{G}_0}\sin(\beta\bar{\omega}\bar{t})+\frac{2\bar{G}_0}{\bar{G}_0}\sin(\beta\bar{\omega}\bar{t})+\frac{2\bar{G}_0}{\bar{G}_0}\sin(\beta\bar{\omega}\bar{t})+\frac{2\bar{G}_0}{\bar{G}_0}\sin(\beta\bar{\omega}\bar{t})+\frac{2\bar{G}_0}{\bar{G}_0}\sin(\beta\bar{\omega}\bar{t})+\frac{2\bar{G}_0}{\bar{G}_0}\sin(\beta\bar{\omega}\bar{t})+\frac{2\bar{G}_0}{\bar{G}_0}\sin(\beta\bar{\omega}\bar{t})+\frac{2\bar{G}_0}{\bar{G}_0}\sin(\beta\bar{\omega}\bar{t})+\frac{2\bar{G}_0}{\bar{G}_0}\sin(\beta\bar{\omega}\bar{t})+\frac{2\bar{G}_0}{\bar{G}_0}\sin(\beta\bar{\omega}\bar{t})+\frac{2\bar{G}_0}{\bar{G}_0}\sin(\beta\bar{\omega}\bar{t})+\frac{2\bar{G$$

$$\frac{{}_2\bar{F}_2}{\beta^2\bar{\omega}^2}\cos(\beta\bar{\omega}\bar{t}+\theta)], \text{ and } \bar{E}_n=\bar{\varepsilon}+n\bar{\omega}-\bar{E}_F-\bar{U}_{p1}-\bar{U}_{p2}-1. \ p_n(\bar{\omega}\bar{t}) \text{ and } q_n(\bar{\omega}\bar{t}) \text{ in Equations}$$

(24c) and (24d) represent the phase factor of the *n*th-state wave function and of its spatial derivative at  $\bar{x}=0$  respectively.  $P_{nl}$  and  $Q_{nl}$  are the *l*th Fourier coefficients of  $p_n$  and  $q_n$  respectively. The transmission coefficient  $T_n$  (and therefore the reflection coefficient  $R_n$ ) is calculated from Equation (23).

The normalized emission current density is defined as the ratio of the transmitted probability current density over the incident probability current density,  $w(\varepsilon, x, t) = J_t(\varepsilon, x, t)/J_i(\varepsilon, x, t)$ , where the probability current density is  $J(x,t) = (i\hbar/2m)(\psi\partial\psi^*/\partial x - \psi^*\partial\psi/\partial x) = (i\hbar/2m)\sum_{n=-\infty}^{\infty} \sum_{l=-\infty}^{\infty} (\psi_n \partial \psi_l^*/\partial x - \psi_n^* \partial \psi_l \partial x)$ . Thus, the normalized instantaneous emission current density is found as,

$$w(\bar{\varepsilon}, \bar{x}, \bar{t}) = \frac{1}{\sqrt{\bar{\varepsilon}}} \sum_{n=-\infty}^{\infty} \sum_{l=-\infty}^{\infty} \operatorname{Im} \left[ e^{i(l-n)\bar{\omega}\bar{t}} T_n T_l^* (C+iD) \right], \tag{25a}$$

$$C = \overline{L}[Ai(-\overline{\eta_l})Bi(-\overline{\eta_n}) - Ai(-\overline{\eta_n})Bi(-\overline{\eta_l})]$$

$$+ \bar{F}_0^{1/3} [Ai(-\overline{\eta_n})Ai'(-\overline{\eta_l}) + Bi(-\overline{\eta_n})Bi'(-\overline{\eta_l})], \tag{25b}$$

$$D = \overline{L}[Ai(-\overline{\eta_l})Ai(-\overline{\eta_n}) + Bi(-\overline{\eta_l})Bi(-\overline{\eta_n})]$$

$$+ \bar{F}_0^{1/3} [Ai(-\overline{\eta_n})Bi'(-\overline{\eta_l}) - Bi(-\overline{\eta_n})Ai'(-\overline{\eta_l})], \tag{25c}$$

where  $\overline{\eta_n} = \overline{F_0}^{1/3} \left[ \frac{\overline{E_n}}{\overline{F_0}} + \frac{2\overline{F_1}}{\overline{\omega}^2} \cos(\overline{\omega} \overline{t}) + \frac{2\overline{F_2}}{\beta^2 \overline{\omega}^2} \cos(\beta \overline{\omega} \overline{t} + \theta) + \overline{x} \right]$ , and  $\overline{L}$  is defined in Equation (24f). The normalized time-averaged emission current density is obtained as,

$$\langle w(\bar{\varepsilon}) \rangle = \sum_{n=-\infty}^{\infty} \langle w_n(\bar{\varepsilon}) \rangle, \quad \langle w_n(\bar{\varepsilon}) \rangle = |T_n|^2 \frac{\bar{F}_0^{1/3}}{\pi \sqrt{\bar{\varepsilon}}}.$$
 (26)

## 2.3.2 Results and Discussion

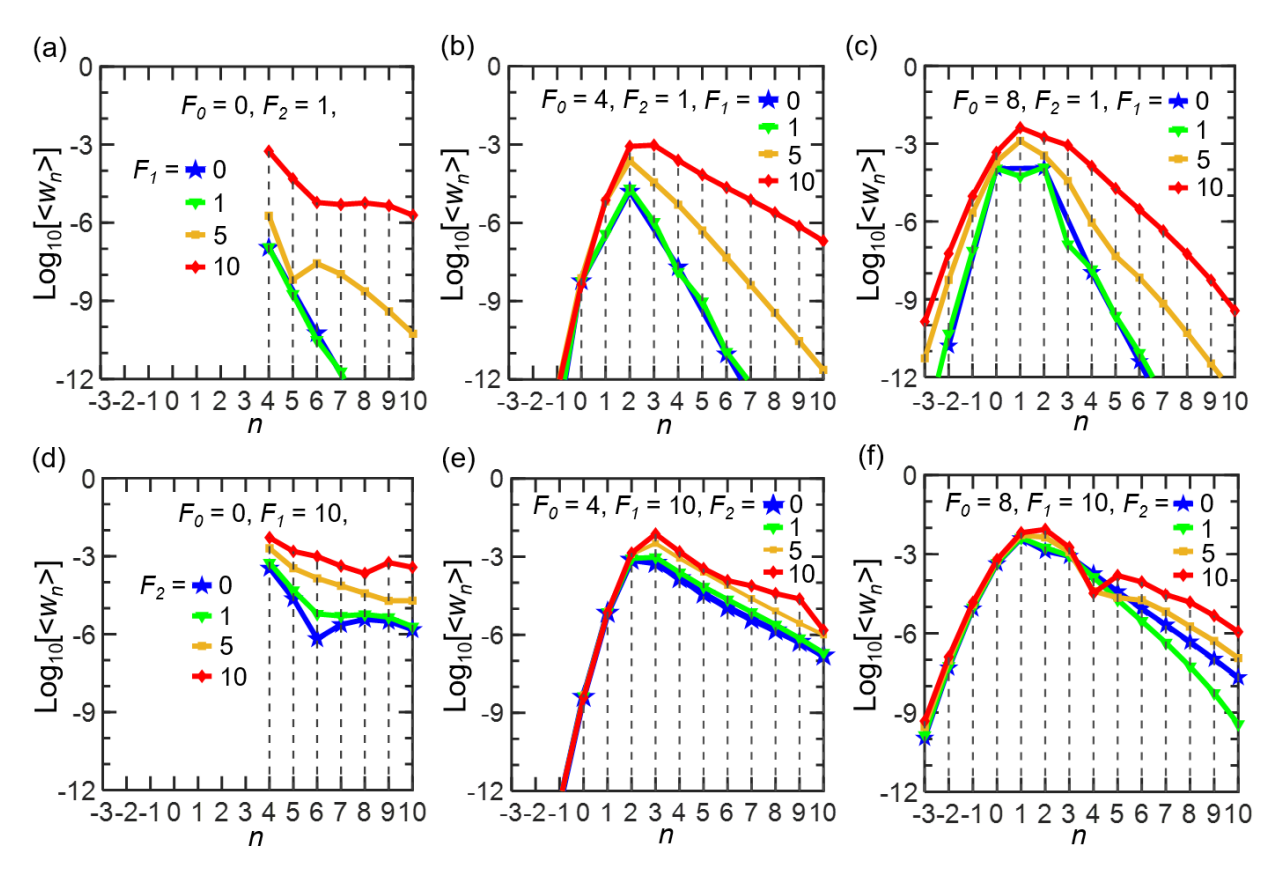


Figure 2.8: Photoelectron energy spectra under different in-phase (i.e.,  $\theta=0$ ) laser fields  $F_1$  (at frequency  $\omega$ ) and  $F_2$  (at frequency  $2\omega$ ) and dc fields  $F_0$ . In (a)-(c)  $F_2$  is fixed as 1 V/nm, and in (d)-(f)  $F_1$  is fixed as 10 V/nm. The n-photon process (that is the horizontal axis) is given with respect to the fundamental laser frequency, which measures the energy of the emitted electrons. The units of dc field  $F_0$  and laser fields  $F_1$  and  $F_2$  are V/nm in all figures.

The photoelectron energy spectra for different combinations of in-phase ( $\theta=0$ ) two-color laser fields  $F_1$  (at frequency  $\omega$ ) and  $F_2$  (at frequency  $2\omega$ ) and dc fields  $F_0$  are shown in Figure 2.8. The results are calculated from Equation (26), except for the dc field  $F_0=0$  cases (Figures 2.8(a) and 2.8(d)), which are obtained from Equation (19). When the dc field  $F_0$  is turned off (see Figures 2.8(a) and 2.8(d)), the dominant emission process is the four-photon absorption (n=4) for the fundamental laser, indicating the electron at the Fermi level needs to absorb at least four photons to overcome the potential barrier W (see Figure 2.7). This is consistent with the ratio of the work function over the fundamental laser photon energy,  $W/\hbar\omega=3.29$ . Applying a strong dc field  $F_0$ 

to the metal is able to open the tunneling emission channels below the over-barrier emission threshold (n < 4), as shown in Figures 2.8(b)-2.8(c) and 2.8(e)-2.8(f). This is because the dc field could sufficiently narrow the potential barrier at the metal-vacuum interface (x = 0) (see Figure 2.7), enabling the dc-assisted tunneling emission process for n < 4. As  $F_0$  increases from Figures 2.8(b) to 2.8(c) and 2.8(e) to 2.8(f), the potential barrier becomes narrower, increasing the probability of electron emission through the tunneling channels, and the emission channel with the highest probability shifts towards the direct tunneling process (n = 0), which is consistent with the observation in Reference [6]. For a given dc field  $F_0$ , as either of laser fields ( $F_1$  or  $F_2$ ) increases, the energy spectra become broader, because more emission channels are open up and contribute to photoemission. In the meantime, the dominant emission process shifts to the channel with larger n, which is due to the fact that electrons have to absorb sufficient number of photons to overcome the increasing ponderomotive energies  $U_{p1}=e^2F_1^2/4m_e\omega^2$  and  $U_{p2}=e^2F_2^2/4m_e\beta^2\omega^2$  with increasing laser fields strength, exhibiting the transition from the multiphoton regime to opticalstrong-field regime. These observations are consistent with previous experimentally and theoretically obtained energy spectra [6][12][14][54][61]. Since  $F_2$  is fixed at 1 V/nm in Figures 2.8(a)-2.8(c), whereas  $F_1$  is fixed at a larger value of 10 V/nm in Figures 2.8(d)-2.8(f), the spectra in Figures 2.8(d)-2.8(f) are generally broader than those in Figures 2.8(a)-2.8(c).

In general, when the dc field  $F_0$  or the laser field  $F_1$  or  $F_2$  becomes much stronger than the other two, the total current emission is dominated by this largest field. Figure 2.9 shows the normalized total time-averaged emission current density  $\langle w \rangle$  as a function of the fundamental laser field  $F_1$ , for different second harmonic laser fields  $F_2$  and dc fields  $F_0$ , when  $\theta = 0$  and  $\pi$ . When the second harmonic field  $F_2$  increases,  $\langle w \rangle$  becomes less sensitive to  $F_1$ , since  $F_2$  gradually dominates the emission process. For single-frequency laser-induced electron emission [6], it is confirmed that, in

the multiphoton regime, the slope of the curve of  $\langle w \rangle$  versus  $F_1$  follows the scale  $\langle w \rangle \propto F_1^{2n}$ ; this indicates that the dominant emission process is the n-photon process. This scale is not strictly valid for the two-color photoemission here; however, the change of the slope of the curves could still manifest the shift of the main n-photon emission process. For instance, as the dc field  $F_0$  increases from Figures 2.9(a) to 2.9(c) for  $\theta=0$  and from 2.9(d) to 2.9(f) for  $\theta=\pi$ , the slope of  $\langle w \rangle$  for a given  $F_2$  decreases, since the dominant emission process shifts to the lower emission channels.

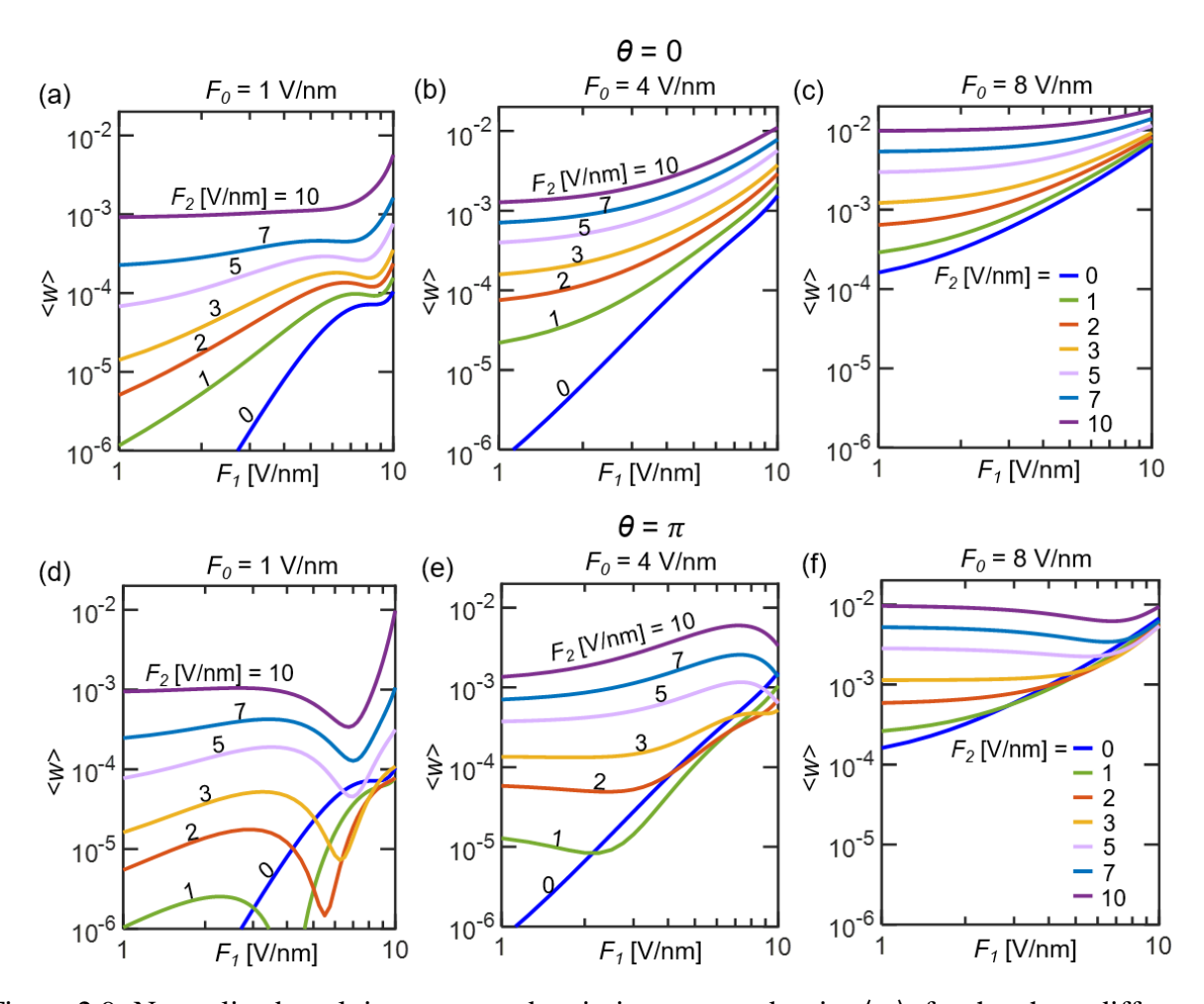


Figure 2.9: Normalized total time-averaged emission current density  $\langle w \rangle$ , for the phase difference between the two-color lasers (a)-(c)  $\theta = 0$ , and (d)-(f)  $\theta = \pi$ , as a function of the fundamental laser field  $F_1$ , under various combinations of the second-harmonic laser field  $F_2$  and dc electric field  $F_0$ . The laser intensity is related to the laser electric field as  $I_{1,2}$  (W/cm<sup>2</sup>) = 1.33 × 10<sup>11</sup>× ( $F_{1,2}$  (V/nm))<sup>2</sup>.

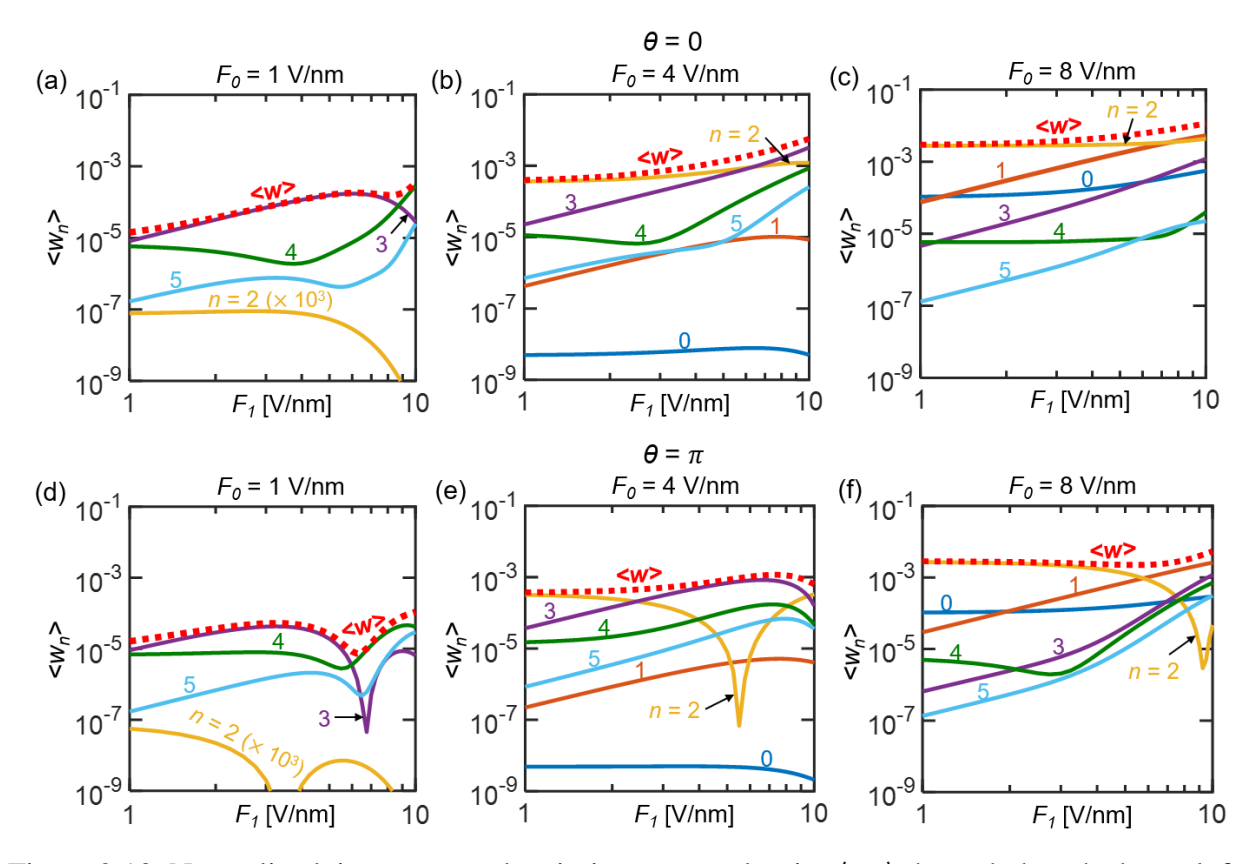


Figure 2.10: Normalized time-averaged emission current density  $\langle w_n \rangle$  through the *n*th channel, for the phase difference between the two-color lasers (a)-(c)  $\theta = 0$ , and (d)-(f)  $\theta = \pi$ , as a function of the fundamental laser field  $F_1$ , for various dc electric fields  $F_0$ , when the second harmonic laser field  $F_2 = 5$  V/nm. Dotted lines represent the normalized total emission current  $\langle w \rangle = \sum_n \langle w_n \rangle$ .

The above trend is also reflected in Figure 2.10, which shows the normalized time-averaged emission current density  $\langle w_n \rangle$  through the nth channel as a function of the fundamental laser field  $F_1$ , for fixed  $F_2 = 5$  V/nm. For both cases of  $\theta = 0$  and  $\theta = \pi$ , when  $F_0$  increases from 1 to 4 V/nm, the dominant emission channel shifts from n = 3 to n = 2 in general (see Figures 2.10(a), 2.10(b), 2.10(d), and 2.10(e)). When  $F_0$  reaches 8 V/nm, the dominant emission process transits from the two-photon absorption (n = 2) for  $F_1 \leq 7$  V/nm to single-photon absorption (n = 1) for  $F_1 > 7$  V/nm (see Figures 2.10(c) and 2.10(f)). It is clear that the direct tunneling (n = 0) is almost independent of the laser field  $F_1$  but very sensitive to the dc field  $F_0$ .

When the phase difference  $\theta$  changes from 0 to  $\pi$ , due to the interference effect between the two lasers, new dips appear in the curves of  $\langle w_n \rangle$ , which can cause changes of the dominant emission process when  $F_1$  increases. For example, in Figure 2.10(e), the dip in the curve of n=2 at around  $F_1=5.5$  V/nm changes the dominant emission to the n=3 process instead of the n=2 process otherwise observed. The dips are also reflected in the total emission current  $\langle w \rangle$  (see Figures 2.9(d) and 2.9(e)), which is consistent with our previous observation of two-color laser induced emission without a dc bias (see Figure 2.3). As the dc field  $F_0$  becomes larger, these new dips gradually disappear, as shown in Figures 2.9(f) and 2.10(f), because the interference effect of the two lasers is masked by the strong dc field.

The total emission current density  $\langle w \rangle$  as a function of the dc field  $F_0$  for different laser fields  $F_1$  and  $F_2$  is shown in Figure 2.11. When the phase difference of the two lasers  $\theta=0$ , the total emission current density  $\langle w \rangle$  increases as either of the laser fields  $(F_1 \text{ or } F_2)$  increases. When the dc field  $F_0$  becomes larger,  $\langle w \rangle$  becomes less sensitive to the laser fields, since the Fowler-Nordheim-like field emission [81] due to the dc electric field becomes more important than the over-barrier photoemission. The curves in Figure 2.11(a) resemble the experimentally measured trends of the voltage- and power-dependent electron flux (see Figure 2 in Reference [9]). As shown in Figures 2.11(d)-2.11(f), when  $\theta=\pi$ , due to the interference effect of the two lasers, the curves are intertwined, indicating strong nonlinear dependence of the emission current on the laser fields. For large  $F_0$  ( $\geq 7$  V/nm) and small  $F_2$  (= 1 V/nm) in Figure 2.11(d),  $\langle w \rangle$  remains almost the same as that with  $\theta=0$  in Figure 2.11(a), since the interference effect is suppressed by the dc field.

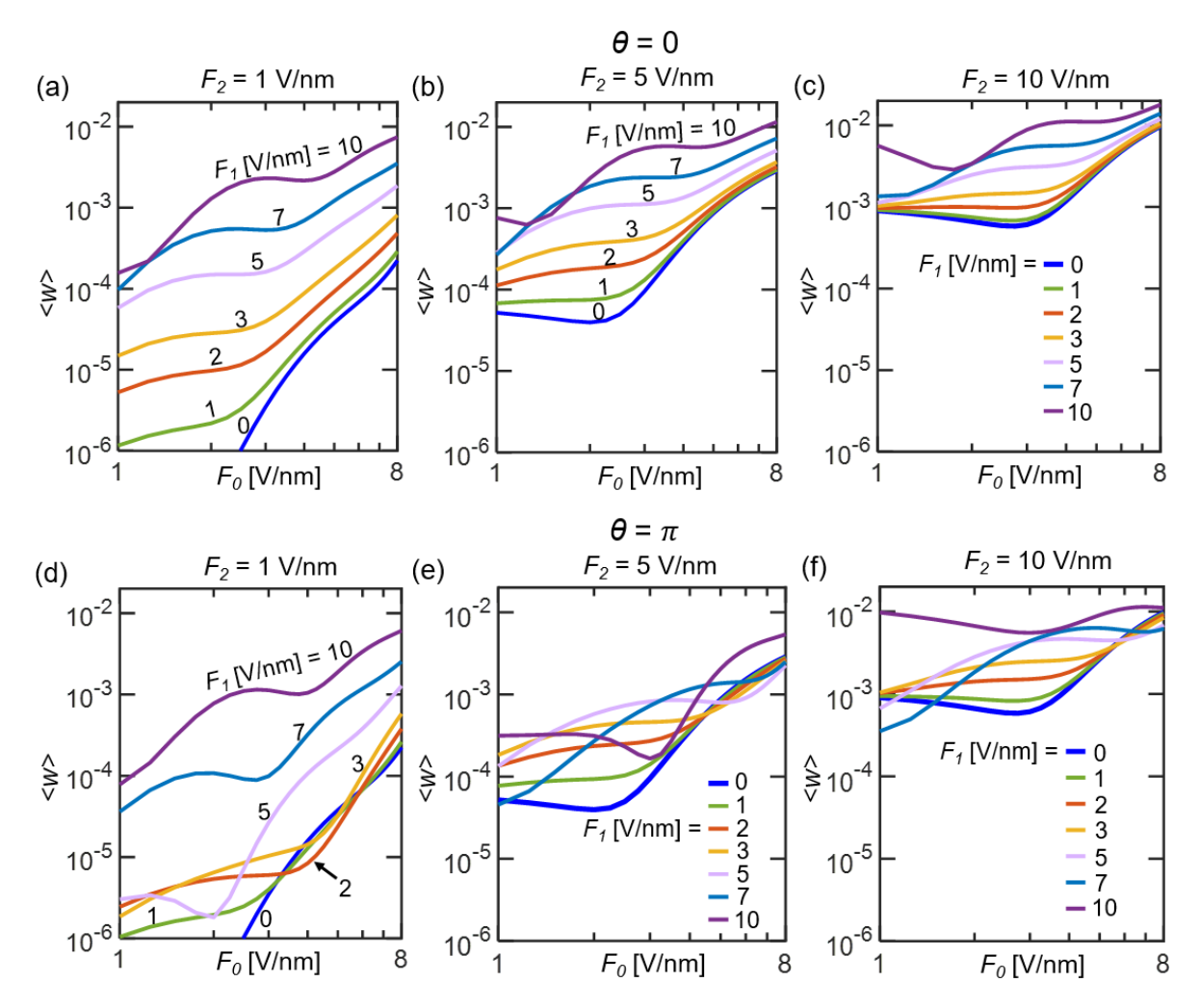


Figure 2.11: Normalized total time-averaged emission current density  $\langle w \rangle$  for the phase difference between the two-color lasers (a)-(c)  $\theta = 0$ , and (d)-(f)  $\theta = \pi$ , as a function of the dc electric field  $F_0$ , for different fundamental laser fields  $F_1$  and second-harmonic laser fields  $F_2$ . Intertwined curves in (d)-(f) indicate the strong interference effect of the two lasers.

Figure 2.12 shows the emission current density  $\langle w_n \rangle$  as a function of the dc field  $F_0$  for the case of  $F_1 = 7$  V/nm. It is clear that the dominant multiphoton emission process shifts to smaller n as  $F_0$  increases. As  $F_2$  increases, these shifts would occur at larger dc field  $F_0$ . For example, when  $\theta = 0$ , the shifts of three-photon emission to two-photon emission occur at  $F_0 \approx 3.5$ , 4, and 4.5 V/nm when  $F_2 = 1$ , 5, and 10 V/nm in Figures 2.12(a)-2.12(c), respectively. The shifts of the dominant emission process also depend strongly on the phase difference  $\theta$ . For  $F_2 = 5$  V/nm, a new dip appears in the curve of n = 2 when  $\theta = \pi$  as compared to the case of  $\theta = 0$ , leading to

the change of the dominant emission channel (i.e., two-photon process in Figure 2.12(b) vs single-photon process in Figure 2.12(e) at  $F_0 \approx 7.5 \text{ V/nm}$ ).

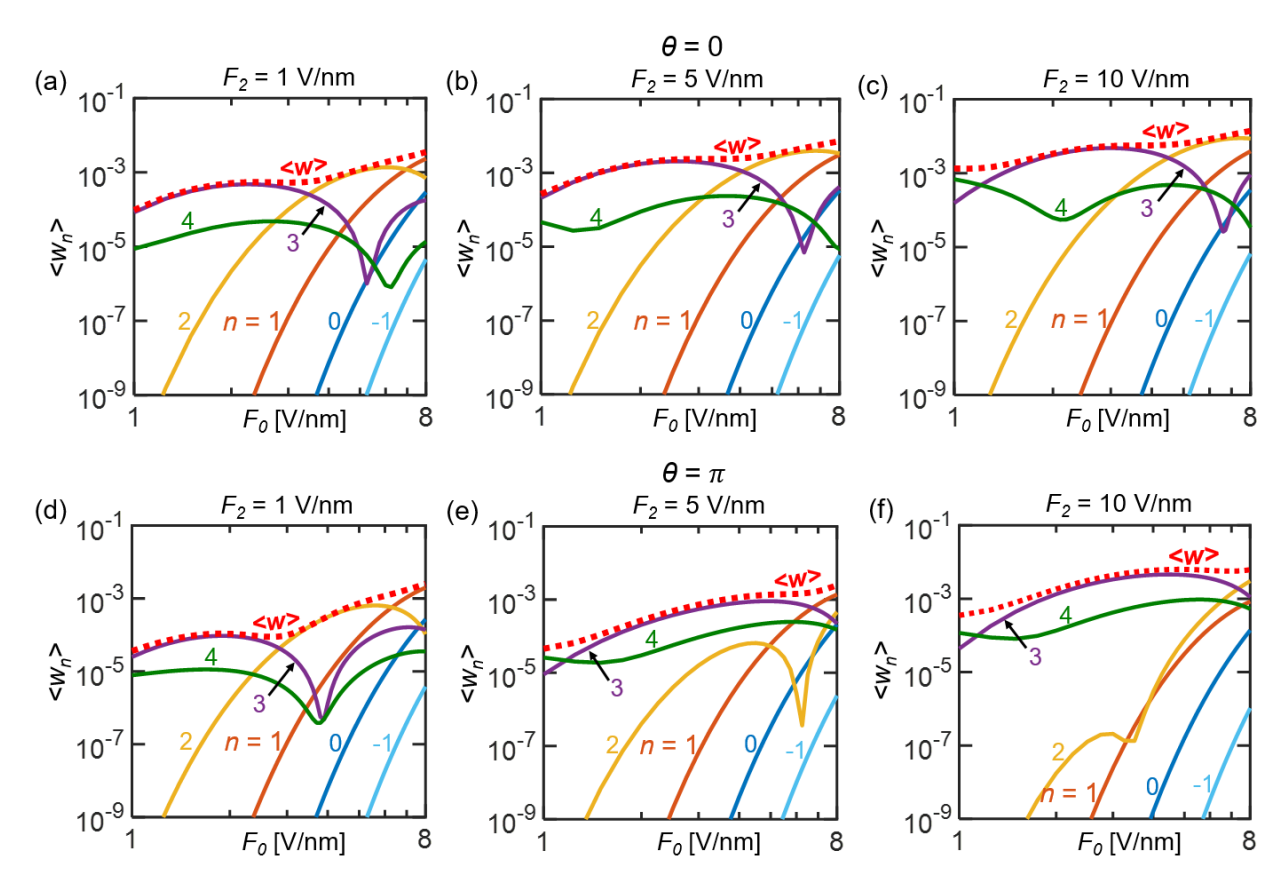


Figure 2.12: Normalized time-averaged emission current density  $\langle w_n \rangle$  through the *n*th channel for the phase difference (a)-(c)  $\theta = 0$ , and (d)-(f)  $\theta = \pi$ , as a function of the dc electric field  $F_0$ , for various second-harmonic laser fields  $F_2$ , when the fundamental laser field is  $F_1 = 7$  V/nm. Dotted lines represent the normalized total emission current  $\langle w \rangle = \sum_n \langle w_n \rangle$ .

The combined effects of the dc field and the interference between two-color lasers on the energy spectra and total emission current are shown in Figure 2.13; this reveals the strong effects of the dc bias on the photoemission current modulation depth. Figure 2.13(a) shows the effects of phase difference  $\theta$  of the two-color lasers on the total emission current density  $\langle w \rangle$ , under different dc fields  $F_0$ . Here, the  $\omega$ -laser-field  $F_1$  and the  $2\omega$ -laser-field  $F_2$  are fixed as 1.6 V/nm and 0.22 V/nm respectively (intensity ratio of 2%). It is clear that  $\langle w \rangle$  oscillates as a function of  $\theta$  with a period of  $2\pi$ , which shows a close resemblance to the experimental observation (see Figure 2(b) in

Reference [57]). As the dc field  $F_0$  increases,  $\langle w \rangle$  also increases. The maximum (minimum) values of  $\langle w \rangle$  occur around  $\theta = 0$  ( $\theta = \pi$ ), when the two-color lasers are in phase (180° out of phase). Figure 2.13(b) shows the photoelectron energy spectra of  $\langle w \rangle$  at different  $\theta$  in a single period for the case of  $F_0 = 1$  V/nm in Figure 2.13(a). When  $\theta = 0$  (A),  $\pi/2$  (B), and  $3\pi/2$  (D), the electron emission probability through the dominant channel (n = 3) driven by two-color lasers is larger than that driven by the strong fundamental laser field  $F_1$  alone. However, when  $\theta = \pi$  (C), the emission through n = 3 driven by the two-color lasers becomes smaller than that driven by  $F_1$  alone, due to the strong interference effect. The emission current driven by the two-color lasers is always larger than that driven by the weak second harmonic laser field  $F_2$  alone, regardless of  $\theta$ . These observations are in excellent agreement with the experimentally measured electron spectra (see Figure 3 in Reference [57]).

Figure 2.13(c) summarizes the modulation depth in Figure 2.13(a), defined as  $\Gamma = (\langle w \rangle_{max} - \langle w \rangle_{min})/(\langle w \rangle_{max} + \langle w \rangle_{min})$ , as a function of the dc field  $F_0$ . When  $F_0$  is zero, the modulation depth  $\Gamma$  is as high as 99% [61]. As  $F_0$  increases,  $\Gamma$  decreases because the interference effect is gradually suppressed by  $F_0$ . When  $F_0 = 8$  V/nm,  $\Gamma$  drops to approximately 2.98%, showing a strong dependence of current modulation on the dc bias. It is important to note that even when the dc bias  $F_0$  reaches 3 V/nm (significantly larger than the laser fields  $F_1 = 1.6$  V/nm and  $F_2 = 0.22$  V/nm, corresponding to a ratio of  $F_0$ :  $F_1$ :  $F_2 \cong 1$ : 0.5: 0.07), a current modulation  $\Gamma \geq 70\%$  can still be achieved. This suggests a practical way to maintain a strong current modulation, while increasing the total emission current by orders of magnitude, by simply adding a strong dc bias for two-color laser induced electron emission.

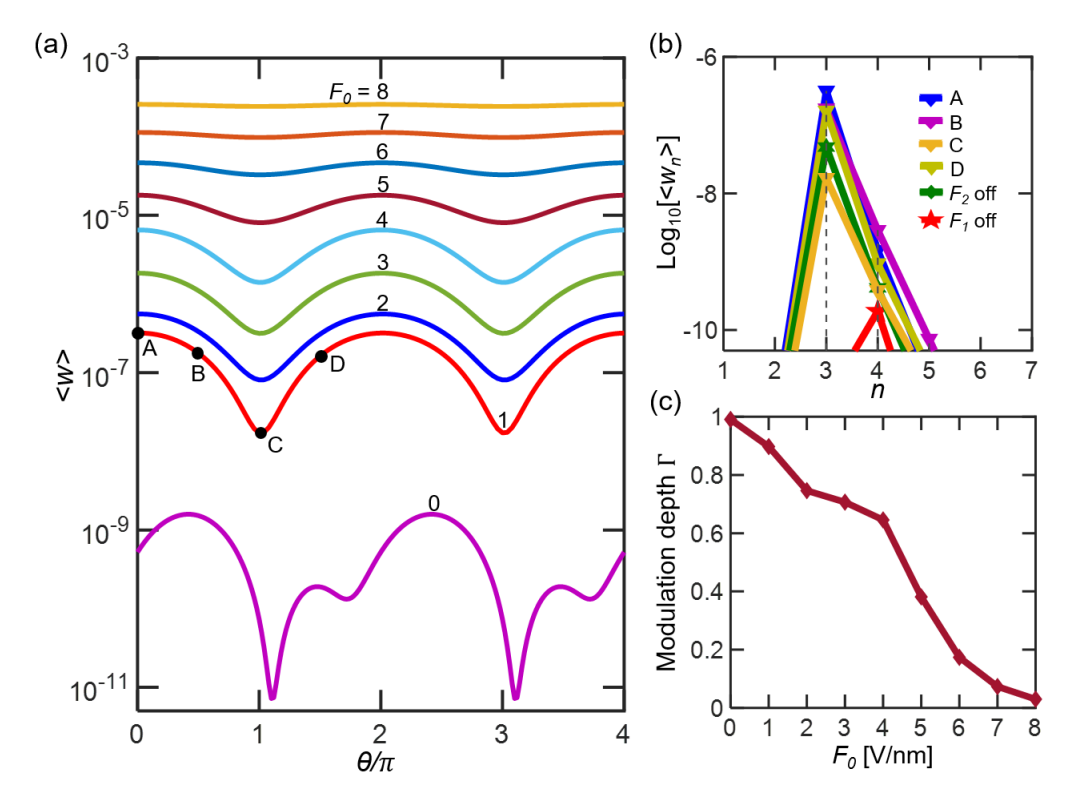


Figure 2.13: Emission current modulation depth. (a) Normalized total time-averaged emission current density  $\langle w \rangle$  as a function of the phase difference  $\theta$ , for different dc electric fields  $F_0$ , with  $\omega$ -laser-field  $F_1$  and  $2\omega$ -laser-field  $F_2$  fixed at 1.6 V/nm and 0.22 V/nm respectively (experimental laser parameters in Reference [57]). (b) Energy spectra of the emission current at different  $\theta$  for the case of  $F_0 = 1$  V/nm in (a). A, B, C, and D denote the cases of  $\theta = 0$ ,  $\pi/2$ ,  $\pi$ , and  $3\pi/2$  in (a), respectively. (c) Current modulation depth  $\Gamma$  in (a) as a function of the dc field  $F_0$ . The unit of dc field  $F_0$  is V/nm in all figures.

Since photoelectron emission paths (or channels) depend strongly on the incident laser frequencies, as well as the interferences between them, superimposing different order of harmonic lasers on the fundamental laser can lead to different photoemission currents. Figure 2.14 shows the effects of the harmonic order  $\beta$  on the total emission current density  $\langle w \rangle$  induced by the two-color lasers of frequency  $\omega$  and  $\beta\omega$  under various dc fields. When the dc field  $F_0=0$ , the maximum value of  $\langle w \rangle$  occurs when  $\beta=4$ . This is because the maximum emission current happens when the single-photon energy (of the fourth-harmonic laser in this case) roughly equals the potential barrier  $(4\hbar\omega/W\approx1)$  [6][61]. By comparing Figure 2.14 with Figure 2.8, it is found that the harmonic order  $\beta$  where the maximum emission current occurs coincides with the channel

number n of the dominant n-photon process (with respect to the fundamental frequency  $\omega$ ), for a given combination of  $F_0$ ,  $F_1$ , and  $F_2$ . As observed in Figure 2.14, as  $F_0$  increases, the value of  $\beta$  for the maximum  $\langle w \rangle$  shifts to a smaller number. This is consistent with the observation in Figure 2.8 that a larger dc field  $F_0$  changes the dominant n-photon process to a smaller n. When  $F_0 \geq 7$  V/nm, the electron emission becomes almost independent of the frequency  $(\beta \omega)$  of harmonic laser, since the Fowler-Nordheim-like field emission dominates the emission process. When  $\theta$  changes from 0 to  $\pi$ , for small  $F_0$  ( $\leq 4$  V/nm) and  $\beta$  ( $\leq 4$ ), the emission current density  $\langle w \rangle$  has a distinct reduction due to the interference effect of the two lasers. However, for large  $F_0$  ( $\geq 7$  V/nm), the emission current  $\langle w \rangle$  is almost independent of  $\theta$ , for all harmonic orders of the second laser.

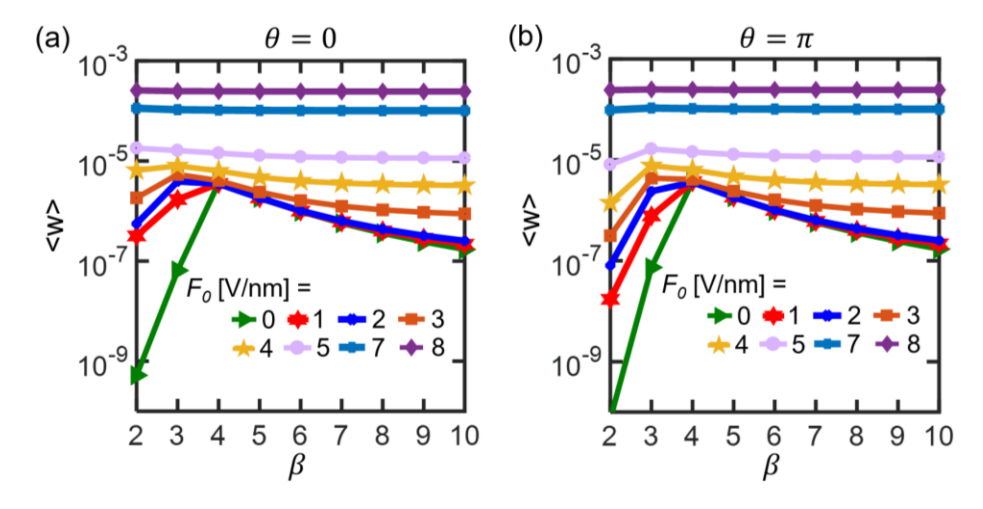


Figure 2.14: Normalized total time-averaged emission current density  $\langle w \rangle$  as a function of harmonic order  $\beta$ , for the phase difference (a)  $\theta = 0$ , and (b)  $\theta = \pi$ . The fundamental  $\omega$ -laser field  $F_1 = 1.6$  V/nm, and the harmonic  $\beta \omega$ -laser field  $F_2 = 0.22$  V/nm.

Our calculations so far are based on the sharp triangular potential profile (see Figure 2.7), which does not include the image charge effects (or Schottky effect) due to the applied dc field. Our earlier work [6] demonstrated that the effects of image-charge-induced Schottky barrier lowering on photoemission can be accurately approximated in our model, by simply replacing the work function W in Equation (20) with the effective work function  $W_{eff} = W - 2\sqrt{e^3 F_0/16\pi\varepsilon_0}$ ,

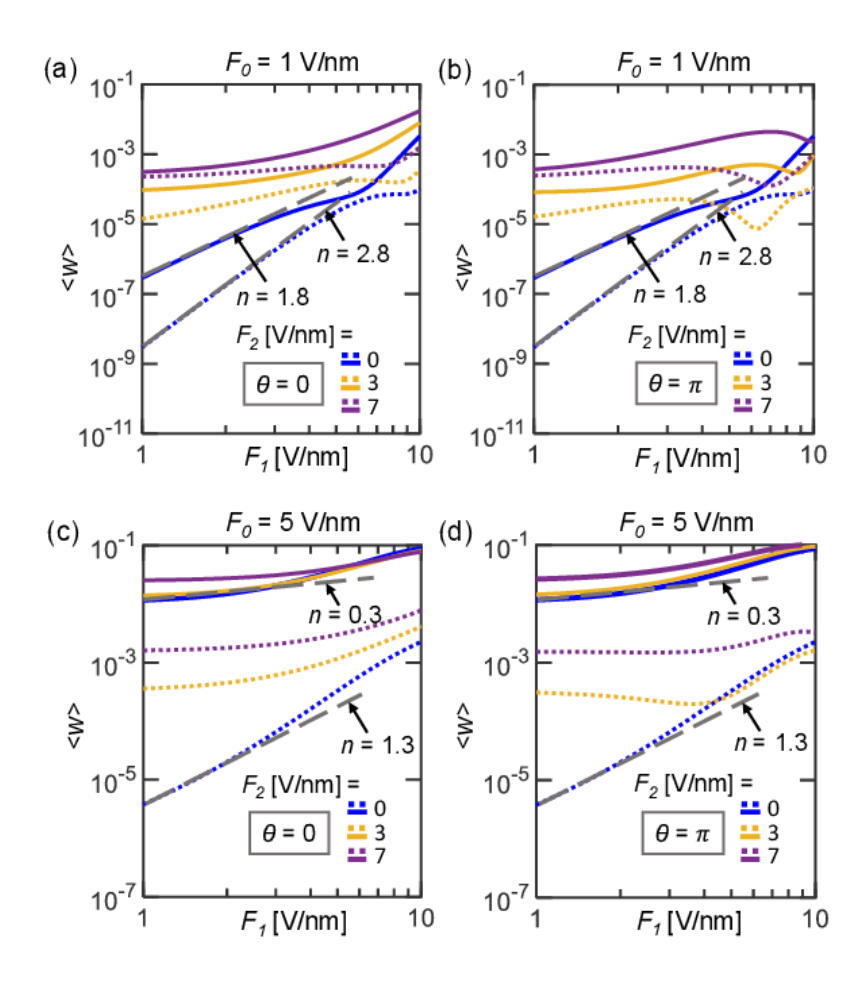


Figure 2.15: Effects of the image-charge-induced barrier lowering on the total emission current  $\langle w \rangle$  for various  $F_0$ ,  $F_1$ ,  $F_2$ , and  $\theta$ . The solid (dotted) lines represent the cases with (without) the image charge effect, calculated using effective work function  $W_{eff}$  (work function W). The gray dashed lines show the scale  $\langle w \rangle \propto F_1^{2n}$ .

where  $\epsilon_o$  is the free space permittivity. A comparison between the total emission current density  $\langle w \rangle$  with and without the image-charge-induced barrier lowering is shown in Figure 2.15. Due to the reduction of potential barrier ( $W_{eff} < W$ ), the emission current increases when considering the image charge effect. A larger dc field  $F_0$  increases the emission current more significantly ( $F_0 = 1 \text{V/nm}$  in Figures 2.15(a), 2.15(b) vs  $F_0 = 5 \text{V/nm}$  in 2.15(c), 2.15(d)), since a smaller effective barrier  $W_{eff}$  is created. As  $F_2$  increases, the difference between the emission current  $\langle w \rangle$  with  $W_{eff}$  and with W becomes smaller. The increase of the emission current due to the inclusion of the image effect is relative insensitive to the phase delay  $\theta$  of the two-color lasers. It is also

important to note that with the inclusion of  $W_{eff}$ , the slope of  $\langle w \rangle$  decreases, as observed from the value of n in the scale  $\langle w \rangle \propto F_1^{2n}$ , which indicates that the number of photons involved in the dominant emission process decreases, because of the deduction of the potential barrier near the metal surface.

# 2.3.3 Application to Time-Resolved Photoelectron Spectroscopy

Photoelectron spectroscopy is one of the most popular techniques to study the composition and electronic states of solid surfaces by analyzing the energy spectra [89], [90]. Particularly, the time-resolved photoemission spectroscopy enables the measurement of short lifetime of the intermediate states, such as the image-potential states on metal surface, via control of the time delay between the pump and probe photons [91]–[93]. In this part, we demonstrate the application of our analytical model to describe the dynamics of different *n*-photon excited states in time and energy.

As shown in Figure 2.16(a), our 1D model is able to provide excellent fitting to the measured photoelectron spectra in Reference [57] for the tungsten nanotip, by using a dc field of  $F_0 = 0.01$  V/nm and an effective work function of  $W_{eff} = 3.85$  eV. Furthermore, the current modulation profile (both magnitude and shape) obtained from our 1D model in section 2.2 [61] agrees very well with the experimentally observed sinusoidal variation with a period of  $2\pi$  for the relative phase delay  $\theta$ , as shown in Figure 2.16(b). Notably, other models, including simple tunneling rate model and 1D time-dependent density functional theory (TDDFT), fail to describe the experimental results of the sinusoidal profile (see supplementary material of Reference [57]).

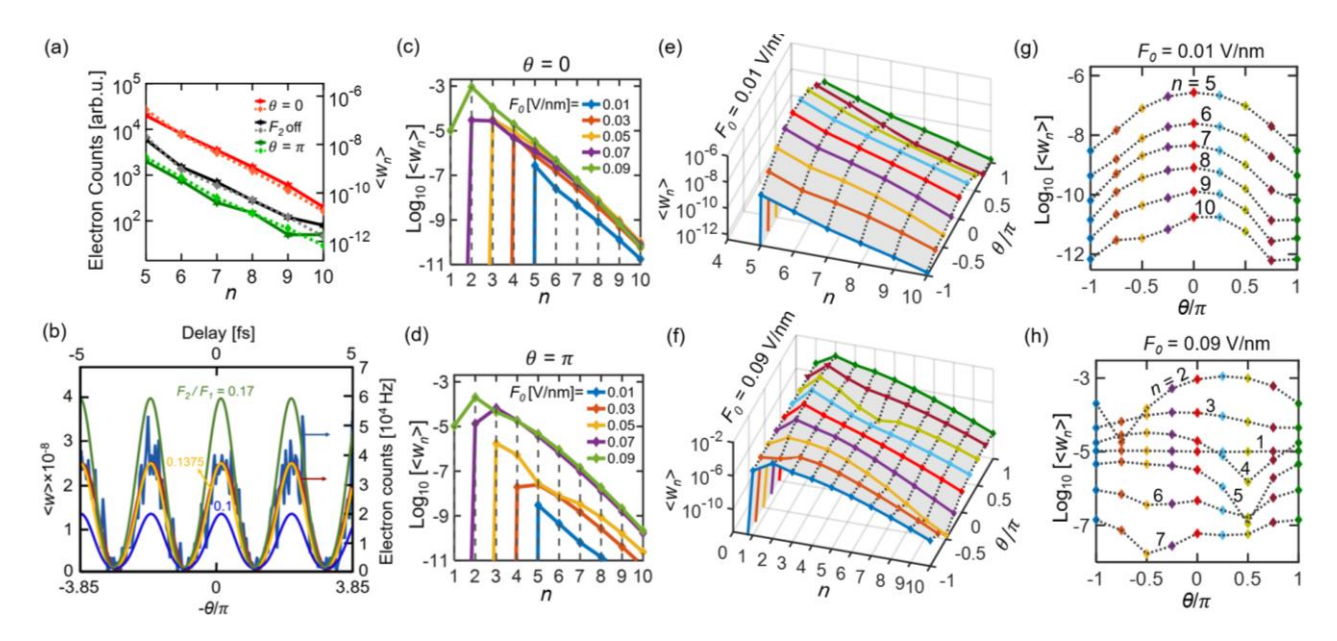


Figure 2.16: Time-resolved photoelectron energy spectra for the tungsten nanotip. (a) Comparison between the experimentally measured electron counts from Figure 3 in Reference [57] (see solid lines) and fitting results  $\langle w_n \rangle$  (see dotted lines). (b) Normalized total time-averaged emission current density  $\langle w \rangle$  as a function of the phase difference between the two-color lasers  $\theta$ , for different  $F_2/F_1$ , with fixed  $F_1=1.6$  V/nm. Blue and red lines denote the experimentally observed emission electron current and the sine fit from Figure 2(b) of Reference [57], respectively. (c),(d) Energy spectra for various dc fields  $F_0$  when (c)  $\theta=0$ , and (d)  $\theta=\pi$ . (e),(f) Photoelectron spectra at different phase delays  $\theta$  for the dc field (e)  $F_0=0.01$  V/nm and (f)  $F_0=0.09$  V/nm. (g),(h) Projection of the spectra in (e) and (f) on the  $\theta$  plane, respectively. Except (b), the fundamental laser (1560 nm) field  $F_1=1.8$  V/nm and the second-harmonic laser field  $F_2=0.3$  V/nm for all other figures (experimental laser parameters in Reference [57]).

The photoelectron energy spectra from the tungsten nanotip under various dc fields are shown in Figures 2.16(c) and 2.16(d), for  $\theta=0$  and  $\theta=\pi$ , respectively. In the calculation, for each dc field, the effective work function  $W_{eff}$  is approximated by determining the peak value in the surface barrier profile under dc bias [94][95],  $\Phi_{dc}(x)=W-eF_0d\ln(\frac{2x+r}{r})/\ln(\frac{2d}{r}+1)-C_s^2r/2e(x^2-r^2)$ , where the second term is the axial potential profile near a parabolic tip of radius of curvature r with d being a constant (= 83 nm to fit the spectra in Figure 2.16(a)) [95], and the third term is the image charge potential of a spherical surface, with  $C_s=\sqrt{e^3/4\pi\epsilon_0}=1.199985 \text{ eV}(\text{V/nm})^{-1/2}$  being the Schottky constant [94]. It is important to note that the

photoelectron spectra are very sensitive to the applied dc field  $F_0$ , as shown in Figures 2.16(c) and 2.16(d). The shift of the dominant emission process to a smaller n with larger dc field  $F_0$  agrees with the trend in Figure 2.8. More importantly, the emission current density is increased by more than three orders of magnitude as  $F_0$  is gradually increased from 0.01 to 0.09 V/nm, which could strongly facilitate the experimental detection of photoemission.

When the relative time delay  $\theta$  changes from  $-\pi$  to  $\pi$ , the variations of the spectra during one period for  $F_0 = 0.01$  and 0.09 V/nm are shown in Figures 2.16(e) and 2.16(f), respectively. To clearly observe the dynamics of different excited states in time, Figures 2.16(g) and 2.16(h) show the projection of the energy spectra in Figures 2.16(e) and 2.16(f) on the  $\theta - \langle w_n \rangle$  plane respectively. When the dc field is small, with  $F_0 = 0.01 \text{ V/nm}$  (see Figure 2.16(g)), all the *n*-photo orders of the spectra are modulated in the same way as a function of the relative phase delay  $\theta$ , in agreement with the results in Reference [57]. The rising tendency of the points along the phase difference  $\theta$  from  $-\pi$  to 0 indicates the population of the *n*-photon excited intermediate states induced by lasers, while the decreasing signal from 0 to  $\pi$  implies the decay of the excited states. When  $F_0$  is increased to 0.09 V/nm (see Figure 2.16(h)), it is interesting to find that due to the effect of the dc field, various n-photon excited states behave differently with respect to time delay  $\theta$ . For instance, the one-photon tunneling state is almost invariable as  $\theta$  changes from  $-\pi$  to  $\pi$ , but the two-photon state decreases significantly at  $\theta = -3\pi/4$ . This is in contrast to the two samefrequency induced photoemission, where the dynamics of multiphoton excited states remains same under different dc bias  $F_0$  (see Figure 3.1). In addition, for a small dc field, the value of n for the dominant excitation state remains unchanged over the relative phase delay  $\theta$  (see Figure 2.16(g)), which means the energy of the *n*-photon excited intermediate state is independent of the time delay

[91]. However, when the dc field is larger, n for the dominant excitation state changes with the relative phase delay  $\theta$  (see Figure 2.16(h)).

For electron emitters under a dc bias, it is important to prevent breakdown and premature failure of the emitter tips. Table I lists the local dc fields (after field enhancement) of sharp tips that have already been achieved in experiments before breakdown for eight materials. It is known that nanostructures survive large fields better for short pulse durations. Thus, local dc field up to 10 V/nm or larger value at sharp tips may be realized in experiments via either laboratory-scale setup based on pulsed capacitor discharge [9][96], or powerful THz pulses [97]..

Table 1: List of achieved strong local dc fields (after field enhancement) of sharp tips before breakdown for eight materials.

<u> </u>	Achieved local dc field
	(V/nm)
Au	8.8 [9]
W	9.64 [96]
Cu	10.35 [96]
Mo	8.09 [96]
Pt/Ir	16 [97]
Carbon fiber	10.46 [41]
Carbon nanotube	14 [98]
CNT fiber	9.85 [42]–[44]

# 2.3.4 Summary on Photoemission with DC Bias

In this section, we construct an exact analytical model for photoelectron emission from a dc biased metal surface induced by two-color laser fields, by solving the time-dependent Schrödinger equation. Our calculations reveal underlying various emission process, including multiphoton over-barrier emission, dc-assisted tunneling emission and optical field emission, for different dc

and laser fields, and recover the trend in the experimentally measured energy spectra and voltageand power-dependent electron flux. Besides the properties of the two-color lasers, including
relative phase, intensity and frequency, our model shows the addition of a dc field to the metal
surface can provide great tunability of the photoemission energy spectra and current modulation
depth for two-color laser-induced photoemission. Furthermore, the dc bias can increase the
emission current by orders of magnitude. This increase of the current emission is due to the
combined effects of potential barrier narrowing and barrier lowering. Our results suggest a
practical way to maintain a strong current modulation while increasing the total emission current
by orders of magnitude in two-color laser induced electron emission, by simply adding a strong dc
bias and a weak harmonic laser. This work will enable applications requiring both high current
level and strong current modulation, such as miniaturized particle accelerators, photoelectron
microscopy, and ultrafast electron sources. Moreover, being verified against the experimentally
measured time-resolved photoelectron energy spectra, the results from our model are expected to
guide future experiments on time-resolved photoemission spectroscopy.

### 2.5 Conclusion

In this chapter, we present quantum analytical solutions for highly nonlinear ultrafast photoelectron emission from metal surfaces driven by two-color laser fields with and without a dc bias, by exactly solving the TDSE. We systematically study the photoelectron energy spectra, emission current density, and current modulation under various combinations of laser intensities and frequencies, dc bias, and phase differences of the two-color lasers. Our model shows great tunability on the photoelectron spectra, emission current, and current modulation depth, via the control of the phase delay, relative intensity, harmonic order of the two-color lasers and dc fields. The results are in good agreement with experimental measurements on the two-color photoelectron

energy spectra and current modulation from a sharp nanotip. Our results suggest a practical way to maintain a strong current modulation in the meantime to increase the total photoemission current by orders of magnitude, by simply adding a strong dc bias and a weak harmonic laser. Application of our model to time-resolved photoelectron spectroscopy is also exemplified, showing the dynamics of the *n*-photon two-color excited electronic states depends strongly on the applied dc field. Our study may inspire new routes towards many applications requiring both high photoemission current and strong current modulation, such as tabletop particle accelerator, X-ray sources and time-resolved photoelectron microscopy.

#### **CHAPTER 3**

# PHOTOEMISSION MODULATION BY TWO LASERS OF THE SAME-FREQUENCY

#### 3.1 Introduction

Although two-color laser induced electron emission from nanoemitters provides an attractive platform for modulating photoelectron emission by the relative phase difference between the two-color lasers and shows promises for the potential application of time-resolved photoelectron spectroscopy [62][99], the two-color laser system typically relies on the generation of higher order harmonics of a fundamental laser [57]–[60][85], which, because of its stringent requirements on the experimental setup and its relative low efficiency, greatly limits the accessibility of the two-color laser system. For higher intensity lasers, harmonic generation becomes increasingly complex and difficult to control [100][101].

In this Chapter, we propose to utilize two lasers of the same frequency to modulate the photoelectron emission by their relative phase delay. This is motivated by the simple experimental implementation of single-frequency laser pairs, e.g. via a beam splitter with various coating materials to control the reflection and transmission of incident light [102]–[105]. The two same-frequency lasers may be tuned to have virtually arbitrary ratio of intensities (in contrast to a small harmonic-to-fundamental intensity ratio in the two-color laser system [57]–[60][85]), thus providing a much larger parameter space to assess the interference effect of the two lasers and the induced photoelectron emission. Using the quantum mechanical model in Reference [6], we study the photoemission modulation properties for a dc-biased metal cathode illuminated by two laser fields with the same frequency. We investigate the modulation of photoemission current and the dynamics of multiphoton excited states for different laser fields, wavelengths, cathode materials, and dc fields. Our study demonstrates the capability of measuring the time-resolved photoelectron

energy spectra using single-frequency laser pairs. The material of this chapter is based on our published paper in Reference [106] and is presented with permission from the copyright holder.

# 3.2 Analytical model

Under the action of two same-frequency laser fields  $F_1\cos(\omega t)$  and  $F_2\cos(\omega t + \theta)$  and a dc electric field  $F_0$ , the time-dependent potential barrier near the surface of the cathode reads [6][61][62][74][106],

$$\Phi(x,t) = \begin{cases} 0, & x < 0 \\ E_F + W_{eff} - eF_0 x - eFx \cos(\omega t + \varphi), & x \ge 0, \end{cases}$$
 (27)

where  $E_F$  is the Fermi energy of the metal cathode,  $W_{eff} = W - 2\sqrt{e^3F_0/16\pi\varepsilon_0}$  is the effective work function with Schottky effect [6], with W being the nominal work function, e is the elementary charge,  $\varepsilon_0$  is the free space permittivity, x is the distance away from the cathode surface (x=0), and F is the magnitude of the total laser field due to the two laser fields  $F_1\cos(\omega t)$  and  $F_2\cos(\omega t + \theta)$ ,

$$F = \sqrt{(F_1 + F_2 \cos \theta)^2 + (F_2 \sin \theta)^2}.$$
 (28)

From Equation (28), it is clear that the magnitude of the total laser field depends strongly on the phase delay of the two lasers  $\theta$ , which is expected to provide similar current modulation to that in the two-color laser setup [61][62]. The resultant phase  $\varphi = \arcsin(F_2 \sin \theta / F)$ , the effect of which becomes important for photoemission only in very short laser pulses when carrier-envelope phase matters. For laser pulses longer than about 10 cycles, it can be well approximated by continuous-wave excitation for photoemission [6]. Thus, in the calculation of this chapter, we ignore the effects of the absolute phase and set  $\varphi = 0$  without loss of generality [106]. Based on the quantum analytical theory of photoemission in References [6][74], the time-averaged normalized emission current density, defined as the time-averaged ratio of the transmitted

probability current density over the incident probability current density,  $\langle w(\varepsilon, x, t) \rangle = \langle J_t/J_i \rangle$ , can be obtained as,

$$\langle w(\varepsilon) \rangle = \sum_{n=-\infty}^{\infty} \langle w_n(\varepsilon) \rangle, \quad \langle w_n(\varepsilon) \rangle = \frac{(eF_0\hbar/\sqrt{2m_e})^{1/3}}{\pi\sqrt{\varepsilon}} |T_n|^2, \tag{29}$$

where  $\langle w_n \rangle$  denotes the normalized emission current density through the nth channel with emitted electron energy  $\varepsilon + n\hbar\omega$  due to the n-photon contribution,  $\hbar$  is the reduced Plank constant, m is the electron mass and  $T_n$  represents the transmission coefficient of electron wave functions, which is calculated from,

$$2\sqrt{\varepsilon}\delta(l) = \sum_{n=-\infty}^{\infty} T_n \left[ \sqrt{\varepsilon + l\hbar\omega} P_{n(n-l)} + \frac{\hbar}{\sqrt{2m_e}} Q_{n(n-l)} \right], \tag{30}$$

where  $\delta(l)$  is the Dirac delta function, l and n are integers,  $P_{nl} = \frac{1}{2\pi} \int_0^{2\pi} p_n(\omega t) e^{-il\omega t} d(\omega t)$  and  $Q_{nl} = \frac{1}{2\pi} \int_0^{2\pi} q_n(\omega t) e^{-il\omega t} d(\omega t)$  are the Fourier coefficients, with  $p_n(\omega t) = \exp\left[-(ie^2 F_0 F/m_e \hbar \omega^3) \sin \omega t + (ie^2 F^2/8m_e \hbar \omega^3) \sin 2\omega t\right] r(\alpha_n)$  and  $q_n(\omega t) = \exp\left[-(ie^2 F_0 F/m_e \hbar \omega^3) \sin \omega t + (ie^2 F^2/8m_e \hbar \omega^3) \sin 2\omega t\right] [(eF/\hbar \omega) r(\alpha_n) \sin \omega t + (2mF_0 e/\hbar^2)^{1/3} s(\alpha_n)]$ , where  $r(\alpha_n) = Ai(\alpha_n) - iBi(\alpha_n)$ ,  $s(\alpha_n) = iAi'(\alpha_n) + Bi'(\alpha_n)$ , and  $\alpha_n = -[E_n/eF_0 + (eF/m_e \omega^2) \cos \omega t] (2em_e F_0/\hbar^2)^{1/3}$  with  $E_n = \varepsilon + n\hbar\omega - E_F - W_{eff} - U_p$ . Here, Ai and Bi are the Airy functions of the first kind and second kind respectively,  $U_p = e^2 F^2/4m_e \omega^2$  is the ponderomotive energy, and a prime denotes derivative with respect to the argument. For the special case of zero dc field  $F_0 = 0$ , the time-averaged normalized emission current density becomes [6][74],

$$\langle w(\varepsilon) \rangle = \sum_{n=-\infty}^{\infty} \langle w_n(\varepsilon) \rangle, \quad \langle w_n(\varepsilon) \rangle = \text{Re}(|T_n|^2 \sqrt{E_n/\varepsilon}),$$
 (31)

where  $T_n$  is still calculated from Equation (30) with  $P_{nl}$  and  $Q_{nl}$  unchanged, but with  $p_n(\omega t) = \exp\left[(ie^2F^2/8m_e\hbar\omega^3)\sin 2\omega t + (ieF\sqrt{2m_eE_n}/m_e\hbar\omega^2)\cos \omega t\right]$  and  $q_n(\omega t) = p_n(\omega t)\left[\sqrt{2m_eE_n}/\hbar + eF\sin \omega t/\hbar\omega\right]$ .

# 3.3 Results and Discussion

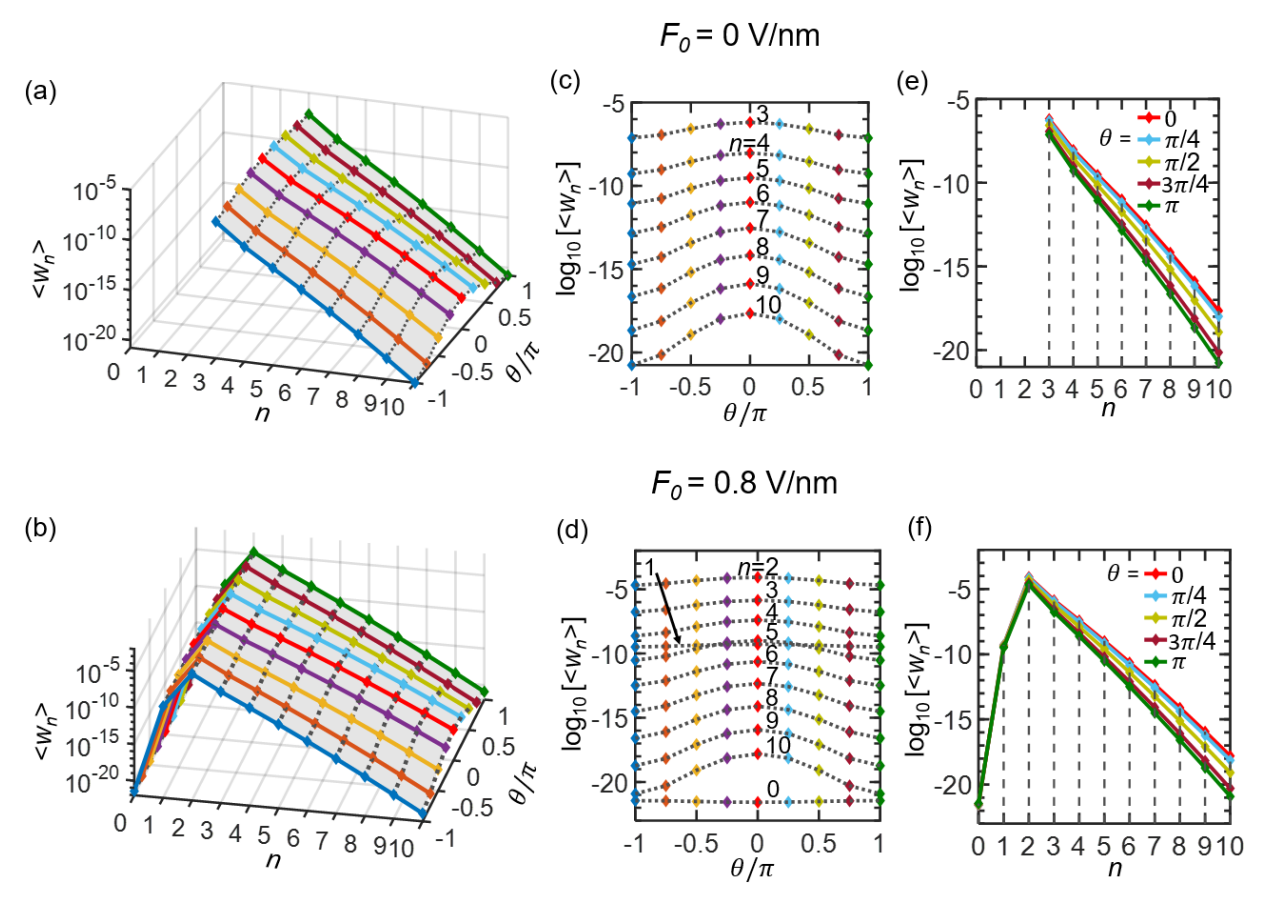


Figure 3.1: Time-resolved photoelectron energy spectra. (a),(b) Energy spectra as a function of the phase difference between the two lasers  $\theta$ , for dc field (a)  $F_0 = 0$  and (b)  $F_0 = 0.8$  V/nm. (c),(d) Projections of the spectra in (a),(b) on the  $\theta$ - $\langle w_n \rangle$  plane respectively. (e),(f) Projections of the spectra in (a),(b) on the n- $\langle w_n \rangle$  plane respectively. Here, the laser fields  $F_1 = 1.8$  V/nm and  $F_2 = 0.3$  V/nm (experimental parameters in Reference [57]).

In Figure 3.1, we plot the calculated photoelectron energy spectra as a function of the phase difference between the two lasers  $\theta$  for different dc fields  $F_0$ . The wavelength of both lasers is 800 nm ( $\hbar\omega=1.55$  eV). The metal is assumed to be tungsten [7][13][57], with a Fermi energy  $E_F=7$  eV and a work function W=4.31 eV. Since most of the electrons emitted from sources are

located near the Fermi level [6][76][86][87], we choose the electron initial energy  $\varepsilon = E_F$  for simplicity. Note with laser fields  $F_1 = 1.8$  V/nm and  $F_2 = 0.3$  V/nm for the special case of  $\theta = 0$ , the total normalized emission current density in Figure 3.1 is  $\langle w \rangle = 6.67 \times 10^{-7}$  and  $8.71 \times 10^{-5}$ , for the DC field  $F_0 = 0$  and 0.8 V/nm respectively. Using free-electron theory of metal [74], we find the corresponding emission current density is  $5.74 \times 10^2$  A/cm<sup>2</sup> and  $6.75 \times 10^4$  A/cm<sup>2</sup>, respectively.

When the dc field  $F_0$  is turned off, the dominant emission process is three-photon absorption (n= 3) (see Figures 3.1(a) and 3.1(e)). This is consistent with the ratio of the work function of tungsten over the photon energy,  $W/\hbar\omega \approx 2.8$ . By changing the phase difference  $\theta$  between the two lasers, the electron emission varies sinusoidally (see Figures 3.1(a) and 3.1(c)). When applying a large dc field  $F_0$  to the cathode, the tunneling emission channels ( $n \le 2$ ) are opened up, as shown in Figures 3.1(b) and 3.1(f). This is because the dc field adequately narrows the surface potential barrier, in addition to the Schottky-effect-induced barrier lowering, enabling the tunneling emission process. In the case of  $F_0 = 0.8 \text{ V/nm}$ , the dominant emission process is shifted to twophoton absorption. From Figures 3.1(c) and 3.1(d), it is found that the multiphoton excited states  $(n \ge 3)$  vary with respect to the phase delay  $\theta$  sinusoidally in the same way, with the maximum at  $\theta = 0$  and the minimum at  $\theta = \pm \pi$ , for both values of dc bias  $F_0$ . This is in contrast to the twocolor laser induced photoemission, where the dynamics of multiphoton excited states changes under different dc bias  $F_0$  (see Figure 2.16(g) and 2.16(h)). The one-photon (n = 1) absorption and direct tunneling (n=0) process are almost independent of  $\theta$  for the case of  $F_0=0.8$  V/nm, as shown in Figures 3.1(d) and 3.1(f).

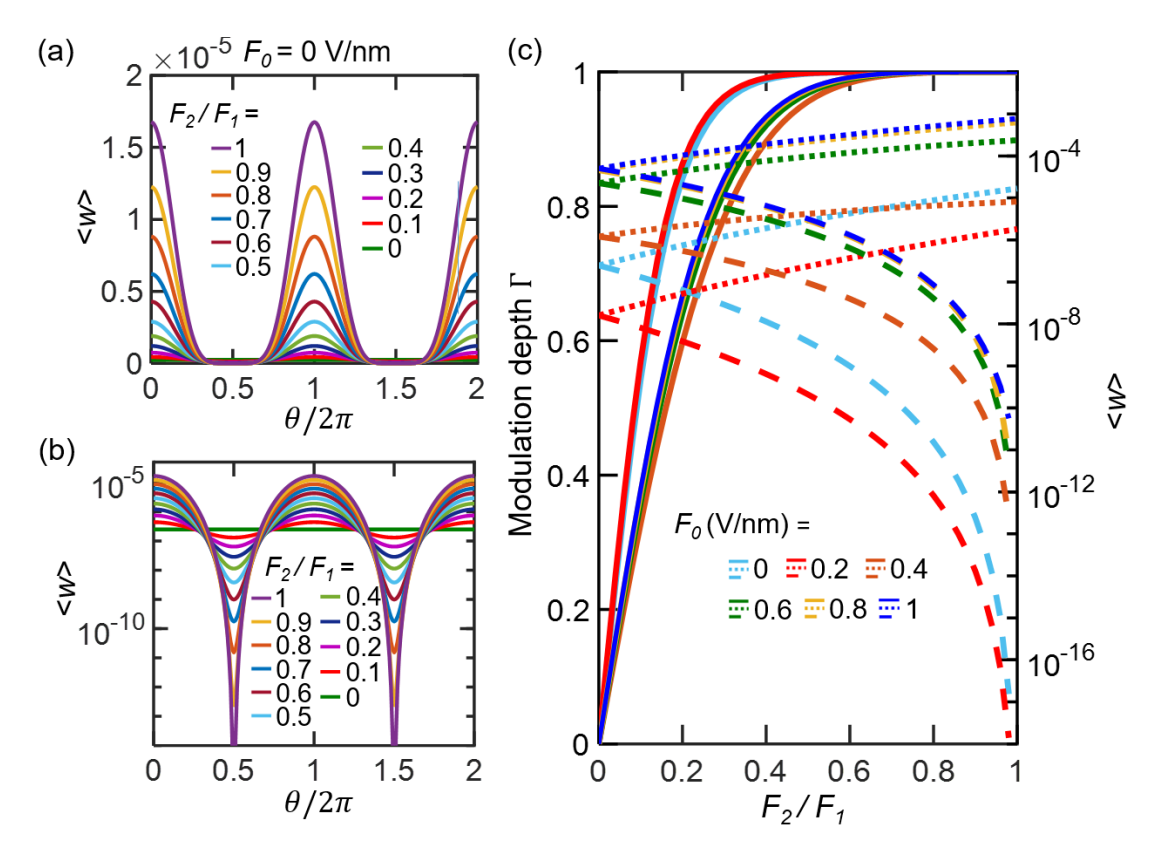


Figure 3.2: Photoemission current modulation. (a) Normalized total time-averaged emission current density < w > as a function of phase difference  $\theta$  for different  $F_2/F_1$ , when the dc field  $F_0 = 0$ . (b) Semilog plot of < w > in (a). (c) Current modulation depth  $\Gamma$  (solid lines) as a function of the laser field ratio  $F_2/F_1$  for different dc fields  $F_0$ . Dotted (dashed) lines in (c) are for the maximum (minimum) emission current density < w > at  $\theta = 0$  ( $\theta = \pi$ ). Here, the laser field  $F_1$  is fixed as 1.8 V/nm.

The sinusoidal modulation in the total emission current density  $\langle w \rangle$  is shown in Figures 3.2(a) and 3.2(b), for the case of  $F_0 = 0$  V/nm. When the laser field ratio  $F_2/F_1$  increases, the maximum emission current  $\langle w \rangle_{max}$  at  $\theta = 0$  increases, while the minimum emission current  $\langle w \rangle_{min}$  at  $\theta = \pi$  decreases, due to the more profound interference of the two lasers. Figure 3.2(c) shows the modulation depth,  $\Gamma = (\langle w \rangle_{max} - \langle w \rangle_{min})/(\langle w \rangle_{max} + \langle w \rangle_{min})$ , as a function of laser field ratio  $F_2/F_1$  under different dc fields  $F_0$ . For a given  $F_0$ ,  $\Gamma$  increases as  $F_2/F_1$  increases, and it reaches the maximum value of 100% when  $F_1 = F_2$ . It is important to note that, in order to reach a large modulation depth ( $\Gamma \geq 90\%$ ), only a small laser field ratio  $F_2/F_1$  is needed even with a strong dc

field, e.g.,  $F_2/F_1 \le 0.4$  when  $F_0 = 1$  V/nm. The dependence of  $\Gamma$  on the dc field  $F_0$  (see Figure 3.2(c)) is not monotonic and will be examined further in Figure 3.3 below.

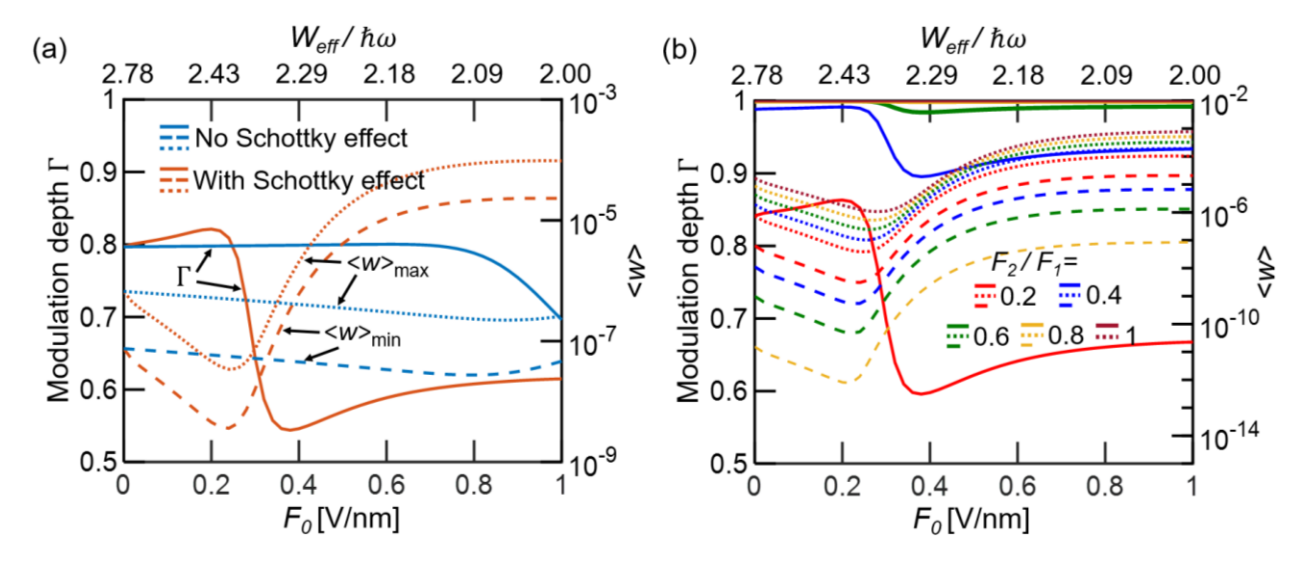


Figure 3.3: (a) Emission current modulation depth  $\Gamma$  (solid lines) as a function of the dc field  $F_0$  with and without the image-charge-induced potential barrier lowering (or the Schottky effect), for laser fields  $F_1 = 1.8$  V/nm and  $F_2 = 0.3$  V/nm. The case without Schottky effect is calculated by replacing  $W_{eff}$  with the nominal work function of metal W in Equation (27). (b) Modulation depth  $\Gamma$  (solid lines) as a function of  $F_0$  for different laser field ratios  $F_2/F_1$ , with the effective work function  $W_{eff}$ .  $F_1$  is fixed at 1.8 V/nm in (b). In (a),(b), the dotted (dashed) lines are for the maximum (minimum) emission current density < w > at  $\theta = 0$  ( $\theta = \pi$ ).

As discussed before, besides making the surface potential barrier narrower, the dc bias induces a reduction of the barrier height via the image charge effect (or the Schottky effect), which strongly influences the photoemission processes [6][62]. In Figure 3.3(a), we compare the emission current modulation depth  $\Gamma$  as a function of the dc field  $F_0$  with and without the Schottky effect. When Schottky effect is not considered,  $\Gamma$  gradually decreases with  $F_0$ . It is clear that the Schottky effect greatly alters the dependence of modulation depth  $\Gamma$  on the dc field  $F_0$  (see solid lines in Figure 3.3(a)). The change of  $\Gamma$  originates from the change of the maximum (minimum) values of emission current  $\langle w \rangle$  with the Schottky effect, as shown by dotted (dashed) lines in Figure 3.3(a). As  $F_0$  varies, the effective potential barrier  $W_{eff}$  changes, which induces an increase (decrease) in

the emission current when the ratio  $W_{eff}/\hbar\omega$  becomes closer to (further away from) an integer, where resonant n-photon absorption occurs (see Figures 6 and 7 of Reference [6]). This resonant emission process causes the nonlinear behavior of  $\Gamma$  as a function of dc field  $F_0$ .

Figure 3.3(b) shows the modulation depth  $\Gamma$  as a function of the dc field  $F_0$  for different laser field ratios  $F_2/F_1$  with fixed  $F_1=1.8$  V/nm. As  $F_2/F_1$  approaches 1, the modulation depth  $\Gamma$  gradually approaches the maximum value of 1 for the full range of dc field  $F_0$  from 0 to 1 V/nm. This is consistent with the observation in Figure 3.2(c). Note that when  $F_0$  is increased from 0 to 1 V/nm, the total emission current density can be increased by orders of magnitude.

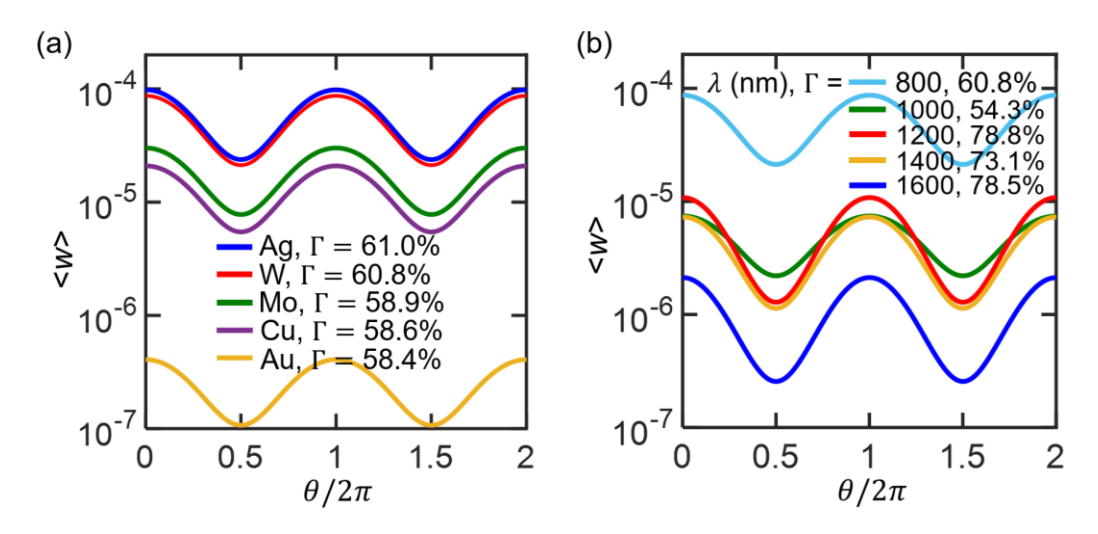


Figure 3.4: Normalized total time-averaged emission current density < w > as a function of the phase difference  $\theta$ , for various (a) cathode materials and (b) incident wavelengths. In (a), the laser wavelength  $\lambda = 800$  nm ( $\hbar \omega = 1.55$  eV). The nominal work function of different materials is  $W_{\rm Ag} = 4.26$  eV [107],  $W_{\rm w} = 4.31$  eV [57][60],  $W_{\rm Mo} = 4.6$  eV [107],  $W_{\rm Cu} = 4.65$  eV [107], and  $W_{\rm Au} = 5.1$  eV [6][107]. In (b), the metal is tungsten. Here, the dc field  $F_0$  is 0.8 V/nm and the laser fields  $F_1$  and  $F_2$  are fixed at 1.8 and 0.3 V/nm, respectively.

We also examine the photoemission current modulation depth  $\Gamma$  for cathode materials with different work functions in Figure 3.4(a) and for various incident laser wavelengths in Figure 3.4(b). We fix the dc field  $F_0 = 0.8$  V/nm and laser fields  $F_1 = 1.8$  V/nm and  $F_2 = 0.3$  V/nm. Under the same illumination condition, the electron emission current depends strongly on the work

function; however, the modulation depth  $\Gamma$  varies only slightly. This is because  $\Gamma$  is predominantly determined by the ratio of the laser field strengths. Figure 3.4(b) shows the effect of laser wavelength on both emission current and modulation depth for a tungsten cathode. The nonlinear dependence may also be attributed to the change of the ratio  $W_{eff}/\hbar\omega$  near resonant n-photon processes [6].

### 3.4 Conclusion

In this chapter, we propose to utilize two lasers of the same frequency to modulate the photoelectron emission by their phase delay. Compared to the two-color laser configuration, single-frequency laser pairs can be more easily implemented in experiments since they relax the requirement of higher order harmonic generation, which becomes increasingly difficult in the high laser intensity regimes. The intensity ratio of the single-frequency laser pairs can be tuned over a much wider range than the two-color laser system. Using the quantum model, we find a strong current modulation (> 90%) can be achieved with a moderate ratio of the laser fields (< 0.4) even under strong dc bias. The nonlinear effects of dc field, cathode materials, and laser wavelength on both the emission current level and modulation depth are also examined. The strong dependence of photoelectron energy spectra on the phase delay of the two lasers demonstrates a promising potential for the application of time-resolved photoelectron spectroscopy using single-frequency laser pairs.

#### **CHAPTER 4**

#### FEW-CYCLE LASER PULSES INDUCED PHOTOEMISSION

#### 4.1 Introduction

Ultrashort pulsed laser induced photoelectron emission from nanostructure enables the control of electron motion on the sub-optical-cycle time scale, by tuning the laser pulse's carrier-envelope phase (CEP) [13][19][54]. This may pave the way towards the subfemtosecond and subnanometer probing of electron motion in solid-state systems and the generation and measurement of attosecond electron pulses. While there have been recent efforts to develop analytical quantum models for continuous-wave laser excitation (see Chapters 2 and 3) [6][61][62][74], numerical simulations are typically implemented to study photoemission due to ultrashort pulsed lasers [13][76][78]. Fowler-Nordheim equation based models are commonly used to calculate the ultrashort pulsed photoemission rate [8][19][55] but it is only valid in the strong optical field regime (see section 1.3). To explicitly reveal the interplay of various emission processes under different regimes and to systematically characterize the parametric scalings of photoemission characteristics, an exact quantum theory under ultrashort pulsed condition is highly desirable.

In this chapter, we present a quantum analytical solution for ultrafast photoelectron emission from a dc-biased metal surface illuminated by few-cycle laser pulses, by exactly solving the TDSE. Our solution is valid from the photon-driven emission regime in low intensity optical fields to the optical-field-driven regime in high intensity optical fields, and is applicable for arbitrary laser parameters (i.e., intensity, pulse duration, carrier frequency and CEP), dc bias, and metal properties (i.e., work function and Fermi level). The model is also applicable to a train of laser pulses with arbitrary pulse repetition rate. Using the analytical formulation, we examine the photoemission properties, including energy spectra, photocurrent or emission charge density, with various

combinations of laser parameters and dc bias, exhibiting good agreement with the experimental observations [13][54][55]. This work offers clear insights to the photoelectron energy distribution and spatiotemporal dynamics of electron emission under different driving pulsed laser and dc electric fields. The material of this chapter is based on our published paper in Reference [56] and is presented with permission from the copyright holder.

## 4.2 Analytical Formulation

Our one-dimensional (1D) model considers electrons with the initial energy  $\varepsilon$  emitted from the metal-vacuum interface at x = 0 under a dc electric field  $F_0$  and an optical electric field (see Figure 4.1) of a Gaussian laser pulse train with a time period T = 2L of the form,

$$F(t) = F_1 e^{-t^2/\sigma^2} \cos(\omega t + \phi),$$
  $(2l-1)L < t \le (2l+1)L$ , with  $l = 0, \pm 1, \pm 2, ...$ , (32) where  $F_1$  is the peak of optical field strength,  $\sigma = \tau_p/(2\sqrt{ln2}) \cong \tau_p/1.665$  with  $\tau_p$  being the full width at half maximum (FWHM) of the field envelope,  $\omega$  is the angular frequency of the carrier wave, and  $\phi$  is the CEP. All the laser pulses are CEP stabilized with  $\omega = m\pi/L = m\omega_E$ , with  $m$  being a positive integer and  $\omega_E$  the pulse repetition frequency [108]. When  $L/\tau_p \gg 1$ , the temporal interaction between consecutive laser pulses becomes negligible and  $F(t)$  can be used to study photoemission due to a single laser pulse. By taking the Fourier series, the laser field in Equation (32) can be expressed as,

$$F(t) = F_1 a_0 \cos \phi + \sum_{\substack{n = -\infty \\ n \neq 0}}^{+\infty} F_1 a_n \cos(n\omega_E t + \phi)$$
(33)

where  $a_0 = \frac{1}{L} \int_0^L e^{-t^2/\sigma^2} \cos(m\omega_E t) dt$ , and  $a_n = \frac{1}{L} \int_0^L e^{-t^2/\sigma^2} \cos[(n-m)\omega_E t] dt$ . From Equation (33), it is clear that the incident laser pulse train is a superposition of sine waves with frequencies separated by  $\omega_E$ . We assume the laser electric field is spatially uniform and perpendicular to the metal surface; thus the time-dependent potential barrier near the meatal-vacuum interface is

[6][56][61][62][74][106],

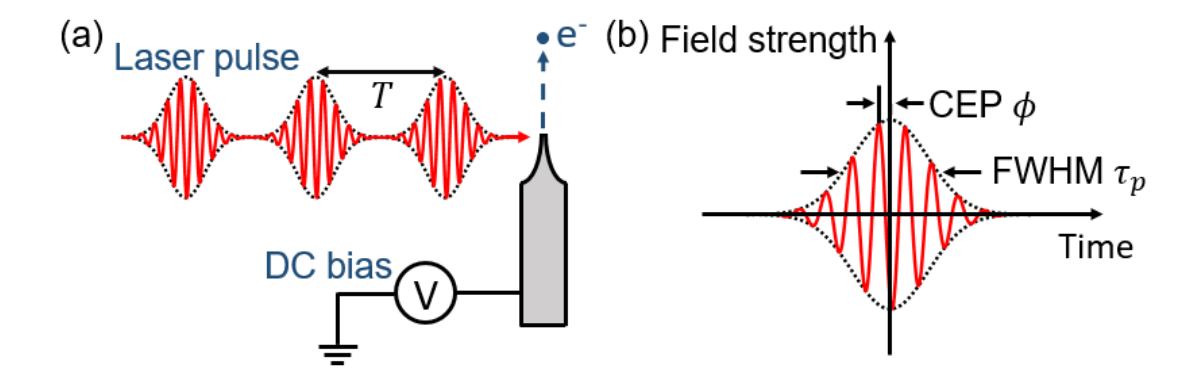


Figure 4.1: (a) Sketch of photoelectron emission from a biased emitter under the illumination of a laser pulse train with a time period T. (b) A single laser pulse with carrier-envelope phase (CEP)  $\phi$  and full width at half maximum (FWHM) of the field envelope  $\tau_p$ . The red curve and black dotted lines denote the time evolution of laser electric field and laser pulse envelope, respectively.

$$\Phi(x,t) = \begin{cases} 0, & x < 0 \\ E_F + W_{eff} - eF_0 x - eF(t) x, & x \ge 0, \end{cases}$$
 (34)

where  $E_F$  is the Fermi energy of the metal cathode,  $W_{eff} = W - 2\sqrt{e^3F_0/16\pi\varepsilon_0}$  is the effective work function with Schottky effect [6][62], with W being the nominal work function, e is the elementary charge,  $\varepsilon_0$  is the free space permittivity, and F(t) is given by Equation (33).

By solving the TDSE with the potential energy given in Equation (34), the exact solution of electron wave function for  $x \ge 0$  (in the vacuum) is found to be (see Appendix C for the method),

$$\psi(x,t) = \sum_{l=-\infty}^{\infty} T_l [Ai(-\eta_l) - iBi(-\eta_l)] \times \exp\left(-i\frac{\varepsilon}{\hbar}t - il\omega_E t\right)$$

$$\times \exp\left(\frac{ieF_1}{\hbar}Gx + \frac{ie^2F_1^2}{8\hbar m_e}M - \frac{ie^2(F_0 + F_1a_0\cos\phi)F_1}{\hbar m_e}N - \frac{ie^2F_1^2}{4\hbar m_e\omega_E^2}R\right), \quad x \ge 0 \quad (35)$$

where  $\varepsilon$  is the electron initial energy,  $G = \sum_{n=-\infty, n\neq 0}^{+\infty} \frac{a_n \sin{(n\omega_E t + \phi)}}{n\omega_E}$ ; M =

$$\sum_{n=-\infty,n\neq 0}^{+\infty} \frac{a_n^2 \sin(2n\omega_E t + 2\phi) + a_n a_{-n} \sin(2n\omega_E t)}{n^3 \omega_E^3} \quad ; \quad N = \sum_{n=-\infty,n\neq 0}^{+\infty} \frac{a_n \sin(n\omega_E t + \phi)}{n^3 \omega_E^3} \quad ; \quad R = \sum_{n=-\infty,n\neq 0}^{+\infty} \frac{a_n \sin(n\omega_E t + \phi)}{n^3 \omega_E^3} \quad ; \quad R = \sum_{n=-\infty,n\neq 0}^{+\infty} \frac{a_n \sin(n\omega_E t + \phi)}{n^3 \omega_E^3} \quad ; \quad R = \sum_{n=-\infty,n\neq 0}^{+\infty} \frac{a_n \sin(n\omega_E t + \phi)}{n^3 \omega_E^3} \quad ; \quad R = \sum_{n=-\infty,n\neq 0}^{+\infty} \frac{a_n \sin(n\omega_E t + \phi)}{n^3 \omega_E^3} \quad ; \quad R = \sum_{n=-\infty,n\neq 0}^{+\infty} \frac{a_n \sin(n\omega_E t + \phi)}{n^3 \omega_E^3} \quad ; \quad R = \sum_{n=-\infty,n\neq 0}^{+\infty} \frac{a_n \sin(n\omega_E t + \phi)}{n^3 \omega_E^3} \quad ; \quad R = \sum_{n=-\infty,n\neq 0}^{+\infty} \frac{a_n \sin(n\omega_E t + \phi)}{n^3 \omega_E^3} \quad ; \quad R = \sum_{n=-\infty,n\neq 0}^{+\infty} \frac{a_n \sin(n\omega_E t + \phi)}{n^3 \omega_E^3} \quad ; \quad R = \sum_{n=-\infty,n\neq 0}^{+\infty} \frac{a_n \sin(n\omega_E t + \phi)}{n^3 \omega_E^3} \quad ; \quad R = \sum_{n=-\infty,n\neq 0}^{+\infty} \frac{a_n \sin(n\omega_E t + \phi)}{n^3 \omega_E^3} \quad ; \quad R = \sum_{n=-\infty,n\neq 0}^{+\infty} \frac{a_n \sin(n\omega_E t + \phi)}{n^3 \omega_E^3} \quad ; \quad R = \sum_{n=-\infty,n\neq 0}^{+\infty} \frac{a_n \sin(n\omega_E t + \phi)}{n^3 \omega_E^3} \quad ; \quad R = \sum_{n=-\infty,n\neq 0}^{+\infty} \frac{a_n \sin(n\omega_E t + \phi)}{n^3 \omega_E^3} \quad ; \quad R = \sum_{n=-\infty,n\neq 0}^{+\infty} \frac{a_n \sin(n\omega_E t + \phi)}{n^3 \omega_E^3} \quad ; \quad R = \sum_{n=-\infty,n\neq 0}^{+\infty} \frac{a_n \sin(n\omega_E t + \phi)}{n^3 \omega_E^3} \quad ; \quad R = \sum_{n=-\infty,n\neq 0}^{+\infty} \frac{a_n \sin(n\omega_E t + \phi)}{n^3 \omega_E^3} \quad ; \quad R = \sum_{n=-\infty,n\neq 0}^{+\infty} \frac{a_n \sin(n\omega_E t + \phi)}{n^3 \omega_E^3} \quad ; \quad R = \sum_{n=-\infty,n\neq 0}^{+\infty} \frac{a_n \sin(n\omega_E t + \phi)}{n^3 \omega_E^3} \quad ; \quad R = \sum_{n=-\infty,n\neq 0}^{+\infty} \frac{a_n \sin(n\omega_E t + \phi)}{n^3 \omega_E^3} \quad ; \quad R = \sum_{n=-\infty,n\neq 0}^{+\infty} \frac{a_n \sin(n\omega_E t + \phi)}{n^3 \omega_E^3} \quad ; \quad R = \sum_{n=-\infty,n\neq 0}^{+\infty} \frac{a_n \sin(n\omega_E t + \phi)}{n^3 \omega_E^3} \quad ; \quad R = \sum_{n=-\infty,n\neq 0}^{+\infty} \frac{a_n \sin(n\omega_E t + \phi)}{n^3 \omega_E^3} \quad ; \quad R = \sum_{n=-\infty,n\neq 0}^{+\infty} \frac{a_n \cos(n\omega_E t + \phi)}{n^3 \omega_E^3} \quad ; \quad R = \sum_{n=-\infty,n\neq 0}^{+\infty} \frac{a_n \cos(n\omega_E t + \phi)}{n^3 \omega_E^3} \quad ; \quad R = \sum_{n=-\infty,n\neq 0}^{+\infty} \frac{a_n \cos(n\omega_E t + \phi)}{n^3 \omega_E^3} \quad ; \quad R = \sum_{n=-\infty,n\neq 0}^{+\infty} \frac{a_n \cos(n\omega_E t + \phi)}{n^3 \omega_E^3} \quad ; \quad R = \sum_{n=-\infty,n\neq 0}^{+\infty} \frac{a_n \cos(n\omega_E t + \phi)}{n^3 \omega_E^3} \quad ; \quad R = \sum_{n=-\infty,n\neq 0}^{+\infty} \frac{a_n \cos(n\omega_E t + \phi)}{n^3 \omega_E^3} \quad ; \quad R = \sum_{n=-\infty,n\neq 0}^{+\infty} \frac{a_n \cos(n\omega_E t + \phi)}{n^3 \omega_E^3} \quad ; \quad R = \sum_{n=-\infty,n\neq 0}^{+\infty} \frac{a_n \cos(n\omega_E t + \phi)}{n^3 \omega_E^3} \quad ; \quad R = \sum_{n=-\infty,n\neq 0}^{+\infty} \frac{a_n \cos(n\omega_E t + \phi)}{n^3 \omega_E^3} \quad ; \quad R = \sum_{$$

$$\begin{split} & \sum_{n=-\infty,n\neq 0}^{+\infty} \sum_{m=-\infty,m\neq 0,n,-n}^{+\infty} \frac{a_m a_n}{mn} \Big\{ \frac{\sin\left[(n-m)\omega_E t\right]}{(n-m)\omega_E} - \frac{\sin\left[(n+m)\omega_E t+2\phi\right]}{(n+m)\omega_E} \Big\} \; ; \;\; \eta_l = \left[\frac{E_l}{e(F_0+F_1 a_0 \cos\phi)} + x + \frac{E_l}{e(F_0+F_1 a_0 \cos\phi)} + x + \frac{E_l}{e(F_0+F_1 a_0 \cos\phi)} \right]^{1/3} \; ; \;\; \text{the drift kinetic energy} \;\; E_l = \varepsilon + l\hbar\omega_E - E_F - \frac{E_l}{e(F_0+F_1 a_0 \cos\phi)} \Big[ \frac{2em_e(F_0+F_1 a_0 \cos\phi)}{\hbar^2} \Big]^{1/3} \; ; \;\; \text{the drift kinetic energy} \;\; E_l = \varepsilon + l\hbar\omega_E - E_F - \frac{E_l}{e(F_0+F_1 a_0 \cos\phi)} \Big[ \frac{e^2F_1^2[a_n^2 + a_n a_{-n} \cos(2\phi)]}{4m_e n^2 \omega_E^2} \Big] \; ; \;\; Ai \;\; \text{and} \;\; Bi \;\; \text{are the Airy functions of the first kind and second kind respectively, showing an outgoing wave traveling} \;\; \text{towards the} \;\; +x \;\; \text{direction} \;\; [6][81][86]; \;\; \text{and} \;\; T_l \;\; \text{represents the transmission coefficient.} \end{split}$$

For x < 0 (inside the cathode), the exact solution of electron wave function is,

$$\psi(x,t) = \exp\left(-\frac{i\varepsilon t}{\hbar} + ik_0 x\right) + \sum_{l=-\infty}^{\infty} R_l \exp\left(-i\frac{\varepsilon + l\hbar\omega_E}{\hbar}t - ik_l x\right), \quad x < 0$$
 (36)

which shows the superposition of an incident plane wave with initial energy  $\varepsilon$  and a set of reflected plane waves with reflection coefficient  $R_l$  and energies  $\varepsilon + l\hbar\omega_E$ , where the wavenumbers  $k_0 = \sqrt{2m_e\varepsilon/\hbar^2}$  and  $k_l = \sqrt{2m_e(\varepsilon + l\hbar\omega_E)/\hbar^2}$ .

By imposing the boundary conditions that both the electron wave function  $\psi(x,t)$  and its derivative  $\partial \psi(x,t)/\partial x$  are continuous at x=0 and taking the Fourier transform, we obtain, in nondimensional quantities [6][56][61][62],  $\bar{\varepsilon}=\varepsilon/W_{eff}$ ,  $\bar{\omega}_E=\omega_E\hbar/W_{eff}$ ,  $\bar{t}=tW_{eff}/\hbar$ ,  $\bar{E}_F=E_F/W_{eff}$ ,  $\bar{x}=x/\lambda_0$ ,  $\lambda_0=\sqrt{\hbar^2/2m_eW_{eff}}$ ,  $\bar{F}_0=F_0e\lambda_0/W_{eff}$ ,  $\bar{F}_1=F_1e\lambda_0/W_{eff}$ ,  $\bar{U}_p=U_p/W_{eff}$ ,

$$2\sqrt{\bar{\varepsilon}}\delta(k) = \sum_{l=-\infty}^{\infty} T_l \left[ \sqrt{\bar{\varepsilon} + k\bar{\omega}_E} P_{l(l-k)} + Q_{l(l-k)} \right]$$
 (37)

where  $\delta(k)$ ,  $P_{l(l-k)}$ , and  $Q_{l(l-k)}$  are,

$$\delta(k) = \begin{cases} 1, & k = 0, \\ 0, & k \neq 0, \end{cases} \tag{38a}$$

$$P_{nl} = \frac{1}{2\pi} \int_{0}^{2\pi} p_{n}(\overline{\omega}_{E}\overline{t}) e^{-il\overline{\omega}_{E}\overline{t}} d(\overline{\omega}_{E}\overline{t}), \quad Q_{nl} = \frac{1}{2\pi} \int_{0}^{2\pi} q_{n}(\overline{\omega}_{E}\overline{t}) e^{-il\overline{\omega}_{E}\overline{t}} d(\overline{\omega}_{E}\overline{t}), \quad (38b)$$

$$p_n(\bar{\omega}_E \bar{t}) = \phi(\bar{\omega}_E \bar{t})[Ai(\alpha_n) - iBi(\alpha_n)], \tag{38c}$$

$$q_n(\bar{\omega}_E \bar{t}) = \phi(\bar{\omega}_E \bar{t}) z_n(\bar{\omega}_E \bar{t}), \tag{38d}$$

$$\phi(\bar{\omega}_{E}\bar{t}) = e^{i\frac{\bar{F}_{1}^{2}}{4}\bar{M} - 2i(\bar{F}_{0} + \bar{F}_{1}a_{0}\cos\phi)\bar{F}_{1}\bar{N} - i\frac{\bar{F}_{1}^{2}}{2\bar{\omega}_{E}^{2}}\bar{R}},$$
(38e)

$$z_n(\overline{\omega}\overline{t}) = \overline{F}_1[Ai(\alpha_n) - iBi(\alpha_n)]\overline{G} + (\overline{F}_0 + \overline{F}_1a_0\cos\phi)^{1/3}[iAi'(\alpha_n) + Bi'(\alpha_n)], \qquad (38f)$$

where 
$$\overline{G} = \sum_{n=-\infty,n\neq 0}^{+\infty} \frac{a_n \sin{(n\bar{\omega}_E\bar{t}+\phi)}}{n\bar{\omega}_E}$$
 ,  $\overline{M} = \sum_{n=-\infty,n\neq 0}^{+\infty} \frac{a_n^2 \sin{(2n\bar{\omega}_E\bar{t}+2\phi)} + a_n a_{-n} \sin{(2n\bar{\omega}_E\bar{t})}}{n^3\bar{\omega}_F^3}$  ,  $\overline{N} = \sum_{n=-\infty,n\neq 0}^{+\infty} \frac{a_n^2 \sin{(2n\bar{\omega}_E\bar{t}+2\phi)} + a_n a_{-n} \sin{(2n\bar{\omega}_E\bar{t})}}{n^3\bar{\omega}_F^3}$ 

$$\alpha_n = -(\overline{F}_0 + \overline{F}_1 a_0 \cos\phi)^{1/3} \left[ \frac{\overline{E}_n}{\overline{F}_0 + \overline{F}_1 a_0 \cos\phi} + \sum_{l=-\infty, l\neq 0}^{+\infty} \frac{2\overline{F}_1 a_l \cos(l\overline{\omega}_E \overline{t} + \phi)}{l^2 \overline{\omega}_E^2} \right], \text{ and } \overline{E}_n = \overline{\varepsilon} + n\overline{\omega}_E - \overline{E}_F - \frac{\overline{E}_n}{2} \left[ \frac{\overline{E}_n}{\overline{E}_n + \overline{E}_n a_0 \cos\phi} + \sum_{l=-\infty, l\neq 0}^{+\infty} \frac{2\overline{F}_n a_l \cos(l\overline{\omega}_E \overline{t} + \phi)}{l^2 \overline{\omega}_E^2} \right].$$

 $\overline{U}_p - 1$ . Here,  $p_n(\overline{\omega}_E \overline{t})$  and  $q_n(\overline{\omega}_E \overline{t})$  in Equations (38c) and (38d) denote the phase factor of the nth-state wave function and of its spatial derivative at  $\overline{x} = 0$ , respectively.  $P_{nl}$  and  $Q_{nl}$  are the lth Fourier coefficient of  $p_n(\overline{\omega}_E \overline{t})$  and  $q_n(\overline{\omega}_E \overline{t})$ , respectively. Then, the transmission coefficient  $T_n$  (and reflection coefficient  $R_n$ ) can be obtained from Equation (37).

Following the probability current density  $J(x,t)=(i\hbar/2m)(\psi\partial\psi^*/\partial x-\psi^*\partial\psi/\partial x)=(i\hbar/2m_e)\sum_{n=-\infty}^{\infty}\sum_{l=-\infty}^{\infty}(\psi_n\,\partial\psi_l^*/\partial x-\psi_n^*\,\partial\psi_l/\partial x)$ , the normalized emission current density is defined as the ratio of the transmitted probability current density over the incident probability current density,  $w(\varepsilon,x,t)=J_t(\varepsilon,x,t)/J_i(\varepsilon,x,t)$ . Thus, we obtain the normalized instantaneous photoemission current density,

$$w(\bar{\varepsilon}, \bar{x}, \bar{t}) = \frac{1}{\sqrt{\bar{\varepsilon}}} \sum_{n=-\infty}^{\infty} \sum_{l=-\infty}^{\infty} \operatorname{Im} \left[ e^{i(l-n)\bar{\omega}_E \bar{t}} T_n T_l^* (\bar{C} + i\bar{D}) \right], \tag{39}$$

where 
$$\overline{C} = \overline{F}_1[Ai(-\overline{\eta}_l)Bi(-\overline{\eta}_n) - Ai(-\overline{\eta}_n)Bi(-\overline{\eta}_l)]\overline{G} + (\overline{F}_0 + \overline{F}_1a_0\cos\phi)^{1/3}[Ai(-\overline{\eta}_n)Ai'(-\overline{\eta}_l) + Bi(-\overline{\eta}_n)Bi'(-\overline{\eta}_l)]\overline{G} + (\overline{F}_0 + \overline{F}_1[Ai(-\overline{\eta}_n)Ai(-\overline{\eta}_l) + Bi(-\overline{\eta}_n)Bi(-\overline{\eta}_l)]\overline{G} + (\overline{F}_0 + \overline{G}_n)Bi'(-\overline{\eta}_n)Bi'(-\overline$$

 $\overline{F}_1 a_0 \cos\phi)^{1/3} \left[ Ai \left( -\overline{\eta}_n \right) Bi \left( -\overline{\eta}_l \right) - Bi \left( -\overline{\eta}_n \right) Ai \left( -\overline{\eta}_l \right) \right], \quad \overline{G} = \sum_{n=-\infty, n\neq 0}^{+\infty} \frac{a_n \sin\left(n\overline{\omega}_E \overline{t} + \phi\right)}{n\overline{\omega}_E} \,, \quad \text{and} \quad \overline{\eta}_n = \\ \left( \overline{F}_0 + \overline{F}_1 a_0 \cos\phi \right)^{1/3} \left[ \frac{\overline{\epsilon} + n\overline{\omega}_E - \overline{E}_F - \overline{U}_p - 1}{\overline{F}_0 + \overline{F}_1 a_0 \cos\phi} + \sum_{l=-\infty, l\neq 0}^{+\infty} \frac{2\overline{F}_1 a_l \cos(l\overline{\omega}_E \overline{t} + \phi)}{l^2 \overline{\omega}_E^2} + \overline{x} \right] \,. \quad \text{The normalized time-averaged photoemission current density over one laser pulse is defined as the ratio of the total emission charge density $Q$ due to a single laser pulse and the length $\tau_p$, }$ 

$$\langle w(\bar{\varepsilon}) \rangle = \frac{Q}{\tau_p} = \sum_{n=-\infty}^{\infty} \langle w_n(\bar{\varepsilon}) \rangle, \quad \langle w_n(\bar{\varepsilon}) \rangle = |T_n|^2 \frac{(\bar{F}_0 + \bar{F}_1 a_0 \cos \phi)^{1/3}}{\pi \sqrt{\bar{\varepsilon}}} \frac{2L}{\tau_p}, \tag{40}$$

where  $\langle w_n(\bar{\varepsilon}) \rangle$  denotes the time-averaged emission current density through the *n*th channel, with emitted electron energy  $\varepsilon + n\hbar\omega_E$ .

For the special case of dc field  $F_0=0$  and CEP  $\phi=\pi/2$ , the electron wave function for  $x\geq 0$  is revised by displacing  $[Ai(-\eta_l)-iBi(-\eta_l)]$  in Equation (35) with  $\exp\{i[\ x+\sum_{n=-\infty,n\neq 0}^{+\infty}\frac{eF_1a_n\cos(n\omega_Et+\phi)}{n^2\omega_E^2m_e}]\sqrt{2m_eE_l}/\hbar\}$ . The transmission coefficient  $T_n$  is still calculated from Equation (37) with  $P_{nl}$  and  $Q_{nl}$  unchanged, but with  $p_n(\omega t)=\phi(\bar{\omega}_E\bar{t})\exp[i\sqrt{\bar{E}_n}\sum_{l=-\infty,l\neq 0}^{+\infty}\frac{2\bar{F}_1a_l\cos(l\bar{\omega}_E\bar{t}+\phi)}{l^2\bar{\omega}_E^2}]$  and  $q_n(\omega t)=p_n(\omega t)[\sqrt{\bar{E}_n}+\sum_{l=-\infty,l\neq 0}^{+\infty}\frac{\bar{F}_1a_l\sin(l\bar{\omega}_E\bar{t}+\phi)}{l\bar{\omega}_E}]$ .

The normalized photoemission current density becomes,

$$w(\bar{\varepsilon}, \bar{x}, \bar{t}) = \frac{1}{\sqrt{\bar{\varepsilon}}} \sum_{n=-\infty}^{\infty} \sum_{l=-\infty}^{\infty} \operatorname{Im} \left[ i e^{i(l-n)\bar{\omega}_E \bar{t}} T_n T_l^* \bar{A} e^{i\bar{B}} \right], \tag{41}$$

$$\langle w(\bar{\varepsilon}) \rangle = \sum_{n=-\infty}^{\infty} \langle w_n(\bar{\varepsilon}) \rangle, \quad \langle w_n(\bar{\varepsilon}) \rangle = \frac{\text{Re}\left(|T_n|^2 \sqrt{\bar{E}_n}\right)}{\sqrt{\bar{\varepsilon}}} \frac{2L}{\tau_p}, \tag{42}$$

with 
$$\overline{A} = (\sqrt{\overline{E}_l})^* + \sum_{m=-\infty, m\neq 0}^{+\infty} \frac{\overline{F}_1 a_m \sin{(m\overline{\omega}_E \overline{t} + \phi)}}{m\overline{\omega}_E}$$
 and  $\overline{B} = [\sqrt{\overline{E}_n} - (\sqrt{\overline{E}_l})^*](\overline{x} + \overline{E}_l)^*$ 

 $\sum_{m=-\infty,m\neq 0}^{+\infty} \frac{2\overline{F}_1 a_m \cos(m\overline{\omega}_E \overline{t} + \phi)}{m^2 \overline{\omega}_E^2} \text{ (see Appendix C for the method)}.$ 

## 4.3 Results and Discussion

For the calculation of this chapter, unless specified otherwise, the default value of the laser wavelength is 800 nm (or laser period  $T_{\omega}$  of 2.67 fs), the cathode metal is assumed to be gold [6][11][76], with Fermi energy  $E_F = 5.53$  eV and work function W = 5.1 eV, the pulse width  $\tau_p = 8.8$  fs (i.e.,  $\sim 3$  cycles), the laser pulse repetition period T = 267 fs ( $\gg \tau_p$  to isolate a single laser pulse and avoid temporal interaction between adjacent laser pulses), the CEP  $\phi = 0$ , the dc field  $F_0 = 1 \times 10^4$  V/m and the peak laser field  $F_1 = 1 \times 10^9$  V/m. Since most of the electrons are emitted with initial energies near the Fermi level [6][76][86][87], we choose the electron initial energy  $\varepsilon = E_F$  for simplicity.

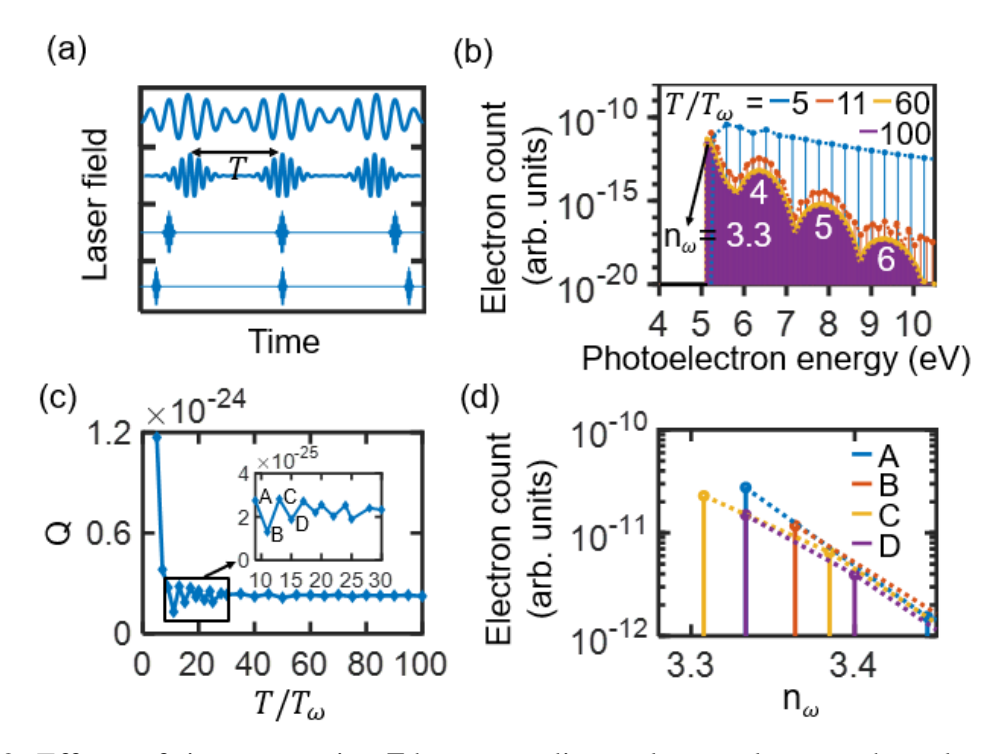


Figure 4.2: Effects of time separation T between adjacent laser pulses on photoelectron energy spectra and total emission charge density Q. (a) Laser electric field for different T. From top to bottom, T=13, 29, 160, and 276 fs, corresponding to  $T/T_{\omega}=5, 11, 60$ , and 100, respectively. (b) Energy spectra for different T.  $n_{\omega}$  denotes the laser photon order (with single photon energy  $\hbar\omega=1.55$  eV). (c) Q as a function of  $T/T_{\omega}$ . The inset shows the magnification of (c) between  $T/T_{\omega}=9$  and 30, where A, B, C and D denote  $T/T_{\omega}=9$ , 11, 13 and 15 respectively. (d) Photoelectron energy spectra near the maximum at A, B, C and D in the inset of (c).

In Figure 4.2, we show the photoelectron energy spectra and total emission charge density Q (=  $\langle w \rangle \tau_p$ ) for various time intervals T between adjacent laser pulses. It is found that as T decreases, photoelectron emission is gradually confined to a smaller number of emission channels but with more electron yield, because of the decreasing frequency ratio between laser carrier  $\omega$  and pulse repetition frequency  $\omega_E$  (see Figure 4.2(b)). The interaction of consecutive laser pulses leads to the smearing of multiphoton absorption peaks (with respect to laser photon energy  $\hbar\omega$ ) in the photoelectron energy spectra envelope with decreasing T. Figure 4.2(c) shows that when  $T/T_{\omega}$  < 9 the closely spaced laser pulse train induces a total emission charge Q per pulse that is significantly higher than that due to a well-separated single laser pulse. When T increases, Q decreases and eventually becomes independent of T when  $T/T_{\omega} > 60$ , indicating the laser pulses are well separated and the results may be regarded as that from a single laser pulse. It is interesting to note the oscillatory feature of Q in the range of  $9 < T/T_{\omega} < 60$  (see the inset of Figure 4.2(c)), due to the varying coherence interaction between neighboring pulses. Figure 4.2(d) compares the photoelectron energy spectra with different T in this oscillation regime (see A, B, C and D in the inset of Figure 4.2(c)), where both the peak electron emission yield and the dominant emission channel vary with T.

We evaluate the effect of CEP  $\phi$  on the photoelectron energy spectra and total emission current density  $\langle w \rangle$  for different pulse duration  $\tau_p$  in Figure 4.3. For small  $\tau_p$  (e.g., 4.4 fs, or 1.7 optical cycles), the spectral features are sinusoidally modulated with  $\phi$  (see Figure 4.3(b)). This is consistent with the experimental observation of CEP modulation in photoemission spectra with a few-cycle laser pulse [13][54]. As pulse width  $\tau_p$  increases, the CEP modulation on spectra becomes less pronounced, and the multiphoton peaks in spectra become narrower (see Figure 4.3(c)), gradually approaching those from continuous-wave excitation [6]. The energy spectra for

small  $\tau_p$  (= 4.4 fs) is enlarged in Figure 4.3(d), showing a higher electron yield and broader spectrum for  $\phi = 0$  than  $\phi = \pi$ . Figures 4.3(e) and 4.3(f) show that CEP modulation is important for a short laser pulse up to  $\tau_p/T_\omega \sim 4$  and the modulation of total photoemission current with  $\phi$  decreases for larger pulse width  $\tau_p$ .

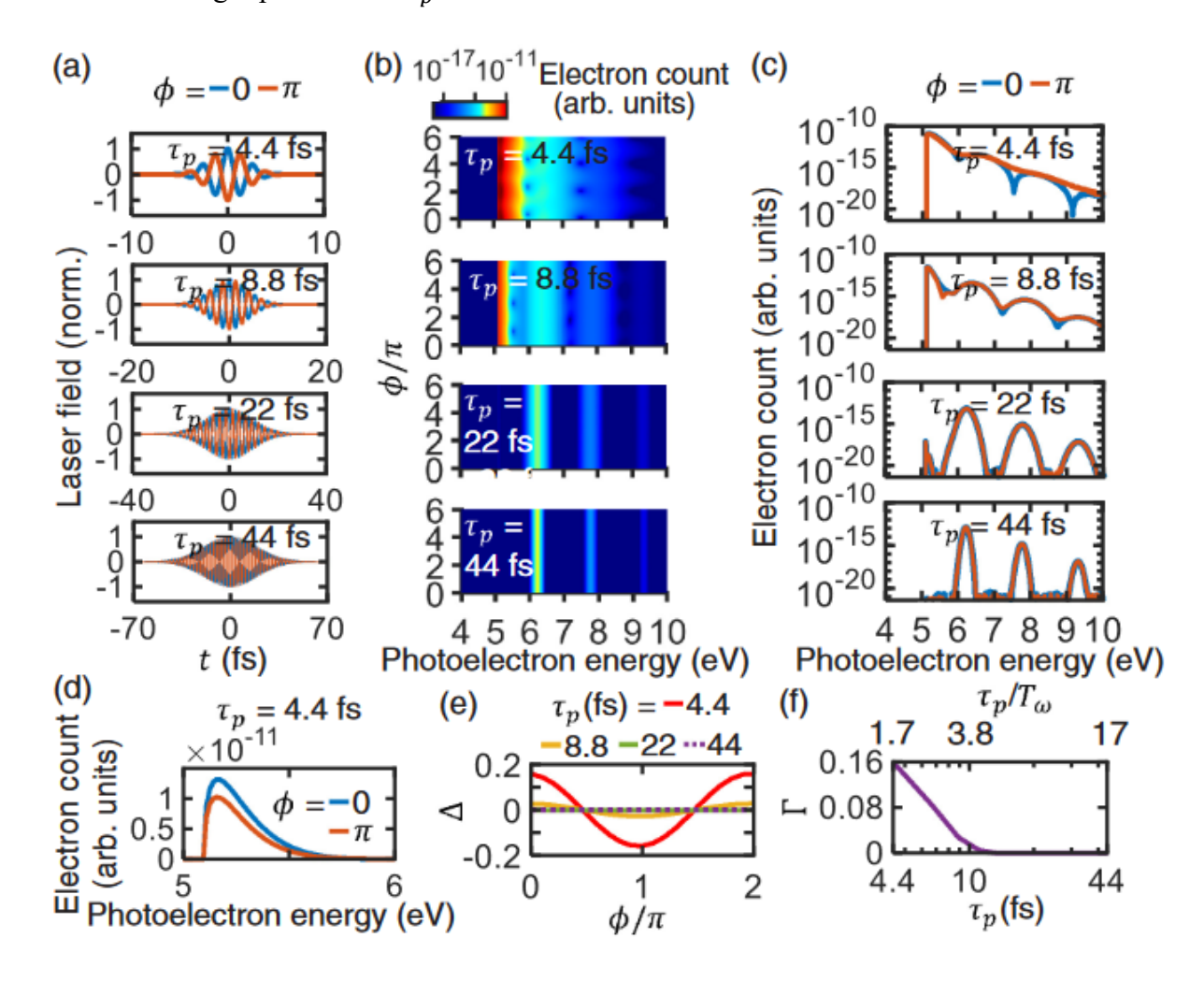


Figure 4.3: CEP modulation in energy spectra with different pulse duration  $\tau_p$ . (a) Laser electric field for different  $\tau_p$  when CEP  $\phi=0$  and  $\pi$ . (b) Energy spectra as a function of  $\phi$  for different  $\tau_p$ . (c) Extracted energy spectra of  $\phi=0$  and  $\pi$  from (b). (d) Linear plot of energy spectrum for  $\tau_p=4.4$  fs in (c). (e) Normalized current modulation magnitude  $\Delta=(< w>-< w>_{ave})/< w>_{ave}$  as a function of  $\phi$  for different  $\tau_p$ . Here,  $< w>_{ave}=(< w>_{max}+< w>_{min})/2$  denotes the averaged value of < w> with respect to  $\phi$ . (f) Current modulation depth  $\Gamma=(< w>_{max}-< w>_{min})/(< w>_{max}+< w>_{min})$  as a function of  $\tau_p$ .

We next examine the CEP sensitivity of photoelectron emission charge Q under different laser

fields  $F_1$ . As shown in Figures 4.4(a) and 4.4(b), in general, the CEP modulation on Q increases as  $F_1$  increases. Also, the position of  $\phi$  for the maximum (or minimum) Q shifts when the laser field  $F_1$  increases for a fixed pulse duration  $\tau_p$  (see the dashed lines in Figures 4.4(a) and 4.4(b)). To investigate the CEP sensitivity more closely, in Figure 4.4(c), we plot the difference between the maximum and minimum values of Q in the curves of Figures 4.4(a) and 4.4(b) as a function of  $F_1$ . Following Reference [55], by fitting the Q vs  $\phi$  curves with a sinusoidal function of  $F_1$ . Following Reference [55], by fitting the maximum Q with  $F_1$ , as shown in Figure 4.4(d). We see a pronounced dip in  $Q_{\text{max}}$ - $Q_{\text{min}}$  at large laser field  $F_1 = 9$  V/nm for both cases of  $\tau_p = 4.7$  and 8.8 fs, and for  $\tau_p = 8.8$  fs another dip appearing at  $F_1$ =5 V/nm (see Figure 4.4(c)). From Figure 4.4(d), phase shifts of  $\pi$  in  $\phi$  are found near these dips. These behaviors agree very well with the varnishing CEP sensitivity of photoemission accompanied by a  $\pi$  phase shift in the optical-field regime observed in recent experiments [55].

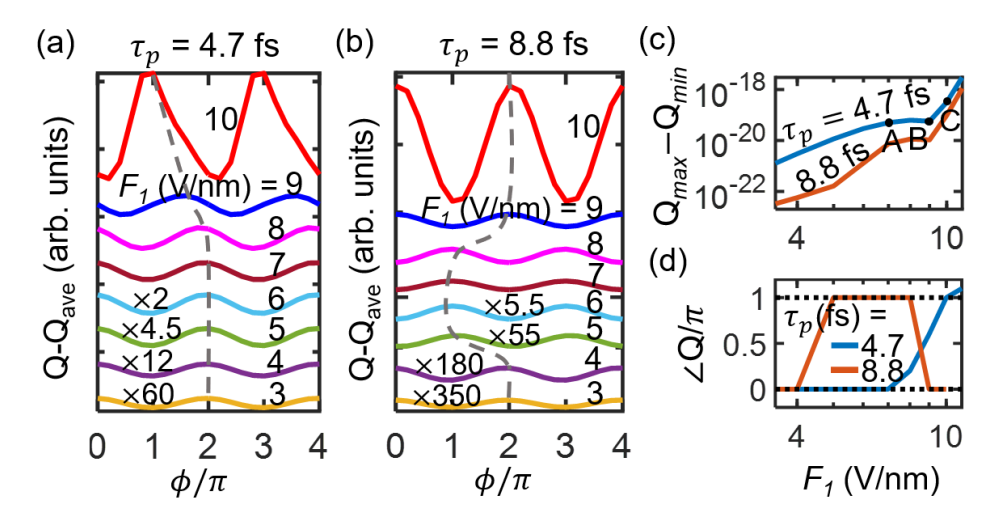


Figure 4.4: CEP sensitivity of total emission charge density Q under different laser fields  $F_1$ . (a),(b) Difference between Q and its averaged value  $Q_{ave}$  as a function of  $\phi$  for different  $F_1$  with pulse duration (a)  $\tau_p = 4.7$  fs and (b)  $\tau_p = 8.8$  fs. For a given  $F_1$ ,  $Q_{ave} = (Q_{max} + Q_{min})/2$ . Dashed lines indicate the shift of the phase for the CEP modulation. (c) Difference between the maximum and minimum values of charge  $Q_{max}$ - $Q_{min}$  in the curves of (a) and (b), as a function  $F_1$  for different  $\tau_p$ . Points A, B and C denote  $F_1 = 7$ , 9, and 10 V/nm, respectively. (d) Photoemission charge phase  $\angle Q$  as a function of  $F_1$  for different  $\tau_p$ .  $\angle Q$  is obtained by using  $B\cos(\phi+\angle Q)$  to fit the curves in (a) and (b), with  $B = Q_{max}$ - $Q_{min}$ .

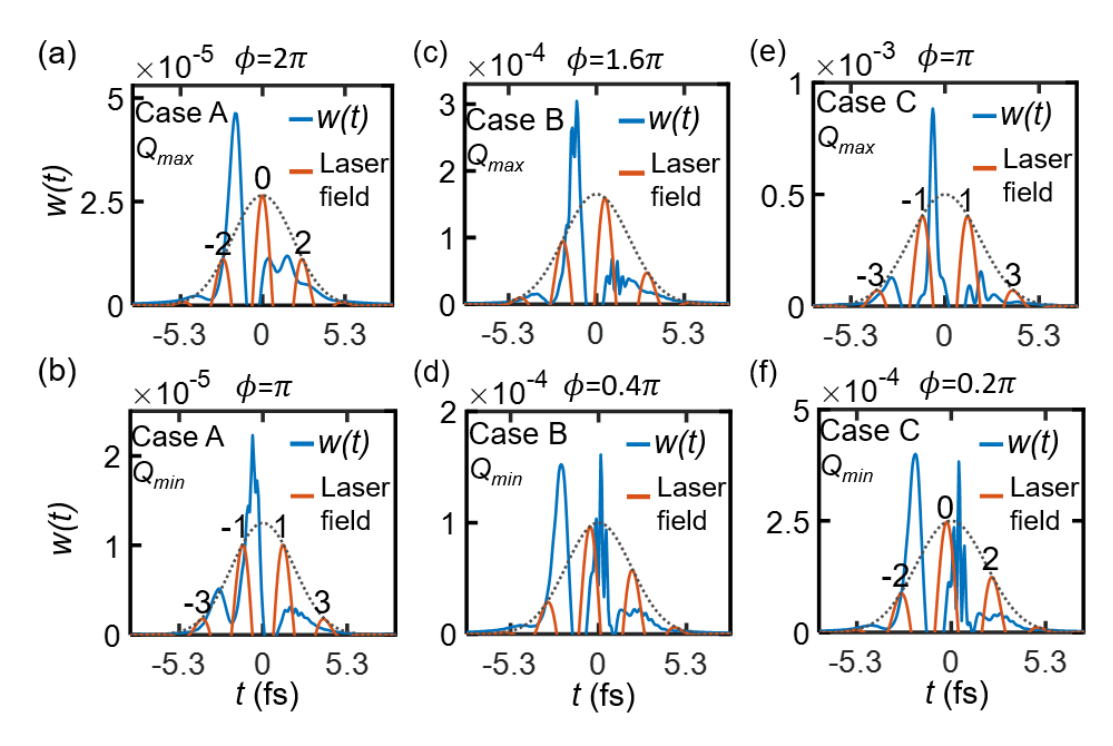


Figure 4.5: Time-dependent emission current density w(t) at the surface ( $\bar{x} = 0$ , with surface oscillatory current excluded) as a function of time t for pulse duration  $\tau_p = 4.7$  fs at CEP  $\phi$  when  $Q_{max}$  (top row) or  $Q_{min}$  (bottom row) occurs, under different laser fields at (a),(b)  $F_1 = 7$  V/nm; (c),(d)  $F_1 = 9$  V/nm; and (e),(f)  $F_1 = 10$  V/nm. The values of laser field  $F_1$  correspond to case A, B and C in Figure 4.4(c), respectively. The value of CEP  $\phi$  in each panel corresponds to the occurrence of  $Q_{max}$  (top row) or  $Q_{min}$  (bottom row) in Figure 4.4(a). The blue lines are for emission current density, red lines for laser field, and black dotted lines for laser pulse envelope. The optical half cycles of the laser field in (a), (b), (e), (f) are numbered as  $0, \pm 1, \pm 2$  and  $\pm 3$ , with "0" being the center cycle with the highest peak. Only positive optical half cycles are shown.

To uncover the physical origin of the vanishing CEP sensitivity behavior and the CEP phase shift in the photoemission charge, we plot the time-dependent electron emission current density w(t) at the surface ( $\bar{x}=0$ ) as a function of time, under different laser fields  $F_1$  and CEP  $\phi$  for  $\tau_p=4.7$  fs, as shown in Figure 4.5. The laser field strengths of 7, 9, and 10 V/nm used in Figure 4.5 correspond to cases A, B and C in Figure 4.4(c), respectively. By observing these time-dependent current pulses, it is clear that electron emission starts at the beginning of each positive half cycle in a given laser field pulse. When  $F_1=7$  V/nm (case A before the dip in CEP sensitivity in Figure 4.4(c)), even-numbered positive optical half cycles (Figure 4.5(a)) drive more photoelectron emission than odd-numbered positive optical half cycles (Figure 4.5(b)). However, as the laser

field  $F_1$  is increased to 10 V/nm (case C after the dip in CEP sensitivity in Figure 4.4(c)), odd-numbered positive half cycles trigger more electron emission than even-numbered cycles (cf. Figures. 4.5(e) and 4.5(f)). This indicates in the strong field regime, there exists a competition between even and odd positive half-cycle contributions to photoelectron emission, and thus a  $\pi$  phase shift in  $\phi$  as shown in Figure 4.4(d), with varying CEP. At  $F_1 = 9$  V/nm (case B at the dip in CEP sensitivity in Figure 4.4(c)),  $Q_{\text{max}}$ - $Q_{\text{min}}$  becomes minimal, where  $Q_{\text{max}}$  and  $Q_{\text{min}}$  occur at  $\phi = 1.6\pi$  and  $0.4\pi$ , respectively. The competition between electron emission from neighboring positive optical half cycles also leads to the dips in CEP sensitivity and phase shifts at  $F_1 = 5$  V/nm and 9 V/nm for  $\tau_p = 8.8$  fs in Figures 4.4(c) and 4.4(d).

It is important to note that, for clarity, we plot in Figure 4.5 only the emitted current density that eventually escapes from the surface, whereas the local strong oscillatory current density near the surface typically associated with photoemission (e.g. see Figures 4.6(a) and 4.6(b) below, and also References [6][61][62][76][109][110]) is filtered out. This is possible in our exact analytical calculation using Equation (39), by excluding the high *n*-order (and *l*-order) terms, which is verified to give the strong oscillatory surface currents only. This is also consistent with previous study that the high energy regime in the photoelectron spectra is due to surface oscillations and rescattering (cf. Figure 4 in Reference [109]).

It is also noteworthy that, though electron emission starts at the beginning of every positive optical half cycles in the laser pulse, there is typically a time delay between the peak of the positive optical half cycle and the peak of the emission current pulse, as seen in Figure 4.5. Furthermore, a stronger positive optical half cycle does not necessarily lead to a higher current pulse emission, which, however, depends strongly on the emission from neighboring half cycles in a laser pulse. These observations indicate that further examination is needed on the validity of the widely used

Fowler-Nordheim rate equations, in which current emission follows closely the optical positive half cycles, to study the CEP sensitive, time-dependent strong-field photoemission [55].

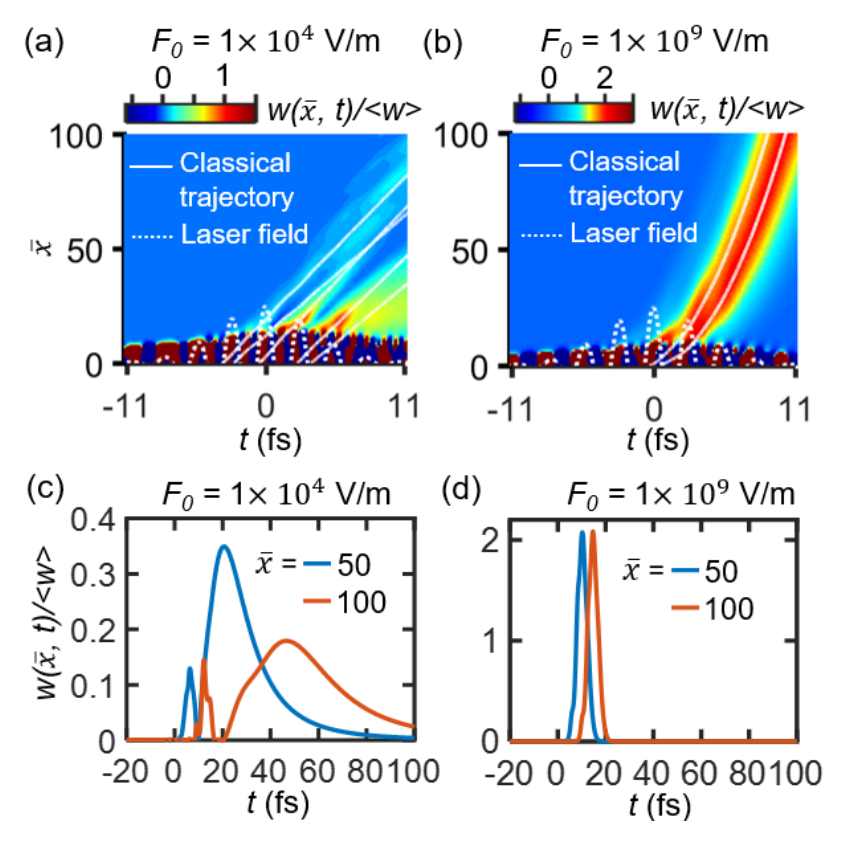


Figure 4.6: Total time-dependent emission current density  $w(\bar{x}, t)$  under the dc field  $F_0 = 1 \times 10^4$  V/m and  $1 \times 10^9$  V/m. (a),(b)  $w(\bar{x}, t)$  including surface oscillation currents as a function of the space  $\bar{x}$  and time t. Solid white lines show the corresponding classical trajectories. Dotted white lines show the positive half cycles of the laser electric field. (c),(d) Emission current density w(t) at  $\bar{x} = 50$  and 100, as a function of time t. The time-dependent current in all figures is normalized in terms of the time-averaged emission current  $\langle w \rangle$ . Here, the laser pulse duration  $\tau_p = 8.8$  fs and the peak laser field  $F_1 = 1$  V/nm. When  $F_0 = 1 \times 10^4$  V/m,  $\langle w \rangle = 2.5 \times 10^{-11}$ ; When  $F_0 = 1 \times 10^9$  V/m,  $\langle w \rangle = 2.1 \times 10^{-7}$ .

In Figure 4.6, we plot the total time-dependent photoemission current density  $w(\bar{x}, t)$ , including oscillatory surface currents, as a function of the space  $\bar{x}$  and time t under different dc bias. The strong oscillatory surface currents are confined to the very limited region near the surface only. It is found that increasing the dc field from  $F_0 = 1 \times 10^4$  V/m to  $1 \times 10^9$  V/m increases the time-averaged emission current density from  $\langle w \rangle = 2.5 \times 10^{-11}$  to  $2.1 \times 10^{-7}$ . More importantly, the

emission current pulse is significantly shortened (from 19.7 fs to 4.8 fs of FWHM at  $\bar{x} = 50$ ). Also, due to the strong acceleration of the larger  $F_0$ , the shape of the pulse is retained (without consideration of space charge effect) as the current pulse travels further from the surface (see Figure 4.6(d)). This may provide a practical way to shorten the photoemission current pulse by simply adding a large dc bias. The solid white lines are the corresponding classical trajectories [76], showing good agreement with the electron dynamics from our quantum model. Note because of the relatively small optical field used, the trajectories of the emitted photoelectrons in Figure 4.6(a) show fewer oscillatory features compared to those cases with strong laser fields (cf. Figure 3 of Reference [110]). This is due to the weaker backpropagation and acceleration processes of emitted electrons (i.e., smaller quiver motion) under weak laser electric fields. When adding a strong dc bias, most of electrons are able to escape from the metal surface with negligible quiver motion, as shown in Figure 4.6(b), similar to the DC field emission process. The classical trajectories in Figures 4.6(a) and 4.6(b) suggest that, in Figure 6(c), the narrow current peak is due to electron emission by the left-to-center and the center positive optical half cycles, and the broad peak is driven by the right-to-center positive optical half cycle. In Figure 4.6(d), the single dominant current peak is mainly driven by the center positive optical half cycle of the laser field under strong dc bias.

### 4.4 Conclusion

In this chapter, we present a quantum analytical solution for few-cycle photoelectron emission from a dc-biased surface induced by Gaussian laser pulses, by solving the TDSE. Our exact model is valid for arbitrary pulse length from sub-cycle to CW excitation, and for arbitrary pulse repetition rate. Our calculations show the emitted charge per pulse oscillatorily increases as the laser pulse separation decreases due to varying coherence interaction of neighboring laser pulses.

Our results recover the experimentally measured features of sinusoidal CEP modulation to photoelectron emission and varnishing CEP sensitivity with a  $\pi$  phase shift in optical-field regime under strong optical fields. Moreover, we find adding a large dc field greatly enhances the photoelectron current and shortens the current pulse.

#### **CHAPTER 5**

### PHOTOELECTRON EMISSION IN A NANOSCALE GAP

#### 5.1 Introduction

Due to the promise for potential applications to ultrafast and highly sensitive photodetection in the room temperature, laser-driven electron emission in the nanometer-scale two-tip junctions has drawn strong recent interests [17][20][23][63]–[66][111]. Rybka et al. [17] reported laser-induced sub-femtosecond photoelectron tunneling in a nanoscale metal-vacuum-metal gap. Higuchi et al. [63] explored the rectification effect of dc-biased two-metal-nanotip junction in ultrafast multiphoton photoemission. Ludwig et al. [23] presented the strong dependence of dynamics of nanoscale electron transport between two metal tips on the temporal profile of driving laser pulses. Turchetti et al. [66] studied the impact of dc bias on photoemission from metal surfaces surrounding a nano-vacuum gap. Typically, numerical solutions of the time-dependent density function theory [23][64][65][112][113] and Schrödinger equation [66][114] are implemented to study the photoemission properties in nanoscale gaps, but the underlying physics for the interplays between electron emission process, laser field, gap size and materials is not always transparent, especially when transitioning among different emission regimes.

In this chapter, by exactly solving the TDSE, we present analytical models for nonlinear ultrafast electron emission and dynamics in a nanoscale metal-vacuum-metal junction without and with dc bias driven by a single-frequency laser field. Using the analytical formulation, we investigate the photoelectron transport with various gap distances, laser intensities, wavelengths, dc bias and metal materials. Our results provide clear insights to the energy distribution of emitted photoelectron and spatiotemporal emission dynamics inside the metal-vacuum-metal junction. Part

of the material of this chapter is submitted to Optics Letters and another journal article is also planned.

## **5.2 Photoelectron Transport without DC Bias**

## 5.2.1 Analytical Model

Our one-dimensional (1D) model (see Figure 5.1) considers electrons with initial energy  $\varepsilon$  emitted from the surface at x = 0, under the action of laser field  $F_1\cos(\omega t)$ , where  $F_1$  is the amplitude of the laser field and  $\omega$  is the angular frequency. The laser field is assumed to be perpendicular to the flat emitter surface, and cuts off abruptly at the surface [6][66], thus the time-dependent potential energy in the entire regime reads [6][61][62][74][106],

$$\Phi(x,t) = \begin{cases} 0 & x < 0 \\ E_F + W - eF_1x\cos(\omega t) & 0 \le x < d \\ -eF_1d\cos(\omega t) & x \ge d, \end{cases}$$
(43)

where  $E_F$  and W are the Fermi energy and work function of the left metal respectively, and e is the elementary charge.

By solving the TDSE subjected to the potential energy given in Equation (43), the electron wave function for x < 0 is found to be,

$$\psi(x,t) = \exp\left(-\frac{i\varepsilon t}{\hbar} + ik_0 x\right) + \sum_{n=-\infty}^{\infty} R_n \exp\left(-i\frac{\varepsilon + n\hbar\omega}{\hbar}t - ik_n x\right), x < 0$$
 (44)

which denotes the superposition of an incident plane wave with initial energy  $\varepsilon$  and a set of reflected plane waves with reflection coefficient  $R_n$  and energies  $\varepsilon + n\hbar\omega$ , where the wavenumber  $k_0 = \sqrt{2m_e\varepsilon/\hbar^2}$  and  $k_n = \sqrt{2m_e(\varepsilon + n\hbar\omega)/\hbar^2}$ .

For  $0 \le x < d$  (in the gap), the exact solution of electron wave function is (see Appendix D for the method),

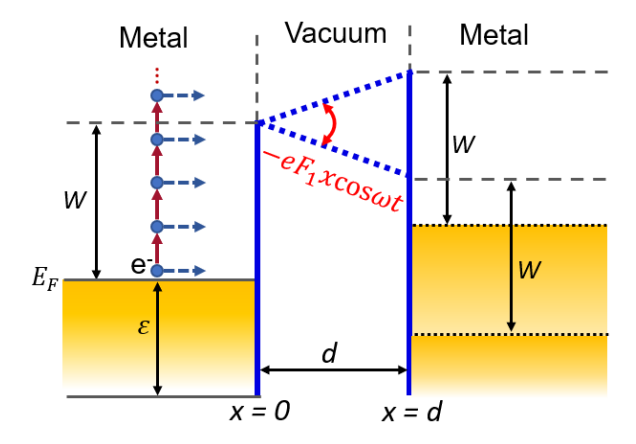


Figure 5.1: Energy diagram for photoelectron emission in a nanoscale metal-vacuum-metal junction under a single-frequency laser field. Electrons with the initial energy  $\varepsilon$  are emitted from the surface at x = 0, with an energy of  $\varepsilon + n\hbar\omega$ , due to n-photon contribution. Here, by symmetry, electron emission from the surface at x = d can be modeled in the same way (but with an opposite sign of instantaneous laser field).

$$\psi(x,t) = \sum_{n=-\infty}^{\infty} \exp\left[-i\frac{\varepsilon + n\hbar\omega}{\hbar}t\right] \exp\left[\frac{ixeF_1\sin(\omega t)}{\hbar\omega} + \frac{ie^2F_1^2\sin(2\omega t)}{8m_e\hbar\omega^3}\right] \times \left\{T_{1n}\exp\left[i\sqrt{\frac{2m_eE_n}{\hbar^2}}\left(x + \frac{eF_1\cos(\omega t)}{m_e\omega^2}\right)\right] + T_{2n}\exp\left[-i\sqrt{\frac{2m_eE_n}{\hbar^2}}\left(x + \frac{eF_1\cos(\omega t)}{m_e\omega^2}\right)\right]\right\}, \ 0 \le x < d \ (45)$$

which shows the superposition of a set of electron waves travelling towards +x direction with coefficient  $T_{1n}$  and towards -x direction with coefficient  $T_{2n}$  inside the gap, where the drift kinetic energy  $E_n = \varepsilon + n\hbar\omega - E_F - W - U_p$ , and the ponderomotive energy  $U_p = e^2 F_1^2 / 4m_e \omega^2$ .

For  $x \ge d$ , an exact solution of electron wave function is easily obtained,

$$\psi(x,t) = \sum_{n=-\infty}^{\infty} T_{3n} \exp\left(-i\frac{\varepsilon + n\hbar\omega}{\hbar}t\right) \exp\left[ik_n x + i\frac{eF_1 d\sin(\omega t)}{\hbar\omega}\right], x \ge d \qquad (46)$$

which represents the superposition of transmitted electron plane waves with energies  $\varepsilon + n\hbar\omega$ , due to multiphoton absorption (n>0), direct tunneling (n=0) and multiphoton emission (n<0) [6][76], where the wavenumber  $k_n = \sqrt{2m_e(\varepsilon + n\hbar\omega)/\hbar^2}$  and  $T_{3n}$  is the transmission coefficient.

By imposing the boundary conditions that both the electron wave function  $\psi(x,t)$  and its derivative  $\partial \psi(x,t)/\partial x$  are continuous at x=0 and x=d, and taking Fourier transform, we obtain, in nondimensional quantities [6][61][62],  $\bar{\varepsilon}=\varepsilon/W$ ,  $\bar{\omega}=\omega\hbar/W$ ,  $\bar{t}=tW/\hbar$ ,  $\bar{E}_F=E_F/W$ ,  $\bar{x}=x/\lambda_0$ ,  $\bar{t}=x/\lambda_0$ ,  $\bar{t}=x$ 

$$\sum_{n=-\infty}^{\infty} T_{1n} \left[ \sqrt{\overline{\varepsilon} + m\overline{\omega}} P_{1n(n-m)} + Q_{1n(n-m)} \right] + T_{2n} \left[ \sqrt{\overline{\varepsilon} + m\overline{\omega}} P_{2n(n-m)} + Q_{2n(n-m)} \right]$$

$$= 2\sqrt{\overline{\varepsilon}} \delta(m)$$
(47)

$$\sum_{n=-\infty}^{\infty} \left[ \sqrt{\bar{\varepsilon} + m\bar{\omega}} U_{1n(n-m)} - V_{1n(n-m)} \right] T_{1n} + \left[ \sqrt{\bar{\varepsilon} + m\bar{\omega}} U_{2n(n-m)} - V_{2n(n-m)} \right] T_{2n} = 0$$
 (48)

$$\sum_{n=-\infty}^{\infty} T_{1n} U_{1n(n-m)} + T_{2n} U_{2n(n-m)} = T_{3m} \exp\left(i\bar{d}\sqrt{\bar{\varepsilon} + m\bar{\omega}}\right)$$
 (49)

where  $\delta(m)$ ,  $P_{1n(n-m)}$ ,  $Q_{1n(n-m)}$ ,  $P_{2n(n-m)}$ ,  $Q_{2n(n-m)}$ ,  $U_{1n(n-m)}$ ,  $V_{1n(n-l)}$ ,  $U_{2n(n-m)}$ , and  $V_{2n(n-l)}$  are given by,

$$\delta(m) = \begin{cases} 1, & m = 0, \\ 0, & m \neq 0, \end{cases}$$
 (50a)

$$P_{1nl} = \frac{1}{2\pi} \int_0^{2\pi} p_{1n}(\overline{\omega}\overline{t}) e^{-il\overline{\omega}\overline{t}} d(\overline{\omega}\overline{t}), \quad Q_{1nl} = \frac{1}{2\pi} \int_0^{2\pi} q_{1n}(\overline{\omega}\overline{t}) e^{-il\overline{\omega}\overline{t}} d(\overline{\omega}\overline{t}), \quad (50b)$$

$$P_{2nl} = \frac{1}{2\pi} \int_0^{2\pi} p_{2n}(\overline{\omega}\overline{t}) e^{-il\overline{\omega}\overline{t}} d(\overline{\omega}\overline{t}), \quad Q_{2nl} = \frac{1}{2\pi} \int_0^{2\pi} q_{2n}(\overline{\omega}\overline{t}) e^{-il\overline{\omega}\overline{t}} d(\overline{\omega}\overline{t}), \quad (50c)$$

$$p_{1n}(\bar{\omega}\bar{t}) = e^{i\frac{2\sqrt{\bar{E}_n}\bar{F}_1}{\bar{\omega}^2}\cos(\bar{\omega}\bar{t})}f(\bar{\omega}\bar{t}), \tag{50d}$$

$$q_{1n}(\bar{\omega}\bar{t}) = \left[\sqrt{\bar{E}_n} + \frac{\bar{F}_1}{\bar{\omega}}\sin(\bar{\omega}\bar{t})\right] p_{1n}(\bar{\omega}\bar{t}), \tag{50e}$$

$$p_{2n}(\bar{\omega}\bar{t}) = e^{-i\frac{2\sqrt{\bar{E}_n}\bar{F}_1}{\bar{\omega}^2}\cos(\bar{\omega}\bar{t})}f(\bar{\omega}\bar{t}), \qquad (50f)$$

$$q_{2n}(\overline{\omega}\overline{t}) = \left[\frac{\overline{F}_1}{\overline{\omega}}\sin(\overline{\omega}\overline{t}) - \sqrt{\overline{E}_n}\right] p_{2n}(\overline{\omega}\overline{t}), \tag{50g}$$

$$f(\bar{\omega}\bar{t}) = e^{i\frac{\bar{F}_1^2}{4\bar{\omega}^3}\sin(2\bar{\omega}\bar{t})},$$
(50h)

$$U_{1nl} = P_{1nl} e^{i\sqrt{\overline{E}_n} \, \bar{d}}, \qquad V_{1nl} = Q_{1nl} e^{i\sqrt{\overline{E}_n} \, \bar{d}},$$
 (50*i*)

$$U_{2nl} = P_{2nl} e^{-i\sqrt{\bar{E}_n}\,\bar{d}}, \quad V_{2nl} = Q_{2nl} e^{-i\sqrt{\bar{E}_n}\,\bar{d}},$$
 (50j)

with  $\bar{E}_n = \bar{\varepsilon} + n\bar{\omega} - \bar{E}_F - \bar{U}_p - 1$ . The coefficients  $T_{1n}$ ,  $T_{2n}$ , and  $T_{3n}$  (and therefore  $R_n$ ) is then calculated from Equations (47), (48) and (49).

The normalized transmitted current density is defined as the ratio of the transmitted probability current density over the incident probability current density,  $w(\varepsilon, x, t) = J_t(\varepsilon, x, t)/J_i(\varepsilon, x, t)$ , where the probability current density  $j(x,t) = (i\hbar/2m_e)(\psi\nabla\psi^* - \psi^*\nabla\psi) = (i\hbar/2m_e)\sum_{n=-\infty}^{\infty}\sum_{l=-\infty}^{\infty}(\psi_n\nabla\psi_l^* - \psi_n^*\nabla\psi_l)$ . Thus, the normalized instantaneous current density inside the gap (0 < x < d) is,

$$w(\bar{\varepsilon}, \bar{x}, \bar{t}) = \frac{1}{\sqrt{\bar{\varepsilon}}} \sum_{n=-\infty}^{\infty} \sum_{l=-\infty}^{\infty} Re \left\{ e^{i(l-n)\bar{\omega}\bar{t}} \times \left\{ T_{1n} T_{1l}^* D_1 + T_{1n} T_{2l}^* D_2 + T_{2n} T_{1l}^* D_3 + T_{2n} T_{2l}^* D_4 \right\} \right\}$$
(51)

where 
$$D1 = \exp\left[i\left(\sqrt{\overline{E}_n} - \left(\sqrt{\overline{E}_l}\right)^*\right)\left(\bar{x} + \frac{2\bar{F}_1\cos(\bar{\omega}\bar{t})}{\bar{\omega}^2}\right)\right]\left[\left(\sqrt{\overline{E}_l}\right)^* + \frac{\bar{F}_1\sin(\bar{\omega}\bar{t})}{\bar{\omega}}\right]$$
,  $D2 = \exp\left[i\left(\sqrt{\overline{E}_n} + \left(\sqrt{\overline{E}_l}\right)^*\right)\left(\bar{x} + \frac{2\bar{F}_1\cos(\bar{\omega}\bar{t})}{\bar{\omega}^2}\right)\right]\left[\left(\sqrt{\overline{E}_l}\right)^* - \frac{\bar{F}_1\sin(\bar{\omega}\bar{t})}{\bar{\omega}}\right]$ ,  $D3 = \exp\left[-i\left(\sqrt{\overline{E}_n} + \left(\sqrt{\overline{E}_l}\right)^*\right)\left(\bar{x} + \frac{2\bar{F}_1\cos(\bar{\omega}\bar{t})}{\bar{\omega}^2}\right)\right]\left[\left(\sqrt{\overline{E}_l}\right)^* + \frac{\bar{F}_1\sin(\bar{\omega}\bar{t})}{\bar{\omega}}\right]$ , and  $D4 = -\exp\left[i\left(\left(\sqrt{\overline{E}_l}\right)^* - \sqrt{\overline{E}_n}\right)\left(\bar{x} + \frac{2\bar{F}_1\cos(\bar{\omega}\bar{t})}{\bar{\omega}^2}\right)\right]\left[\left(\sqrt{\overline{E}_l}\right)^* - \frac{\bar{F}_1\sin(\bar{\omega}\bar{t})}{\bar{\omega}}\right]$ . The corresponding time-averaged emission current density is

$$\langle w(\bar{\varepsilon}) \rangle = \frac{1}{2\pi} \int_0^{2\pi} w(\bar{\varepsilon}, \bar{x}, \bar{t}) d(\bar{\omega}\bar{t}). \tag{52}$$

In the metal on the right-hand side (x > d), the normalized instantaneous transmitted current density is found as,

obtained from the numerical integration of Equation (52) over time,

$$w(\bar{\varepsilon}, \bar{x}, \bar{t}) = \frac{1}{\sqrt{\bar{\varepsilon}}} \sum_{n=-\infty}^{\infty} \sum_{l=-\infty}^{\infty} Re\{e^{i(l-n)\bar{\omega}\bar{t}} T_{3n} T_{3l}^* D\},$$
 (53)

where  $D=\mathrm{e}^{i\,[\sqrt{\overline{\varepsilon}+n\overline{\omega}}-(\sqrt{\overline{\varepsilon}+l\overline{\omega}})^*]\bar{x}}(\sqrt{\overline{\varepsilon}+l\overline{\omega}})^*$ . The time-averaged transmitted current density is,

$$\langle w(\bar{\varepsilon}) \rangle = \sum_{n=-\infty}^{\infty} \langle w_n(\bar{\varepsilon}) \rangle, \quad \langle w_n(\bar{\varepsilon}) \rangle = \text{Re}(|T_{3n}|^2 \sqrt{1 + n\overline{\omega}/\bar{\varepsilon}}), \tag{54}$$

where  $\langle w_n \rangle$  represents the time-averaged transmitted current density through *n*-photon process, with transmitted electrons of energy  $\varepsilon + n\hbar\omega$  [6,76]. Due to current continuity, the time-averaged current density obtained from Equation (52) and Equation (54) are equal, which has been verified in our calculations.

### 5.2.2 Results and Discussion

Using the analytical solution presented above, we analyze the photoelectron emission properties under different combinations of gap distances and laser fields. Unless mentioned otherwise, the default value of the laser wavelength is 800 nm ( $\hbar\omega=1.55~{\rm eV}$ ), the metals on both sides of the gap are assumed to be gold [17][20][65][111], with Fermi energy  $E_F=5.53~{\rm eV}$  and work function  $W=5.1~{\rm eV}$ , and the photoemission current is calculated from Equation (54). Since most of the electrons are emitted with initial energies near the Fermi level [6][76][86][87], we choose the electron initial energy  $\varepsilon=E_F$  for simplicity.

Figure 5.2(a) shows the dependence of total time-averaged transmitted current density  $\langle w \rangle$  on the gap distance d under different laser fields  $F_1$ . When the laser field is off (i.e.,  $F_1 = 0$ ), the current  $\langle w \rangle$  is contributed only by direct tunneling, which rapidly decreases as gap distance increases. After applying a laser field, the current  $\langle w \rangle$  decreases initially as d increases, closely following the scaling for the case of  $F_1 = 0$ , where direct tunneling dominates. As d increases further, for a given laser field, the current  $\langle w \rangle$  oscillates around a constant value (cf. the dashed

lines), which is found to be the photoemission current from a single metal surface (i.e., when the metal on the right-hand side in Figure 5.1 is removed). The oscillation behavior is attributed to the interference of electron waves inside the gap due to reflections from the metal-vacuum interfaces, for various gap distances d. Here, we ignore the effects of image charge and space charge, thus the oscillation amplitude of  $\langle w \rangle$  remains almost unchanged with increasing d. This oscillation behavior is similar to that found in field emission from dielectric coated surfaces [115][116]. The quantum interference of electron waves is also demonstrated experimentally in Reference [13], where the distinct peaks in energy spectra arise from the interference of electron waves rescattering at the emitter tip. Figure 5.2(b) shows the energy spectra for photoelectrons transmitted into the right-side metal for different gap distances d and laser fields  $F_1$ . It can be seen that for a smaller laser field ( $F_1 = 1 \text{ V/nm}$ ), as d decreases, the dominant emission shifts from four-photon

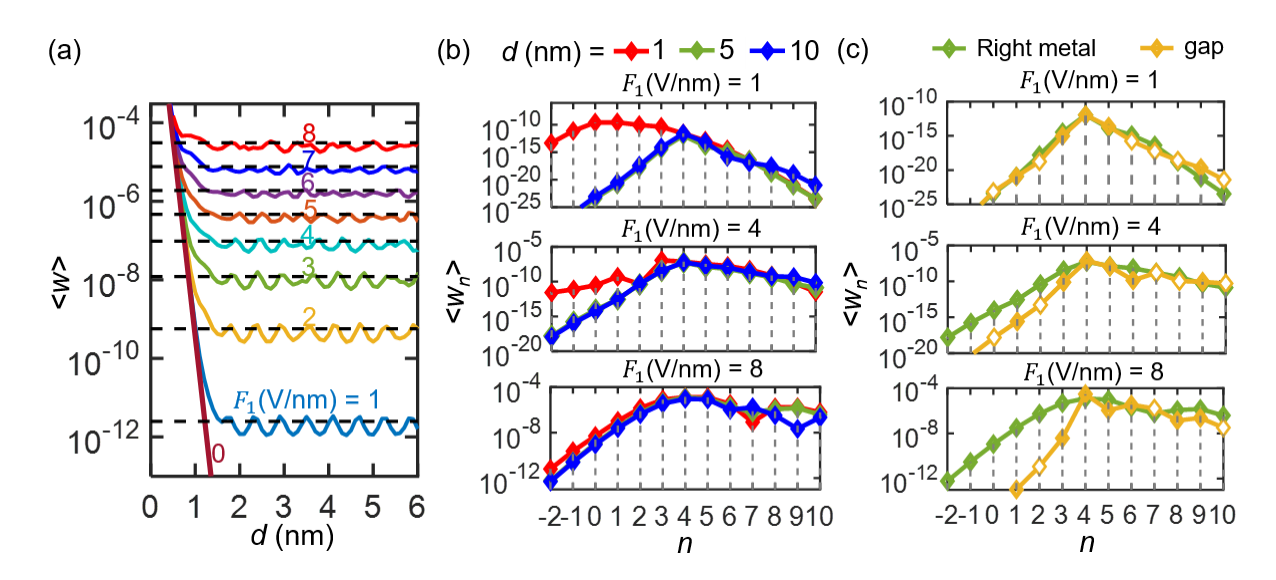


Figure 5.2: Normalized time-averaged photoemission current density under various gap sizes and laser fields. (a) Total emission current density  $\langle w \rangle$  as a function of gap distance d for different laser fields  $F_1$ . Dashed lines denote the emission current density from a single surface when the metal on the right-hand side in Figure 5.1 is removed, which is obtained from Reference [6]. (b) Energy spectra for photoelectrons transmitted into the metal on the right-hand side for different d and d an

over-barrier emission (n = 4, cf. the ratio of metal work function over single photon energy  $W/\hbar\omega \approx 3.29$ ) to tunneling emission (n < 4). As laser field increases ( $F_1 = 4$  V/nm and 8 V/nm), this shift of the dominant emission process becomes less prominent, because the potential barrier inside the gap becomes less sensitive to the gap distance d under strong laser fields.

Figure 5.2(c) compares the energy spectra for photoelectrons inside the gap and in the right-side metal for d = 2 nm. It is found that although the total emission current  $\langle w \rangle$  is equal in these two regions, the energy distribution of photoelectrons is quite different. In particular, the time-averaged current densities for all n-photon channels are positive in the right-side metal, while some of them are negative inside the gap (see the open diamond markers in Figure 5.2(c)). Negative value of  $\langle w_n \rangle$  means electrons excited through those n-photon processes are reflected backwards inside the gap. Additionally, n-photon processes with n < 4 contribute more significantly for transmitted electrons in the right-side metal than those inside the gap, which becomes more pronounced for larger laser intensity.

In Figure 5.3(a), we plot the total time-averaged emission current density  $\langle w \rangle$  as a function of laser field  $F_1$  with various gap distances d. For the vacuum gap with  $d \le 1$  nm, the slope of  $\langle w \rangle$  increases with  $F_1$ , indicating the dominant emission process shifts to higher order n-photon absorption. This is consistent with the results shown in Figure 5.2(b). For the cases with larger gap distances, the slope of  $\langle w \rangle$  becomes insensitive to the gap distance d and follows that of photoemission current from a single metal surface. The scale approaches  $\langle w \rangle \propto F_1^{2n}$  with n=4, indicating four-photon absorption dominates the emission process. Figure 5.3(b) displays the difference between the total emission current in a nanogap and emission current from a single surface  $\langle w \rangle - \langle w \rangle_{SS}$ , where the difference becomes more pronounced in the larger laser intensity regime. Besides, it is interesting to find that the location of channel-closing-induced drop of

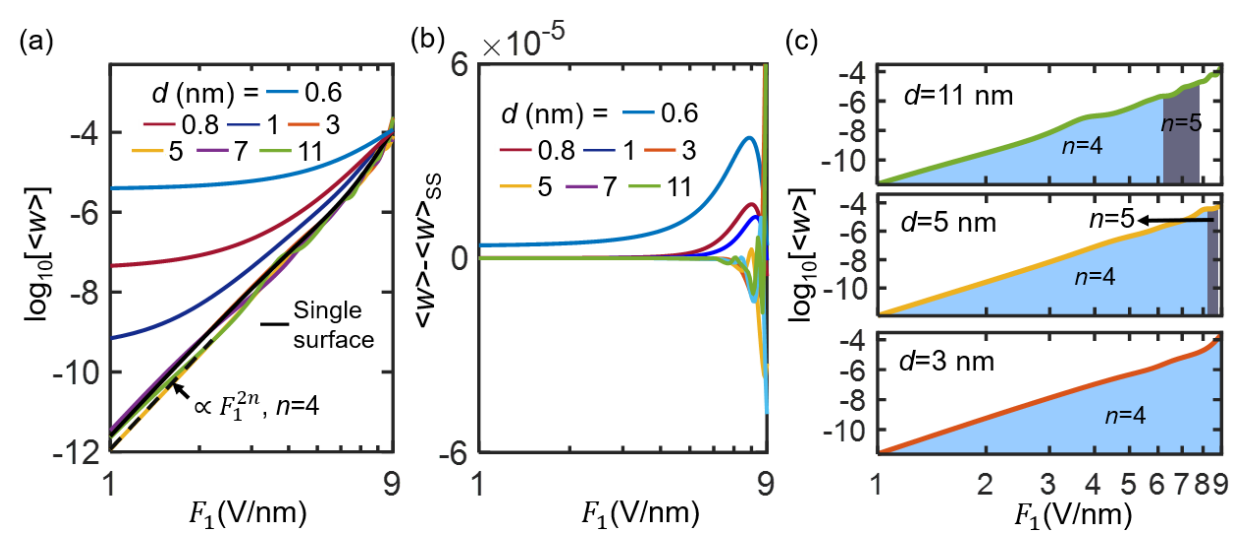


Figure 5.3: (a) Normalized total time-averaged emission current density  $\langle w \rangle$  and (b) difference between total emission current  $\langle w \rangle$  and emission current from a single surface  $\langle w \rangle_{SS}$  as a function of laser field  $F_1$  for different gap distances d. The single surface case  $\langle w \rangle_{SS}$  is obtained from Reference [6]. The dashed line in (a) denotes the scale of  $\langle w \rangle \propto F_1^{2n}$  with n=4. (c) Emission current density  $\langle w \rangle$  as a function of laser field  $F_1$  for gap spacing d=3, 5, and 11 nm. Here, laser field regimes are labeled with n=4 and n=5 (cf. the areas filled with different colors), which means the dominant emission process in this field regime is four- or five-photon absorption.

emission current density  $\langle w \rangle$  (i.e., the location of transition between the dominant four- and fivephoton absorption in Figure 5.3(c), determined by observing the shift of the peak of the emitted electron energy spectra) shifts to larger laser field  $F_1$  for smaller gap distance d. This indicates that decreasing the gap distance (before entering the direct tunneling regime) can extend the multiphoton regime to higher laser intensity. This may be explained by the fact that the shape of the potential barrier becomes less sensitive to the laser field strength for a smaller gap distance, thus allowing the dominant n-photon process to remain over a larger range of laser fields (or laser intensities).

Figure 5.4 shows the time-dependent current density w(x, t) as a function of space x and time t for different combinations of laser field  $F_1$  and gap distance d. It is seen that, besides the surface oscillation current near the metal-vacuum interface at x = 0, some electrons are back reflected from the vacuum-metal interface at x = d into the vacuum gap approximately at the beginning of

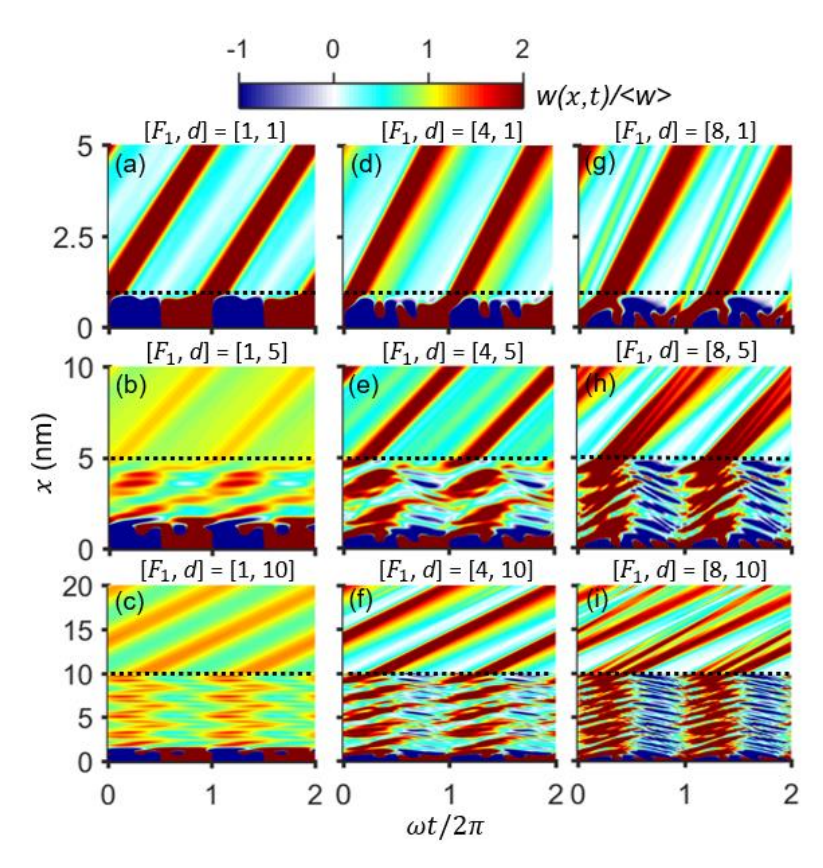


Figure 5.4: Total time-dependent current density w(x, t) as a function of time t and space x, under various laser fields  $F_1$  and gap distances d. Here, the time-dependent current density w(x, t) is normalized in terms of the time-averaged current density  $\langle w \rangle$ . In all figures, the units of  $F_1$  and d are V/nm and nm, respectively. The dotted lines show the position of x = d.

second half cycle of the laser fields (i.e.,  $\omega t = \pi$ ). This is shown by the change of w(x,t) from red to dark blue around  $\omega t = \pi$  in Figures 5.4(e), 5.4(f), 5.4(h) and 5.4(i), where the red region denotes positive current density propagates in the +x direction and the dark blue region in -x direction. As the gap distance d increases, more interference patterns of current density w(x,t) inside the gap are formed. The full width at half maximum (FWHM) of the emission current pulse is about 0.63 fs, which is greatly shorter than laser period of 2.67 fs.

We examine the total emission current density  $\langle w \rangle$  as a function of gap distance d for different incident wavelengths in Figure 5.5(a) and for metals with various work functions in Figure 5.5(b). It is found that the oscillation amplitude of  $\langle w \rangle$  increases when the laser photon energy  $\hbar \omega$  ( $\propto 1/\lambda$ , with  $\lambda$  being the laser wavelength) becomes closer to the metal work function W, indicating

stronger interference of electron waves inside the gap when  $W/\hbar\omega \to 1$ . Figures 5.5(c) and 5.5(d) show the photoelectron energy spectra for different laser wavelengths in Figure 5.5(a) and for different metals in Figure 5.5(b) with d=2 nm, respectively. The shift of the dominant emission to larger n-photon process is due to the increasing ratio of  $W/\hbar\omega$ .

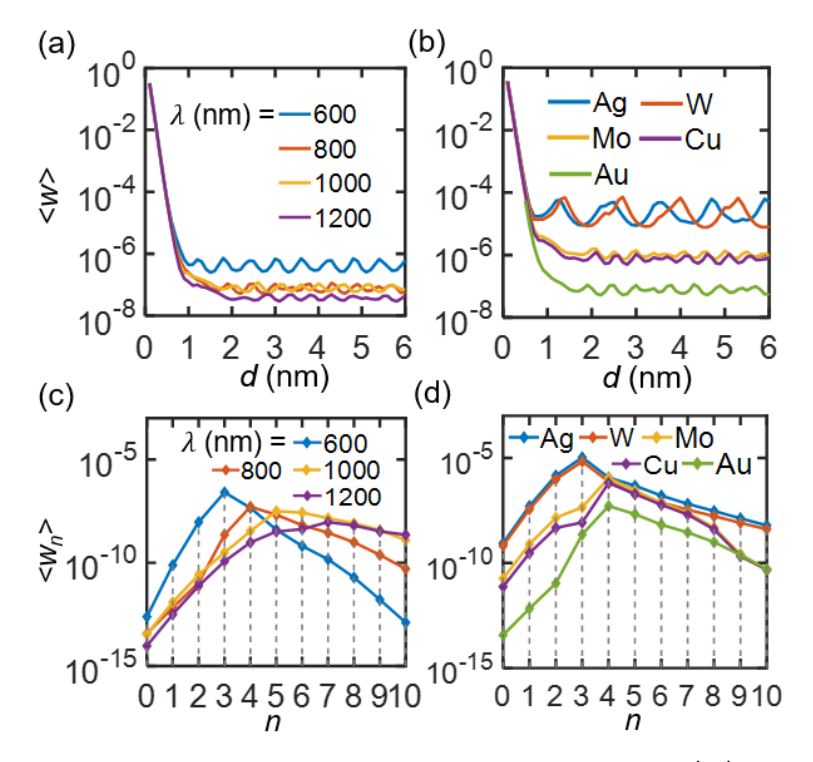


Figure 5.5: Normalized total time-averaged emission current density  $\langle w \rangle$  as a function of gap distance d for various (a) laser wavelengths and (b) metal materials. Photoelectron energy spectra for different (c) laser wavelengths and (d) metals, for d=2 nm. In (a) and (c), the metal is assumed to be gold. In (b) and (d), the incident wavelength is 800 nm. The work function of different materials is  $W_{\rm Ag} = 4.26$  eV [107],  $W_{\rm W} = 4.31$  eV [106],  $W_{\rm Mo} = 4.6$  eV [107],  $W_{\rm Cu} = 4.65$  eV [107], and  $W_{\rm Au} = 5.1$  eV [6][107]. The laser field  $F_1$  is fixed as 4 V/nm for all the cases.

## 5.2.3 Summary on Photoelectron Transport without DC Bias

In this section, we present an analytical solution for photoelectron emission and transport in a nanoscale metal-vacuum-metal junction driven by a single-frequency laser field, by exactly solving the time-dependent Schrödinger equation. The analytical model is valid for arbitrary gap distance, laser intensity, wavelength and metal work function and Fermi level. Our calculation exhibits the transition from direct tunneling to multiphoton induced electron emission and the

oscillatory dependence of photoemission current on the gap distance in the multiphoton regime. Our results demonstrate the energy redistribution of emitted photoelectrons across the two interfaces of the nanogap. We also find that decreasing the gap distance (but before transiting into the direct tunneling regime) can extend the multiphoton regime to higher laser intensity. The nonlinear effects of laser wavelength and materials on the gap-size dependence are examined.

## **5.3 Photoelectron Transport with DC Bias**

# **5.3.1** Analytical model

With the external applied dc voltage V shown in Figure 5.6(a), the symmetry of the metal-vacuummetal system is broken, which means under the same illumination condition, the left and right metal surfaces of the nanogap in Figure 5.6(a) have different photoemission properties. Therefore, we analytically model photoelectron emission from the left and right metal surfaces, respectively.

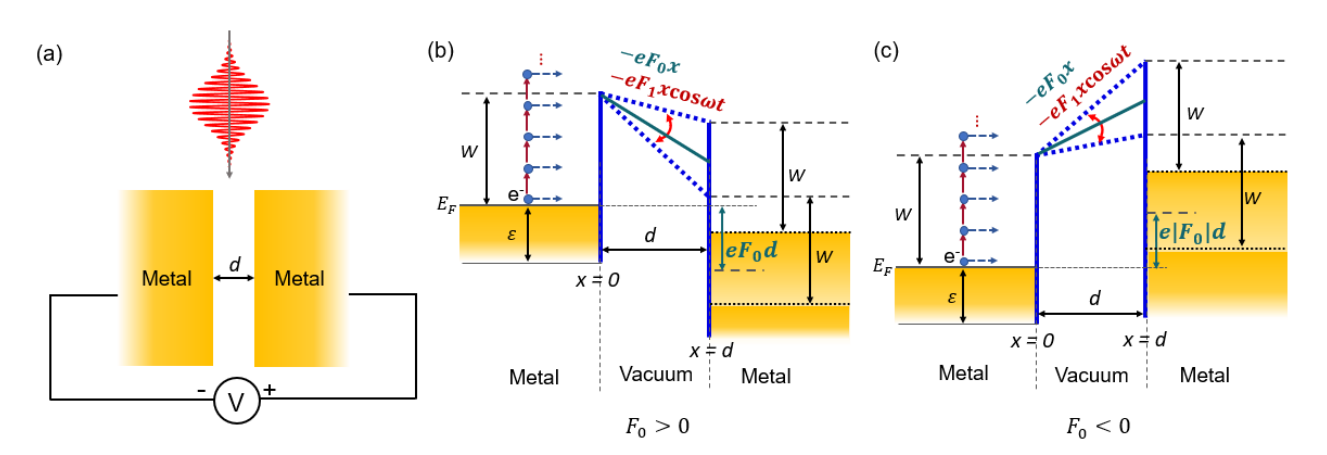


Figure 5.6: (a) Schematic of metal-vacuum-metal nanogap with a dc bias V under the illumination of laser field. d is the gap distance. (b) Energy diagram for photoelectron emission from left metal-vacuum interface of the gap in (a). Electrons with the initial energy  $\varepsilon$  would see a potential barrier subjected to a positive dc electric field  $F_0 = V/d$  (> 0) and laser field  $F_1\cos(\omega t)$ . (c) Energy diagram for photoelectron emission from right metal-vacuum interface of the gap in (a). Electrons would see a potential barrier with a negative dc electric field  $F_0 = -V/d$  (< 0) and laser field  $F_1\cos(\omega t)$  with  $F_1$  of opposite sign of that in (b) at any time instant for a given laser field.

For the photoemission from the left metal-vacuum interface of the nanogap in Figure 5.6(a), electrons with the initial energy  $\varepsilon$  would see a potential barrier subjected to a positive dc electric

field  $F_0 = V/d$  (> 0) and laser field  $F_1\cos(\omega t)$ , as shown in Figure 5.6(b). Thus, the time-dependent potential energy in the whole regime reads as [6][61][62][74][106],

$$\Phi(x,t) = \begin{cases} 0 & x < 0 \\ E_F + W - eVx/d - eF_1x\cos(\omega t) & 0 \le x < d \\ -eV - eF_1d\cos(\omega t) & x \ge d, \end{cases}$$
 (55)

where  $E_F$  and W are the Fermi energy and work function of the left-side metal in Figure 5.6(a) respectively, and V is the magnitude of the applied dc bias. Other parameters have the same definition as that in Equation (43).

By solving the TDSE with the potential energy given in Equation (55), the electron wave function for x < 0 is,

$$\psi(x,t) = \exp\left(-\frac{i\varepsilon t}{\hbar} + ik_0 x\right) + \sum_{n=-\infty}^{\infty} R_{1n} \exp\left(-i\frac{\varepsilon + n\hbar\omega}{\hbar}t - ik_n x\right), x < 0$$
 (56)

which denotes the superposition of an incident plane wave with initial energy  $\varepsilon$  and a set of reflected plane waves with reflection coefficient  $R_{1n}$  and energies  $\varepsilon + n\hbar\omega$ , where the wavenumber  $k_0 = \sqrt{2m_e\varepsilon/\hbar^2}$  and  $k_n = \sqrt{2m_e(\varepsilon + n\hbar\omega)/\hbar^2}$ .

For  $0 \le x < d$  (in the gap), the exact solution of electron wave function is found to be (see Appendix E for the method),

$$\psi(x,t) = \sum_{n=-\infty}^{\infty} \exp\left[-i\frac{\varepsilon + n\hbar\omega}{\hbar}t\right] \exp\left[-\frac{ie^{2}VF_{1}\sin(\omega t)}{\hbar dm_{e}\omega^{3}} + \frac{ixeF_{1}\sin(\omega t)}{\hbar\omega} + \frac{ie^{2}F_{1}^{2}\sin(2\omega t)}{8m_{e}\hbar\omega^{3}}\right] \times \left[T_{1n}Ai(-\eta_{n}) + T_{2n}Bi(-\eta_{n})\right], \quad 0 \le x < d$$
 (57)

which represents the superposition of a set of transmitted and reflected electron waves inside the gap, where  $\eta_n = [\frac{\varepsilon + n\hbar\omega - E_F - W - e^2F_1^2/4m_e\omega^2}{eV}d + x + \frac{eF_1\cos(\omega t)}{m_e\omega^2}](\frac{2em_eV}{\hbar^2d})^{\frac{1}{3}}$ , and  $T_{1n}$  and  $T_{2n}$  are the coefficients.

For  $x \ge d$ , an exact solution of electron wave function is,

$$\psi(x,t) = \sum_{n=-\infty}^{\infty} T_{3n} \exp\left(-i\frac{\varepsilon + n\hbar\omega}{\hbar}t\right) \exp\left[ik_n x + i\frac{eF_1 d\sin(\omega t)}{\hbar\omega}\right], x \ge d$$
 (58)

which shows the superposition of transmitted electron plane waves with energies  $\varepsilon + n\hbar\omega$ , due to multiphoton absorption (n>0), direct tunneling (n=0) and multiphoton emission (n<0), where the wavenumber  $k_n = \sqrt{2m_e(\varepsilon + n\hbar\omega + eV)/\hbar^2}$  and  $T_{3n}$  is the transmission coefficient.

By applying the boundary conditions that both the electron wave function  $\psi(x,t)$  and its derivative  $\partial \psi(x,t)/\partial x$  are continuous at x=0 and x=d, and taking Fourier transform, we obtain, in nondimensional quantities [6][61][62],  $\bar{\varepsilon}=\varepsilon/W$ ,  $\bar{\omega}=\omega\hbar/W$ ,  $\bar{t}=tW/\hbar$ ,  $\bar{E}_F=E_F/W$ ,  $\bar{x}=x/\lambda_0$ ,  $\bar{t}=tW/\lambda_0$ ,  $\bar{t}=tW/\hbar$ , the following equations,

$$\sum_{n=-\infty}^{\infty} T_{1n} \left[ \sqrt{\overline{\varepsilon} + m\overline{\omega}} P_{1n(n-m)} + Q_{1n(n-m)} \right] + T_{2n} \left[ \sqrt{\overline{\varepsilon} + m\overline{\omega}} P_{2n(n-m)} + Q_{2n(n-m)} \right]$$

$$= 2\sqrt{\overline{\varepsilon}} \delta(m)$$

$$\sum_{n=-\infty}^{\infty} \left[ \sqrt{\overline{\varepsilon} + m\overline{\omega} + \overline{V}} U_{1n(n-m)} - V_{1n(n-m)} \right] T_{1n} + \left[ \sqrt{\overline{\varepsilon} + m\overline{\omega} + \overline{V}} U_{2n(n-m)} - V_{2n(n-m)} \right] T_{2n}$$
(59)

$$=0 (60)$$

$$\sum_{n=-\infty}^{\infty} T_{1n} U_{1n(n-m)} + T_{2n} U_{2n(n-m)} = T_{3m} \exp\left(i\bar{d}\sqrt{\bar{\varepsilon} + m\bar{\omega} + \bar{V}}\right)$$
 (61)

where  $\delta(m)$ ,  $P_{1n(n-m)}$ ,  $Q_{1n(n-m)}$ ,  $P_{2n(n-m)}$ ,  $Q_{2n(n-m)}$ ,  $U_{1n(n-m)}$ ,  $V_{1n(n-l)}$ ,  $U_{2n(n-m)}$ , and  $V_{2n(n-l)}$  are given by,

$$\delta(m) = \begin{cases} 1, & m = 0, \\ 0, & m \neq 0, \end{cases} \tag{62a}$$

$$P_{1nl} = \frac{1}{2\pi} \int_0^{2\pi} p_{1n}(\overline{\omega}\overline{t}) e^{-il\overline{\omega}\overline{t}} d(\overline{\omega}\overline{t}), \quad Q_{1nl} = \frac{1}{2\pi} \int_0^{2\pi} q_{1n}(\overline{\omega}\overline{t}) e^{-il\overline{\omega}\overline{t}} d(\overline{\omega}\overline{t}), \quad (62b)$$

$$P_{2nl} = \frac{1}{2\pi} \int_0^{2\pi} p_{2n}(\overline{\omega}\overline{t}) e^{-il\overline{\omega}\overline{t}} d(\overline{\omega}\overline{t}), \quad Q_{2nl} = \frac{1}{2\pi} \int_0^{2\pi} q_{2n}(\overline{\omega}\overline{t}) e^{-il\overline{\omega}\overline{t}} d(\overline{\omega}\overline{t}), \quad (62c)$$

$$p_{1n}(\overline{\omega}\overline{t}) = Ai(\alpha_n)f(\overline{\omega}\overline{t}), \tag{62d}$$

$$q_{1n}(\overline{\omega}\overline{t}) = \left[Ai(\alpha_n)\frac{\overline{F}_1\sin(\overline{\omega}\overline{t})}{\overline{\omega}} + iAi'(\alpha_n)(\overline{V}/\overline{d})^{\frac{1}{3}}\right]f(\overline{\omega}\overline{t}),\tag{62e}$$

$$p_{2n}(\overline{\omega}\overline{t}) = Bi(\alpha_n)f(\overline{\omega}\overline{t}), \tag{62}$$

$$q_{2n}(\bar{\omega}\bar{t}) = [Bi(\alpha_n)\frac{\bar{F}_1\sin(\bar{\omega}\bar{t})}{\bar{\omega}} + iBi'(\alpha_n)(\bar{V}/\bar{d})^{\frac{1}{3}}]f(\bar{\omega}\bar{t}), \tag{62g}$$

$$U_{1nl} = \frac{1}{2\pi} \int_0^{2\pi} u_{1n}(\overline{\omega}\overline{t}) e^{-il\overline{\omega}\overline{t}} d(\overline{\omega}\overline{t}), \quad V_{1nl} = \frac{1}{2\pi} \int_0^{2\pi} v_{1n}(\overline{\omega}\overline{t}) e^{-il\overline{\omega}\overline{t}} d(\overline{\omega}\overline{t}), \quad (62h)$$

$$U_{2nl} = \frac{1}{2\pi} \int_0^{2\pi} u_{2n}(\overline{\omega}\overline{t}) e^{-il\overline{\omega}\overline{t}} d(\overline{\omega}\overline{t}), \quad V_{2nl} = \frac{1}{2\pi} \int_0^{2\pi} v_{2n}(\overline{\omega}\overline{t}) e^{-il\overline{\omega}\overline{t}} d(\overline{\omega}\overline{t}), \quad (62i)$$

$$u_{1n}(\bar{\omega}\bar{t}) = Ai(\gamma_n)f(\bar{\omega}\bar{t}), \tag{62j}$$

$$v_{1n}(\overline{\omega}\overline{t}) = \left[Ai(\gamma_n)\frac{\overline{F}_1\sin(\overline{\omega}\overline{t})}{\overline{\omega}} + iAi'(\gamma_n)(\overline{V}/\overline{d})^{\frac{1}{3}}\right]f(\overline{\omega}\overline{t}),\tag{62k}$$

$$u_{2n}(\overline{\omega}\overline{t}) = Bi(\gamma_n)f(\overline{\omega}\overline{t}), \tag{62l}$$

$$v_{2n}(\overline{\omega}\overline{t}) = [Bi(\gamma_n)\frac{\overline{F}_1\sin(\overline{\omega}\overline{t})}{\overline{\omega}} + iBi'(\gamma_n)(\overline{V}/\overline{d})^{\frac{1}{3}}]f(\overline{\omega}\overline{t}), \tag{62m}$$

$$f(\overline{\omega}\overline{t}) = \exp\left[-i\frac{2\overline{F}_1\overline{V}}{\overline{d}\overline{\omega}^3}\sin(\overline{\omega}\overline{t}) + i\frac{\overline{F}_1^2}{4\overline{\omega}^3}\sin(2\overline{\omega}\overline{t})\right],\tag{62n}$$

with  $\alpha_n = -[\bar{E}_n \bar{d}/\bar{V} + 2\bar{F}_1 \cos{(\bar{\omega}\bar{t})}/\bar{\omega}^2](\bar{V}/\bar{d})^{\frac{1}{3}}$ ,  $\gamma_n = -[\bar{E}_n \bar{d}/\bar{V} + \bar{d} + 2\bar{F}_1 \cos{(\bar{\omega}\bar{t})}/\bar{\omega}^2](\bar{V}/\bar{d})^{\frac{1}{3}}$ , and  $\bar{E}_n = \bar{\varepsilon} + n\bar{\omega} - \bar{E}_F - \bar{U}_p - 1$ . The coefficients  $T_{1n}$ ,  $T_{2n}$ , and  $T_{3n}$  (and therefore  $R_{1n}$ ) is then calculated from Equations (59), (60) and (61).

The normalized transmitted current density is defined as the ratio of the transmitted probability current density over the incident probability current density,  $w(\varepsilon, x, t) = J_t(\varepsilon, x, t)/J_i(\varepsilon, x, t)$ , where the probability current density  $j(x, t) = (i\hbar/2m_e)(\psi\nabla\psi^* - \psi^*\nabla\psi) = (i\hbar/2m_e)(\psi\nabla\psi) = (i\hbar/$ 

 $2m_e$ )  $\sum_{n=-\infty}^{\infty} \sum_{l=-\infty}^{\infty} (\psi_n \nabla \psi_l^* - \psi_n^* \nabla \psi_l)$ . Thus, the normalized instantaneous transmitted current density in the metal on the right-hand side of Figure 5.6(a) (i.e., x > d) is found to be,

$$w(\bar{\varepsilon}, \bar{x}, \bar{t}) = \frac{1}{\sqrt{\bar{\varepsilon}}} \sum_{n=-\infty}^{\infty} \sum_{l=-\infty}^{\infty} Re\{e^{i(l-n)\bar{\omega}\bar{t}} T_{3n} T_{3l}^* D\},$$
 (63)

where  $D=\mathrm{e}^{i\,[\sqrt{\overline{\varepsilon}+n\overline{\omega}+\overline{V}}-(\sqrt{\overline{\varepsilon}+l\overline{\omega}+\overline{V}})^*]\bar{x}}(\sqrt{\overline{\varepsilon}+l\overline{\omega}+\overline{V}})^*$ . The time-averaged transmitted current density is,

$$\langle w(\bar{\varepsilon}) \rangle = \sum_{n=-\infty}^{\infty} \langle w_n(\bar{\varepsilon}) \rangle, \quad \langle w_n(\bar{\varepsilon}) \rangle = \text{Re}\left( |T_{3n}|^2 \sqrt{1 + n\bar{\omega}/\bar{\varepsilon} + \bar{V}/\bar{\varepsilon}} \right), \tag{64}$$

where  $\langle w_n \rangle$  represents the time-averaged transmitted current density through *n*-photon process, with transmitted electrons of energy  $\varepsilon + n\hbar\omega$  [6].

For the photoemission from right metal-vacuum interface of the gap in Figure 5.6(a), electrons would see a potential barrier subjected to a negative dc electric field  $F_0 = -V/d(<0)$  and laser field  $F_1\cos(\omega t)$ , as shown in Figure 5.6(c). Thus, the time-dependent potential barrier in Figure 5.6(c) is [6][61][62][74][106],

$$\Phi(x,t) = \begin{cases} 0 & x < 0 \\ E_F + W + eVx/d - eF_1x\cos(\omega t) & 0 \le x < d \\ eV - eF_1d\cos(\omega t) & x \ge d, \end{cases}$$
(65)

where  $E_F$  and W are the Fermi energy and work function of the right metal in Figure 5.6(a) respectively, and V is the magnitude of the applied dc bias. Other parameters have the same definition as that in Equation (43), with  $F_1$  of opposite sign (i.e., 180 degree out of phase) of that in Figure 5.6(b) at any time instant for a given laser field.

Solving the TDSE with the potential energy given in Equation (65) yields the electron wave function for x < 0,

$$\psi(x,t) = \exp\left(-\frac{i\varepsilon t}{\hbar} + ik_0 x\right) + \sum_{n=-\infty}^{\infty} R_{2n} \exp\left(-i\frac{\varepsilon + n\hbar\omega}{\hbar}t - ik_n x\right), x < 0$$
 (66)

where the wavenumber  $k_0=\sqrt{2m_e\varepsilon/\hbar^2}$  and  $k_n=\sqrt{2m_e(\varepsilon+n\hbar\omega)/\hbar^2}$ , and  $R_{2n}$  is the reflection coefficient.

For  $0 \le x < d$  (in the gap), the exact solution of electron wave function is found to be (see Appendix E for the method),

$$\psi(x,t) = \sum_{n=-\infty}^{\infty} \exp\left[-i\frac{\varepsilon + n\hbar\omega}{\hbar}t\right] \exp\left[\frac{ie^2VF_1\sin(\omega t)}{\hbar dm_e\omega^3} + \frac{ixeF_1\sin(\omega t)}{\hbar\omega} + \frac{ie^2F_1^2\sin(2\omega t)}{8m_e\hbar\omega^3}\right] \times \left[T_{4n}Ai(-\eta_n) + T_{5n}Bi(-\eta_n)\right], \quad 0 \le x < d$$
(67)

where  $\eta_n = \left[-\frac{\varepsilon + n\hbar\omega - E_F - W - e^2F_1^2/4m_e\omega^2}{eV}d + x + \frac{eF_1\cos(\omega t)}{m_e\omega^2}\right]\left(\frac{2em_eV}{\hbar^2d}\right)^{\frac{1}{3}}$ , and  $T_{4n}$  and  $T_{5n}$  are the coefficients.

For  $x \ge d$ , an exact solution of electron wave function is,

$$\psi(x,t) = \sum_{n=-\infty}^{\infty} T_{6n} \exp\left(-i\frac{\varepsilon + n\hbar\omega}{\hbar}t\right) \exp\left[ik_n x + i\frac{eF_1 d\sin(\omega t)}{\hbar\omega}\right], x \ge d \qquad (68)$$

where the wavenumber  $k_n = \sqrt{2m_e(\varepsilon + n\hbar\omega - eV)/\hbar^2}$  and  $T_{6n}$  is the transmission coefficient.

By applying the boundary conditions that both the electron wave function  $\psi(x,t)$  and its derivative  $\partial \psi(x,t)/\partial x$  are continuous at x=0 and x=d, and taking Fourier transform, we obtain the following equations,

$$\sum_{n=-\infty}^{\infty} T_{4n} \left[ \sqrt{\overline{\varepsilon} + m\overline{\omega}} P_{4n(n-m)} + Q_{4n(n-m)} \right] + T_{5n} \left[ \sqrt{\overline{\varepsilon} + m\overline{\omega}} P_{5n(n-m)} + Q_{5n(n-m)} \right]$$

$$= 2\sqrt{\overline{\varepsilon}} \delta(m)$$

$$\sum_{n=-\infty}^{\infty} \left[ \sqrt{\overline{\varepsilon} + m\overline{\omega} - \overline{V}} U_{4n(n-m)} - V_{4n(n-m)} \right] T_{4n} + \left[ \sqrt{\overline{\varepsilon} + m\overline{\omega} - \overline{V}} U_{5n(n-m)} - V_{5n(n-m)} \right] T_{5n}$$

$$= 0$$

$$(70)$$

$$\sum_{n=-\infty}^{\infty} T_{4n} U_{4n(n-m)} + T_{5n} U_{5n(n-m)} = T_{6m} \exp\left(i\bar{d}\sqrt{\bar{\varepsilon} + m\bar{\omega} - \bar{V}}\right)$$
 (71)

where  $\delta(m)$ ,  $P_{4n(n-m)}$ ,  $Q_{4n(n-m)}$ ,  $P_{5n(n-m)}$ ,  $Q_{5n(n-m)}$ ,  $U_{4n(n-m)}$ ,  $V_{4n(n-l)}$ ,  $U_{5n(n-m)}$ , and  $V_{5n(n-l)}$  are given by,

$$\delta(m) = \begin{cases} 1, & m = 0, \\ 0, & m \neq 0, \end{cases}$$
 (72a)

$$P_{4nl} = \frac{1}{2\pi} \int_0^{2\pi} p_{4n}(\overline{\omega}\overline{t}) e^{-il\overline{\omega}\overline{t}} d(\overline{\omega}\overline{t}), \quad Q_{4nl} = \frac{1}{2\pi} \int_0^{2\pi} q_{4n}(\overline{\omega}\overline{t}) e^{-il\overline{\omega}\overline{t}} d(\overline{\omega}\overline{t}), \quad (72b)$$

$$P_{5nl} = \frac{1}{2\pi} \int_{0}^{2\pi} p_{5n}(\overline{\omega}\overline{t}) e^{-il\overline{\omega}\overline{t}} d(\overline{\omega}\overline{t}), \quad Q_{5nl} = \frac{1}{2\pi} \int_{0}^{2\pi} q_{5n}(\overline{\omega}\overline{t}) e^{-il\overline{\omega}\overline{t}} d(\overline{\omega}\overline{t}), \quad (72c)$$

$$p_{5n}(\overline{\omega}\overline{t}) = Ai(\alpha_n)f(\overline{\omega}\overline{t}), \tag{72d}$$

$$q_{5n}(\overline{\omega}\overline{t}) = \left[Ai(\alpha_n)\frac{\overline{F}_1\sin(\overline{\omega}\overline{t})}{\overline{\omega}} - iAi'(\alpha_n)(\overline{V}/\overline{d})^{\frac{1}{3}}\right]f(\overline{\omega}\overline{t}),\tag{72e}$$

$$p_{6n}(\overline{\omega}\overline{t}) = Bi(\alpha_n)f(\overline{\omega}\overline{t}), \tag{72}f$$

$$q_{6n}(\bar{\omega}\bar{t}) = [Bi(\alpha_n)\frac{\bar{F}_1\sin(\bar{\omega}\bar{t})}{\bar{\omega}} - iBi'(\alpha_n)(\bar{V}/\bar{d})^{\frac{1}{3}}]f(\bar{\omega}\bar{t}), \tag{72g}$$

$$U_{4nl} = \frac{1}{2\pi} \int_0^{2\pi} u_{4n}(\overline{\omega}\overline{t}) e^{-il\overline{\omega}\overline{t}} d(\overline{\omega}\overline{t}), \quad V_{4nl} = \frac{1}{2\pi} \int_0^{2\pi} v_{4n}(\overline{\omega}\overline{t}) e^{-il\overline{\omega}\overline{t}} d(\overline{\omega}\overline{t}), \quad (72h)$$

$$U_{5nl} = \frac{1}{2\pi} \int_0^{2\pi} u_{5n}(\overline{\omega}\overline{t}) e^{-il\overline{\omega}\overline{t}} d(\overline{\omega}\overline{t}), \quad V_{5nl} = \frac{1}{2\pi} \int_0^{2\pi} v_{5n}(\overline{\omega}\overline{t}) e^{-il\overline{\omega}\overline{t}} d(\overline{\omega}\overline{t}), \quad (72i)$$

$$u_{4n}(\overline{\omega}\overline{t}) = Ai(\gamma_n)f(\overline{\omega}\overline{t}), \tag{72j}$$

$$v_{4n}(\overline{\omega}\overline{t}) = [Ai(\gamma_n)\frac{\overline{F}_1\sin(\overline{\omega}\overline{t})}{\overline{\omega}} - iAi'(\gamma_n)(\overline{V}/\overline{d})^{\frac{1}{3}}]f(\overline{\omega}\overline{t}), \tag{72k}$$

$$u_{5n}(\overline{\omega}\overline{t}) = Bi(\gamma_n)f(\overline{\omega}\overline{t}), \tag{72l}$$

$$v_{5n}(\overline{\omega}\overline{t}) = [Bi(\gamma_n)\frac{\overline{F}_1\sin(\overline{\omega}\overline{t})}{\overline{\omega}} - iBi'(\gamma_n)(\overline{V}/\overline{d})^{\frac{1}{3}}]f(\overline{\omega}\overline{t}), \tag{72m}$$

$$f(\overline{\omega}\overline{t}) = \exp\left[i\frac{2\overline{F}_1\overline{V}}{\overline{d}\overline{\omega}^3}\sin(\overline{\omega}\overline{t}) + i\frac{\overline{F}_1^2}{4\overline{\omega}^3}\sin(2\overline{\omega}\overline{t})\right],\tag{72n}$$

with  $\alpha_n = [2\bar{F}_1\cos{(\bar{\omega}\bar{t})}/\bar{\omega}^2 - \bar{E}_n\bar{d}/\bar{V}](\bar{V}/\bar{d})^{\frac{1}{3}}, \ \gamma_n = [\bar{d} + 2\bar{F}_1\cos{(\bar{\omega}\bar{t})}/\bar{\omega}^2 - \bar{E}_n\bar{d}/\bar{V}](\bar{V}/\bar{d})^{\frac{1}{3}},$ and  $\bar{E}_n = \bar{\varepsilon} + n\bar{\omega} - \bar{E}_F - \bar{U}_p - 1$ . The coefficients  $T_{4n}$ ,  $T_{5n}$ , and  $T_{6n}$  (and therefore  $R_{2n}$ ) is then calculated from Equations (69), (70) and (71).

The normalized instantaneous transmitted current density in the metal on the left-hand side of Figure 5.6(a), defined as the ratio of the transmitted probability current density over the incident probability current density,  $w(\varepsilon, x, t) = J_t(\varepsilon, x, t)/J_i(\varepsilon, x, t)$ , is obtained as

$$w(\bar{\varepsilon}, \bar{x}, \bar{t}) = \frac{1}{\sqrt{\bar{\varepsilon}}} \sum_{n=-\infty}^{\infty} \sum_{l=-\infty}^{\infty} Re\{e^{i(l-n)\bar{\omega}\bar{t}} T_{6n} T_{6l}^* D\}, \tag{73}$$

where  $D=\mathrm{e}^{i\,[\sqrt{\bar{\varepsilon}}+n\bar{\omega}-\overline{V}-(\sqrt{\bar{\varepsilon}}+l\bar{\omega}-\overline{V})^*]\bar{x}}(\sqrt{\bar{\varepsilon}}+l\bar{\omega}-\overline{V})^*$ . The time-averaged transmitted current density is,

$$\langle w(\bar{\varepsilon}) \rangle = \sum_{n=-\infty}^{\infty} \langle w_n(\bar{\varepsilon}) \rangle, \quad \langle w_n(\bar{\varepsilon}) \rangle = \text{Re}\left( |T_{6n}|^2 \sqrt{1 + n\bar{\omega}/\bar{\varepsilon} - \bar{V}/\bar{\varepsilon}} \right). \tag{74}$$

## 5.3.2 Results and Discussion

In the calculation of this section, positive dc field  $(F_0 > 0)$  and negative dc field  $(F_0 < 0)$  cases denote the electron emission from left metal surface and right metal surface of the vacuum nanogap with the external dc voltage  $V = |F_0|d$  shown in Figure 5.6(a), respectively. Unless mentioned otherwise, the default value of the laser wavelength is 800 nm ( $\hbar\omega = 1.55 \text{ eV}$ ), the metals on both sides of the gap are assumed to be gold [17][20][65][111], with Fermi energy  $E_F = 5.53 \text{ eV}$  and work function W = 5.1 eV, and the photoemission current is calculated from Equations (64) and (74). Since most of the electrons are emitted with initial energies near the Fermi level [6][76][86][87], we choose the electron initial energy  $\varepsilon = E_F$  for simplicity.

In Figure 5.7, we plot the photoelectron energy spectra under different applied dc bias with fixed gap distance d = 5 nm. Increasing the dc field  $F_0$  from 1 to 3 V/nm increases the left-to-right photoelectron transmission current by about two orders of magnitude and shifts the corresponding

dominant electron emission process from three-photon absorption to two-photon absorption, as shown in Figure 5.7(a). This is because under a larger dc field, the potential barrier near the left metal-vacuum interface becomes narrower, enabling the less photon transition process (cf. Figure 5.7(b)). Nevertheless, with the larger dc field, the right-to-left photoelectron current dramatically decreases and the dominant emission shifts to the higher order multiphoton absorption (see Figure 5.7(c)). This can be explained by that under a stronger dc bias V, electrons from the right-side metal surface of the gap need to absorb more photons to overcome the potential barrier with increased height in the gap for the emission, as shown in Figure 5.7(d). These observed changes are also well reflected in Figures 5.8(a) and 5.8(b) which show the total time-averaged transmission current density (w) from left (Figure 5.8(a)) and right (Figure 5.8(b)) metal surface of the nano gap of Figure 5.6(a) as a function of laser field  $F_1$  with different applied dc bias. Here, the increasing (decreasing) slope of the curve of  $\langle w \rangle$  with dc field  $F_0$  manifests the shift of main emission process to the larger (smaller) n-photon absorption. Also, the slop of  $\langle w \rangle$  versus  $F_1$ follows the power-law scaling of photoemission  $\langle w \rangle \propto F_1^{2n}$ , indicating the dominant *n*-photon emission process. The value of n is consistent with the observation in Figures 5.7(a) and 5.7(c) (cf. the cases with  $F_0 = \pm 1$  and  $\pm 3$  V/nm)).

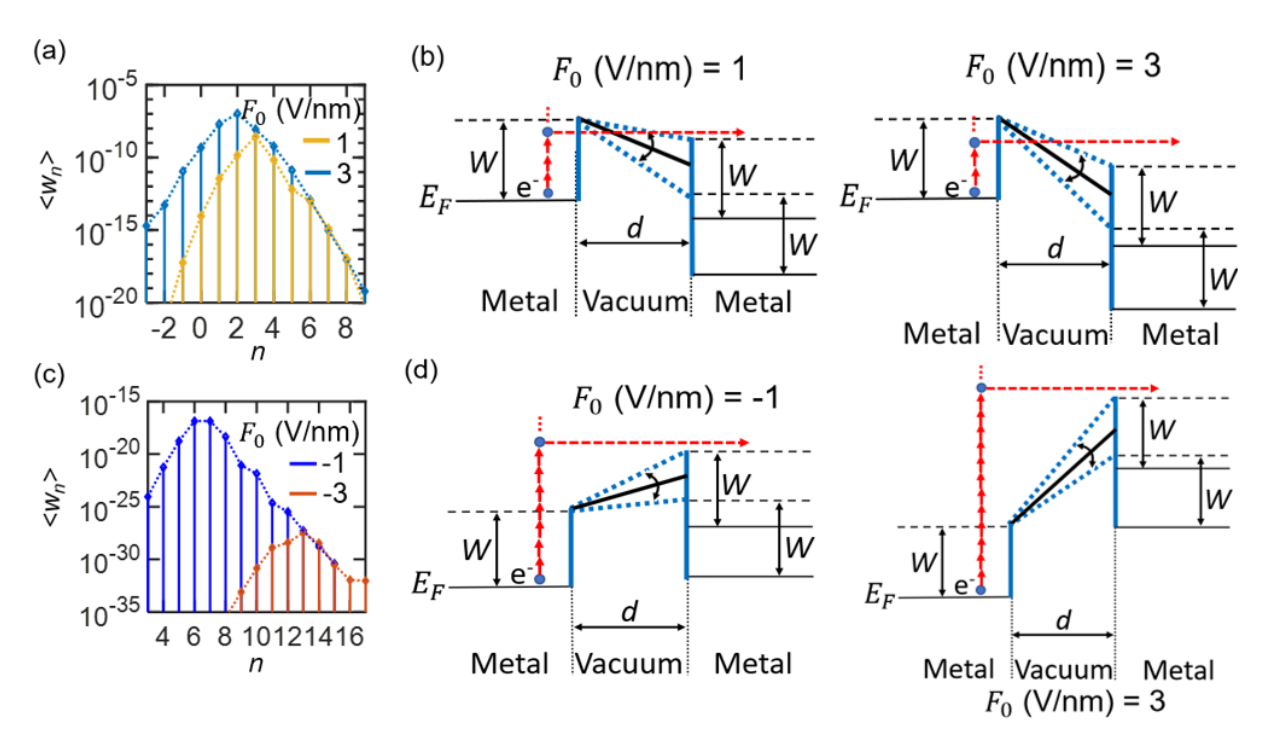


Figure 5.7: Photoelectron energy spectra for dc field (a)  $F_0 = 1$  and 3 V/nm and (c)  $F_0 = -1$  and -3 V/nm. Emission mechanisms when (b)  $F_0 = 1$  and 3 V/nm and (d)  $F_0 = -1$  and -3 V/nm. Here, laser field  $F_1 = 1$  V/nm and gap distance d = 5 nm.

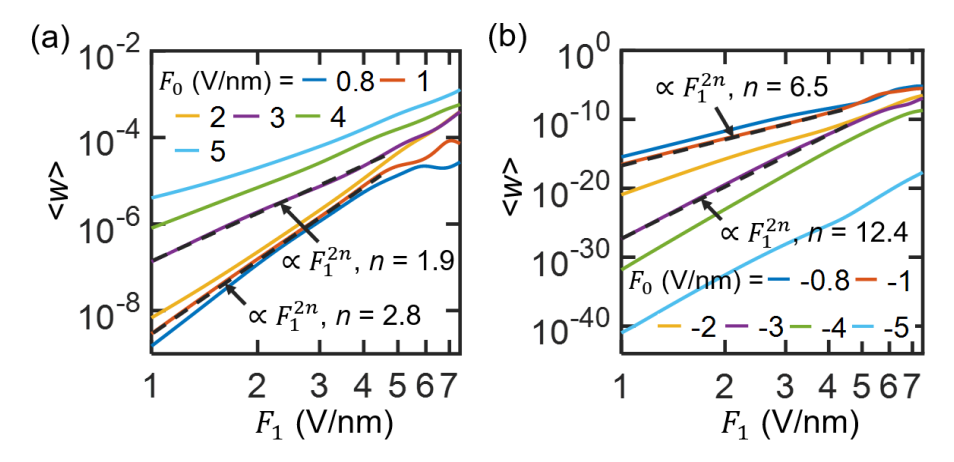


Figure 5.8: Normalized total time-averaged emission current density  $\langle w \rangle$  as a function of laser field  $F_1$  for various dc fields  $F_0$ . The gap distance d is fixed at 5 nm. The black dashed lines display the scale  $\langle w \rangle \propto F_1^{2n}$ . Here, n=2.8, 1.9, 6.5 and 12.4 when  $F_0=1, 3, -1$ , and -3 V/nm is consistent with the observed orders of domination multiphoton emission channel in Figures 5.7(a) and 5.7(c).

In Figure 5.9, we plot the total time-averaged emission current density  $\langle w \rangle$  as a function of gap distance d under various dc fields  $F_0$  and laser fields  $F_1$ . Without the dc field  $(F_0 = 0)$ , the emission current  $\langle w \rangle$  from left or right metal surface would continuously oscillate around the current from

a single surface (cf. the dashed lines) as d increases, which is due to the interference of electron plane waves inside the gap, and the oscillation amplitude remains unchanged, due to the exclusion of image charge and space charge effects in our calculation. After applying a strong dc field, it is found that the oscillation behavior in the photocurrent is gradually suppressed with the increasing d, and the left-to-right emission current eventually approaches that from single metal surface. Besides, our calculation shows with a very narrow gap (d < 0.5 nm), the emission current from the left and right surfaces has the same order of magnitude, regardless of applied laser intensity and dc bias. This is because the gap-dependent direct tunneling emission dominates the transmission. As the gap distance d increases, compared to the emission current from left metal surface, the current from right surface is more greatly suppressed. This manifests that varying the gap distance is able to greatly tune the dc-induced rectification on the photoelectron emission in a nanogap. Our calculation displays the gap distance of larger than 1 nm is enough to achieve full rectification.

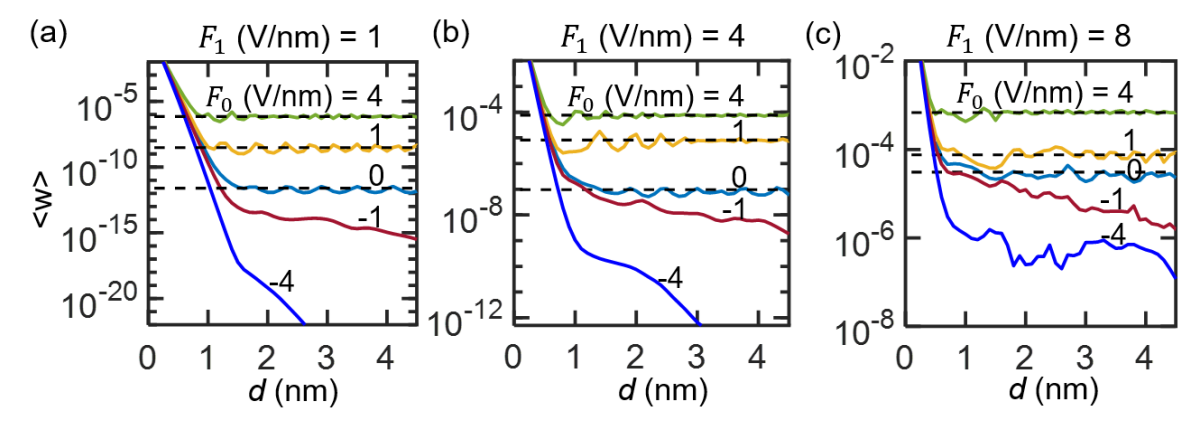


Figure 5.9: Normalized total time-averaged emission current density  $\langle w \rangle$  as a function of gap distance d for different dc fields  $F_0$  and laser fields  $F_1$ . Dashed lines denote the emission current density from single surface, which is obtained from Reference [6].

Figures 5.10(a) and 5.10(b) show the total emission current density  $\langle w \rangle$  as a function of dc field  $F_0$  under different laser fields  $F_1$ . The calculated exponentially increasing and decreasing trend with dc field  $F_0$  exhibits good coincidence with the numerical simulation (see Figure 3 in Reference [66]). Figure 5.10(c) displays the net emission current density, defined as the difference

between the left-to-right and the right-to-left emission current, as a function of dc field  $F_0$  for laser field  $F_1 = 0.4$ , 0.8 and 1 V/nm. It can be seen that as dc bias approaches 0, the net emission current also approaches the minimum value of 0. When the dc bias increases, the net current exponentially increases, indicating it is gradually dictated by the left-to-right photocurrent. This uncovers the rectification effect of external dc bias on the photoemission in a nanoscale gap [17].

In Figures 5.11 and 5.12, we plot the spatiotemporal evolution of emitted electron density from left and right metal surfaces respectively, under different combinations of dc and laser electric fields. Here, the gap distance d is fixed at 5 nm. As clearly seen in Figure 5.11(a), with the external dc field  $F_0 = 1$  V/nm and laser field  $F_1 = 0.1$  V/nm, parts of electrons emitted from left metal surface are reflected back and forth inside the gap, which is in line with the numerical simulation results in Figure 2(a) of Reference [66]. Also, our calculation shows increasing the laser field  $F_1$  causes

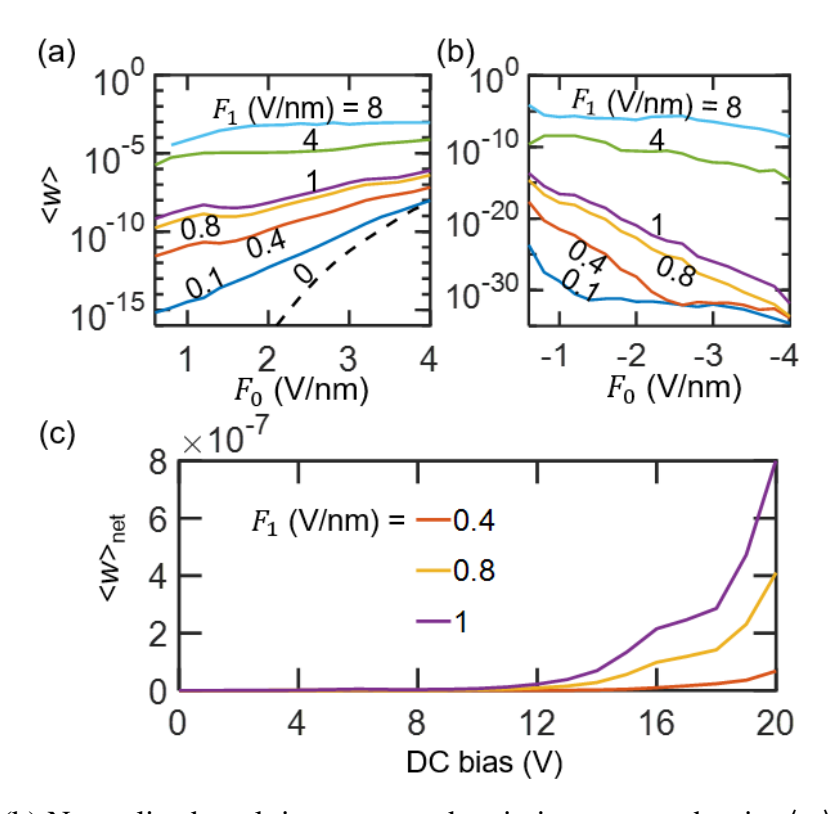


Figure 5.10: (a),(b) Normalized total time-averaged emission current density  $\langle w \rangle$  as a function of dc field  $F_0$  for different laser fields  $F_1$ . (c) The dependence of net emission current density  $\langle w \rangle$  on the applied dc bias for different laser fields  $F_1$ . Here, gap distance d is fixed at 5 nm.

more oscillatory emission features within the gap (cf. Figures 5.11(a)-5.11(c)), which is due to the stronger quiver motion of emitted electrons under strong laser electric fields. When adding a large dc field  $F_0 = 5$  V/nm (see Figures 5.11(d)-5.11(f)), dc field-like electron emission pattern dominates the whole regime, and due to the strong acceleration, electrons enter the right-side metal with higher velocity (cf. the slope of classical trajectories). On the other hand, for the photoelectron emission from right surface (see Figure 5.12), the addition of 1 V/nm dc field confines most of electrons inside the vacuum gap, and only when the laser field  $F_1$  is increased up to 8 V/nm could a small part of electrons escape from the gap into the left metal (cf. Figure 5.12(c)). Similar trend with the increasing  $F_1$  is observed in Figures 5.12(d)-5.12(f), except that most electrons are constrained in the strong surface oscillation regime when applied dc field is 5 V/nm.

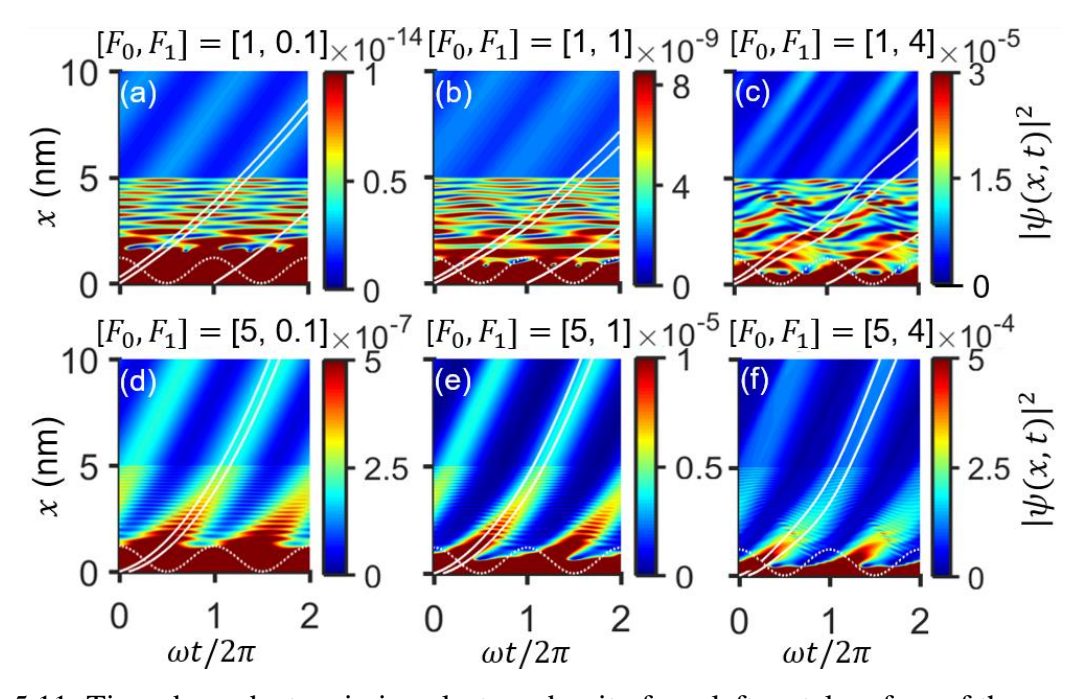


Figure 5.11: Time-dependent emission electron density from left metal surface of the nanogap in Figure 5.6(a) as a function of time t and space x under various combinations of dc and laser fields. Solid white lines show the corresponding classical trajectories [76]. Dotted white lines show the laser electric field. Here, gap distance d is fixed at 5 nm. The units of dc field  $F_0$  and laser field  $F_1$  are V/nm in all figures.

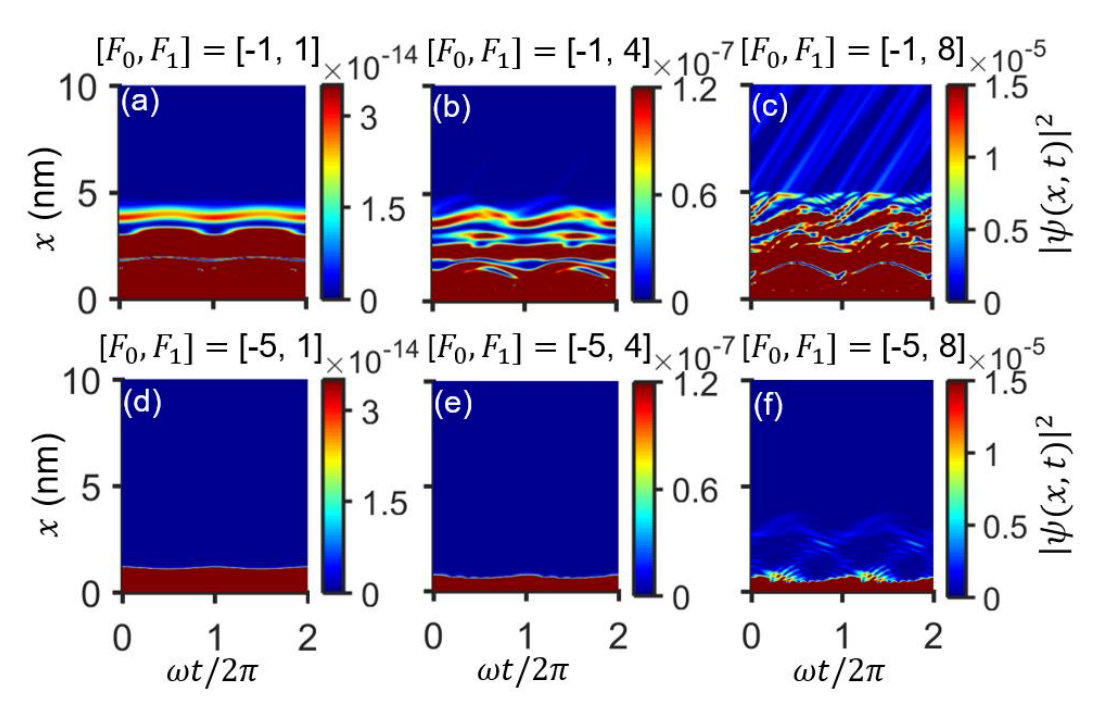


Figure 5.12: Time-dependent emission electron density from right metal surface of the nanogap in Figure 5.6(a) as a function of time t and space x under various combinations of dc and laser fields. Here, gap distance d is fixed at 5 nm. The units of dc field  $F_0$  and laser field  $F_1$  are V/nm in all figures.

## 5.3.3 Summary on Photoelectron Transport with DC Bias

In this section, by exactly solving the TDSE, we present analytical models for photoelectron emission from left- and right-side surfaces of a dc-biased nanoscale metal-vacuum-metal gap driven by a single-frequency laser field. Our results reveal the underlying photoemission process, time-averaged emission current and spatiotemporal dynamics of photoelectrons from both sides of the nano gap under different combinations of dc bias, laser fields and gap distances. Our calculation shows the addition of a large dc field can greatly reduce the interference effect induced oscillation in the total emission current, and demonstrates that in addition to the applied dc bias, changing the gap distance is also able to achieve strong rectification to the photoelectron emission in a dc-biased nano-vacuum gap. Our results may be helpful for the future design of ultrafast optoelectronic devices, such as photodetectors.

#### **CHAPTER 6**

# SUMMARY AND SUGGESTED FUTURE WORK

## **6.1 Summary**

In this thesis, we develop quantum analytical models to study nonlinear ultrafast optical-field induced photoelectron emission from biased metal surfaces, by exactly solving the TDSE. We consider two-color laser induced photoelectron emission with and without dc bias, interference modulation of photoemission using two lasers of the same frequency, nonlinear ultrafast photoemission from a dc-biased surface triggered by few-cycle laser pulses, and laser induced photoelectron transport in nanogaps. Our analytical solution is valid for arbitrary laser parameters, including laser frequency, intensity, relative phase between two lasers, pulse duration, repetition rate, carrier-envelope phase, applied dc fields, gap distances, metal work function and Fermi level. Various emission processes, such as multiphoton over-barrier emission, dc-assisted optical tunneling emission and dc or optical field emission, are all included in our simple formulation. We provide comprehensive analysis of the photoelectron emission properties under different combinations of laser parameters and dc fields.

Under the illumination of two-color laser fields, our results show strong tunability on the photoelectron spectra, emission current, and current modulation, via the control of the phase delay, relative intensity, harmonic order of the two-color lasers, and dc bias, exhibiting good agreement with the experimental measurements. Application of our model to time-resolved photoelectron spectroscopy is demonstrated. Our study also suggests a practical way to maintain a strong current modulation, in the meantime, greatly increase the total emission current in two-color laser-induced electron emission, by simply adding a strong dc bias and a weak harmonic laser.

For the two-same frequency lasers induced photoelectron emission, we find strong interference modulation on electron emission can be achieved with low threshold value of the laser field ratio even with a strong dc field. Our study demonstrates the capability of using interference modulation by single-frequency laser pairs for practical measurements of time-resolved photoelectron energy spectra.

With few-cycle laser pulses, we identify the new signature of coherent interaction of adjacent laser pulses on photoemission, that is, the emitted charge per pulse oscillatorily changes as the laser pulse separation increases. For a well-separated single pulse, our calculations recover the experimentally measured features of sinusoidal CEP modulation to photoelectron emission and vanishing CEP sensitivity with a  $\pi$  phase shift in strong optical-field regime. Moreover, we find adding a large dc field is able to greatly enhance the photoelectron current and shorten the current pulse.

For the photoelectron emission in a metal-vacuum-metal nanogap, our calculation reveals the underlying photoemission processes, including direct tunneling, dc-assisted optical tunneling and over-barrier emission, and the transition between them, under different combinations of gap distance increases, dc bias and laser fields. For the zero dc field, our results show the oscillatory dependence of photoemission current on the gap distance in the multiphoton regime and the energy redistribution of photoelectrons across the two interfaces between the gap and the metals. We also find that decreasing the gap distance (before entering the direct tunneling regime) tends to extend the multiphoton regime to higher laser intensity. With the addition of large dc bias, the interference induced oscillation in photocurrent from metal-vacuum interface of the gap is found to be significantly reduced with the increasing gap spacing. Additionally, our calculation demonstrates

that besides the applied dc bias, changing the gap distance is also able to achieve great rectification to the photoelectron emission in a dc-biased nano-vacuum gap.

### **6.2** Suggested future work

As the works in this thesis are analytically solving the TDSE exactly, it is important to compare our solutions with those of perturbative treatments widely used in the literature, and the inverse LEED and LEED wave functions used for scattering problems [67][118]-[120]. It is also important to consider the effect of space charge in the electron emission process [34][36]. Suggested future work would also include the theoretical modeling of ultrashort pulsed laser induced photoelectron transport in nano-vacuum gaps and the rectification effects in nanogaps formed with dissimilar materials. It would also be interesting to study the effects surface states and materials (e.g., semiconductor and two-dimensional materials) by considering the energy dependent electron supply function inside the material and work function variations along the emission surface in the future. Ultimately, it is envisioned to build a hybrid model using our exact analytical solutions for simulating electron emission in practical geometries, such as sharp metal tips or cathodes with surface roughness, where effects such as the electron emission angle and space charge can be incorporated. The time-dependent field distribution near the emitter may be first calculated using a Maxwell solver. Next, our exact model can be applied along the surface of the emitter to give the instantaneous photoemission current. The emitted electrons can then be loaded into particlein-cell pusher to account for the detailed space charge effects and electron dynamics. Once such a tool becomes available, it would find immense applications in various areas, such as solid-state physics, strong fields, ultrafast sciences, vacuum electronics, and accelerators and beams.

**APPENDICES** 

### **EXACT SLOTUION OF ELECTRON WAVE FUNCTION**

Following Truscott [6][117], the time-dependent potential energy for  $x \ge 0$  (see Appendix A, B, and C) or  $0 \le x < d$  (see Appendix D and E) can be written as  $\Phi(x,t) = V(x,t) - xf(t)$ . Thus, the TDSE can be transformed to the coordinate system  $\xi$ , t, where  $\xi = x - q(t)$ , the displacement  $q(t) = (1/m_e) \int_0^t p(t') dt'$ , and  $p(t) = \int_0^t f(t') dt'$ , by assuming that  $\psi(x,t) = \phi(\xi,t)\chi(x,t)$ , with  $\chi(x,t) = \exp\left[-iEt/\hbar + ixp(t)/\hbar - (i/2\hbar m)\int_0^t p^2(t') dt'\right]$ , and E being a constant. Then, we have,

$$i\hbar \frac{\partial \phi(\xi,t)}{\partial t} = \left[ -\frac{\hbar^2}{2m_e} \frac{\partial^2}{\partial \xi^2} + U(\xi,t) - E \right] \phi(\xi,t), \tag{A1}$$

with  $U(\xi,t)=V(\xi,t)$ . By separation of variables,  $\phi(\xi,t)$  in Equation (A1) can be easily solved. From  $\psi(x,t)=\phi(\xi)\chi(x,t)$ , we obtain exact solution of electron wave function.

# APPENDIX A: Two-color laser induced photoemission without dc field

Based on the method above, we have the potential energy  $\Phi(x,t) = V(x,t) - xf(t)$ , with  $V(x,t) = V_0$  and  $f(t) = eF_1 \cos(\omega t) + eF_2 \cos(\beta \omega t + \theta)$  in the vacuum  $(x \ge 0)$ , and

$$\phi(\xi,t) = \phi(\xi) = e^{i\xi\sqrt{2m_e(E-V_0)/\hbar^2}}.$$
(A2)

From  $\psi(x,t)=\phi(\xi)\chi(x,t)$ , we obtain Equation (14) with  $E=\varepsilon+n\hbar\omega-e^2F_1^2/4m_e\omega^2-e^2F_2^2/4m_e\beta^2\omega^2$ .

### APPENDIX B: Two-color laser induced photoemission with dc field

We have the potential energy  $\Phi(x,t) = V(x,t) - xf(t)$ , with  $V(x) = V_0 - eF_0x$ , and  $f(t) = eF_1\cos(\omega t) + eF_2\cos(\beta\omega t + \theta)$  in the vacuum  $(x \ge 0)$ , and

$$\phi(\xi, t) = g(\xi) \exp\left[\frac{e^2 F_0 F_1 \sin(\omega t)}{i\hbar m_e \omega^3} + \frac{e^2 F_0 F_2 \sin(\beta \omega t + \theta)}{i\hbar m_e \beta^3 \omega^3}\right],\tag{A3}$$

where  $g(\xi) = Ai(-\eta) - iBi(-\eta)$  is the solution of the equation  $-(\hbar^2/2m_e)\partial^2 g(\xi)/\partial \xi^2 + (V_0 - E - eF_0\xi)g(\xi) = 0$ , where  $\eta = (2em_eF_0/\hbar^2)^{1/3}[(E - V_0)/eF_0 + \xi]$  [81][86]. From  $\psi(x,t) = \phi(\xi)\chi(x,t)$ , we obtain Equation (21) with  $E = \varepsilon + n\hbar\omega - e^2F_1^2/4m_e\omega^2 - e^2F_2^2/4m_e\beta^2\omega^2$ .

# **APPENDIX C: Few-cycle laser pulses induced photoemission**

We have the potential energy  $\Phi(x,t) = V(x,t) - xf(t)$ , with  $V(x) = E_F + W_{eff} - e(F_0 + F_1 a_0 \cos \phi)x$  and  $f(t) = e\sum_{n=-\infty,n\neq 0}^{+\infty} F_1 a_n \cos(\frac{n\pi}{L}t + \phi)$  (see Equations (33) and (34)), and

$$\phi(\xi,t) = g(\xi) \exp\left[\sum_{n=-\infty,n\neq 0}^{+\infty} \frac{e^2 a_n F_1(F_0 + F_1 a_0 \cos \phi) \sin (n\omega_E t + \phi)}{i\hbar m_e n^3 \omega_E^3}\right], \tag{A4}$$

where  $g(\xi) = Ai(-\eta) - iBi(-\eta)$  is the solution of the equation  $-(\hbar^2/2m_e)\partial^2 g(\xi)/\partial \xi^2 + [E_F + W_{eff} - E - e(F_0 + F_1 a_0 \cos \phi)\xi]g(\xi) = 0$ , where  $\eta = [2em_e(F_0 + F_1 a_0 \cos \phi)/\hbar^2]^{1/3}[(E - E_F - W_{eff})/e(F_0 + F_1 a_0 \cos \phi) + \xi]$  [81][86]. From  $\psi(x,t) = \phi(\xi,t)\chi(x,t)$ , we obtain Equation (35) with  $E = \varepsilon + l\hbar\omega_E - U_p$  and  $U_p = \sum_{n=-\infty,n\neq 0}^{+\infty} \frac{e^2F_1^2[a_n^2 + a_n a_{-n} \cos(2\phi)]}{4m_e n^2\omega_E^2}$ .

For the special case of dc field  $F_0=0$  and carrier-envelope phase  $\phi=(2n+1)\pi/2$ , with n being an integer, the solution of  $\psi(x,t)$  is revised by merely displacing  $g(\xi)$  in Equation (A4) with  $\exp[i\xi\sqrt{2m_eE}/\hbar]$ .

### APPENDIX D: Photoelectron transport in a nanoscale gap without dc bias

We have the potential energy  $\Phi(x,t) = V(x,t) - xf(t)$ , with  $V(x,t) = E_F + W$  and  $f(t) = eF_1 \cos(\omega t)$ , and

$$\phi(\xi,t) = \phi(\xi) = e^{\pm i\xi\sqrt{2m_e(E-V_0)/\hbar^2}}.$$
 (A5)

Here, "+" in  $\phi(\xi)$  denotes the electron wave travelling towards +x direction; "-" denotes the electron wave travelling towards -x direction. Due to the reflection of electron waves at metal-vacuum surfaces of x=0 and d (see Figure 5.1), the electron wave function  $\psi(x,t)$  inside the vacuum gap  $(0 \le x < d)$  should be the superposition of wave functions towards +x direction and -x direction. Then, from  $\psi(x,t) = \phi(\xi)\chi(x,t)$ , we obtain Equation (45) with  $E = \varepsilon + n\hbar\omega - e^2F_1^2/4m_e\omega^2$ .

### APPENDIX E: Photoelectron transport in a nanoscale gap with dc bias

For the photoemission from left metal-vacuum interface of the gap in Figure 5.6(a), we have the potential energy  $\Phi(x,t) = V(x,t) - xf(t)$ , with  $V(x,t) = V_0 - eVx/d$  where and  $f(t) = eF_1 \cos(\omega t)$ , and

$$\phi(\xi, t) = g(\xi) \exp\left[\frac{e^2 V F_1 \sin(\omega t)}{i\hbar d m_c \omega^3}\right]$$
 (A6)

where  $g(\xi) = Ai(-\eta) \pm iBi(-\eta)$  is the solution of the equation  $-(\hbar^2/2m_e)\partial^2 g(\xi)/\partial \xi^2 + (V_0 - E - eV\xi/d)g(\xi) = 0$ , where  $\eta = (2em_eV/d\hbar^2)^{1/3}[(E - V_0)d/eV + \xi]$  [81][86]. Here, "—" in  $g(\xi)$  denotes the electron wave travelling towards +x direction; "+" denotes the electron wave travelling towards -x direction. Due to the reflection of electron waves at metal-vacuum surfaces of x=0 and d (see Figure 5.6(a)), the electron wave function  $\psi(x,t)$  inside the vacuum gap  $(0 \le x < d)$  should be the superposition of wave functions towards +x direction and -x direction. Then, from  $\psi(x,t) = \phi(\xi)\chi(x,t)$ , we obtain Equation (57) with  $E = \varepsilon + n\hbar\omega - e^2F_1^2/4m_e\omega^2$ .

For the photoemission from right metal-vacuum interface of the gap in Figure 5.6(a), we have the potential energy  $\Phi(x,t) = V(x,t) - xf(t)$ , with  $V(x,t) = V_0 + eVx/d$  where and  $f(t) = eF_1 \cos(\omega t)$ , and

$$\phi(\xi, t) = g(\xi) \exp\left[\frac{e^2 V F_1 \sin(\omega t)}{i\hbar d m_e \omega^3}\right]$$
 (A7)

where  $g(\xi)=Ai(\eta)\pm iBi(\eta)$  is the solution of the equation  $-(\hbar^2/2m_e)\partial^2 g(\xi)/\partial\xi^2+(V_0-E+eV\xi/d)g(\xi)=0$ , where  $\eta=(2em_eV/d\hbar^2)^{1/3}[\xi-(E-V_0)d/eV]$  [81][86]. Here, "+" in  $g(\xi)$  denotes the electron wave travelling towards +x direction; "-" denotes the electron wave travelling towards -x direction. Due to the reflection of electron waves at metal-vacuum surfaces of x=0 and d (see Figure 5.6(a)), the electron wave function  $\psi(x,t)$  inside the vacuum gap  $(0 \le x < d)$  should be the superposition of wave functions towards +x direction and -x direction. Then, from  $\psi(x,t)=\phi(\xi)\chi(x,t)$ , we obtain Equation (67) with  $E=\varepsilon+n\hbar\omega-e^2F_1^2/4m_e\omega^2$ .

BIBLIOGRAPHY

#### **BIBLIOGRAPHY**

- [1] P. Agostini, F. Fabre, G. Mainfray, G. Petite, and N. K. Rahman, "Free-Free Transitions Following Six-Photon Ionization of Xenon Atoms," *Phys. Rev. Lett.*, vol. 42, no. 17, pp. 1127–1130, Apr. 1979.
- [2] P. Kruit, J. Kimman, and M. J. V. der Wiel, "Absorption of additional photons in the multiphoton ionisation continuum of xenon at 1064, 532 and 440 nm," *J. Phys. B: At. Mol. Phys.*, vol. 14, no. 19, pp. L597–L602, Oct. 1981.
- [3] P. Balcou, C. Cornaggia, A. S. L. Gomes, L. A. Lompre, and A. L\textquotesingleHuillier, "Optimizing high-order harmonic generation in strong fields," *J. Phys. B: At. Mol. Opt. Phys.*, vol. 25, no. 21, pp. 4467–4485, Nov. 1992.
- [4] M. Krüger, C. Lemell, G. Wachter, J. Burgdörfer, and P. Hommelhoff, "Attosecond physics phenomena at nanometric tips," *J. Phys. B: At. Mol. Opt. Phys.*, vol. 51, no. 17, p. 172001, Aug. 2018.
- [5] P. Dombi *et al.*, "Strong-field nano-optics," *Rev. Mod. Phys.*, vol. 92, no. 2, p. 025003, Jun. 2020.
- [6] P. Zhang and Y. Y. Lau, "Ultrafast strong-field photoelectron emission from biased metal surfaces: exact solution to time-dependent Schrödinger Equation," *Scientific Reports*, vol. 6, no. 1, p. 19894, Jan. 2016.
- [7] P. Hommelhoff, C. Kealhofer, and M. A. Kasevich, "Ultrafast Electron Pulses from a Tungsten Tip Triggered by Low-Power Femtosecond Laser Pulses," *Phys. Rev. Lett.*, vol. 97, no. 24, p. 247402, Dec. 2006.
- [8] P. Hommelhoff, Y. Sortais, A. Aghajani-Talesh, and M. A. Kasevich, "Field Emission Tip as a Nanometer Source of Free Electron Femtosecond Pulses," *Phys. Rev. Lett.*, vol. 96, no. 7, p. 077401, Feb. 2006.
- [9] C. Ropers, D. R. Solli, C. P. Schulz, C. Lienau, and T. Elsaesser, "Localized Multiphoton Emission of Femtosecond Electron Pulses from Metal Nanotips," *Phys. Rev. Lett.*, vol. 98, no. 4, p. 043907, Jan. 2007.
- [10] R. Ganter *et al.*, "Laser-Photofield Emission from Needle Cathodes for Low-Emittance Electron Beams," *Phys. Rev. Lett.*, vol. 100, no. 6, p. 064801, Feb. 2008.
- [11] R. Bormann, M. Gulde, A. Weismann, S. V. Yalunin, and C. Ropers, "Tip-Enhanced Strong-Field Photoemission," *Phys. Rev. Lett.*, vol. 105, no. 14, p. 147601, Sep. 2010.

- [12] M. Schenk, M. Krüger, and P. Hommelhoff, "Strong-Field Above-Threshold Photoemission from Sharp Metal Tips," *Phys. Rev. Lett.*, vol. 105, no. 25, p. 257601, Dec. 2010.
- [13] M. Krüger, M. Schenk, and P. Hommelhoff, "Attosecond control of electrons emitted from a nanoscale metal tip," *Nature*, vol. 475, no. 7354, pp. 78–81, Jul. 2011.
- [14] G. Herink, D. R. Solli, M. Gulde, and C. Ropers, "Field-driven photoemission from nanostructures quenches the quiver motion," *Nature*, vol. 483, no. 7388, pp. 190–193, Mar. 2012.
- [15] L. Wimmer, G. Herink, D. R. Solli, S. V. Yalunin, K. E. Echternkamp, and C. Ropers, "Terahertz control of nanotip photoemission," *Nature Physics*, vol. 10, no. 6, pp. 432–436, Jun. 2014.
- [16] F. Kusa, K. E. Echternkamp, G. Herink, C. Ropers, and S. Ashihara, "Optical field emission from resonant gold nanorods driven by femtosecond mid-infrared pulses," *AIP Advances*, vol. 5, no. 7, p. 077138, Jul. 2015.
- [17] T. Rybka, M. Ludwig, M. F. Schmalz, V. Knittel, D. Brida, and A. Leitenstorfer, "Sub-cycle optical phase control of nanotunnelling in the single-electron regime," *Nature Photonics*, vol. 10, no. 10, pp. 667–670, Oct. 2016.
- [18] C. Li *et al.*, "Carbon Nanotubes as an Ultrafast Emitter with a Narrow Energy Spread at Optical Frequency," *Advanced Materials*, vol. 29, no. 30, p. 1701580, 2017.
- [19] W. P. Putnam, R. G. Hobbs, P. D. Keathley, K. K. Berggren, and F. X. Kärtner, "Optical-field-controlled photoemission from plasmonic nanoparticles," *Nature Physics*, vol. 13, no. 4, pp. 335–339, Apr. 2017.
- [20] P. Rácz *et al.*, "Measurement of Nanoplasmonic Field Enhancement with Ultrafast Photoemission," *Nano Lett.*, vol. 17, no. 2, pp. 1181–1186, Feb. 2017.
- [21] M. Sivis, N. Pazos-Perez, R. Yu, R. Alvarez-Puebla, F. J. García de Abajo, and C. Ropers, "Continuous-wave multiphoton photoemission from plasmonic nanostars," *Communications Physics*, vol. 1, no. 1, pp. 1–6, Apr. 2018.
- [22] C. Li *et al.*, "Extreme nonlinear strong-field photoemission from carbon nanotubes," *Nature Communications*, vol. 10, no. 1, p. 4891, Oct. 2019.
- [23] M. Ludwig *et al.*, "Sub-femtosecond electron transport in a nanoscale gap," *Nature Physics*, vol. 16, no. 3, pp. 341–345, Mar. 2020.
- [24] S. Berweger, J. M. Atkin, R. L. Olmon, and M. B. Raschke, "Adiabatic Tip-Plasmon Focusing for Nano-Raman Spectroscopy," *J. Phys. Chem. Lett.*, vol. 1, no. 24, pp. 3427–3432, Dec. 2010.

- [25] S. Berweger, J. M. Atkin, X. G. Xu, R. L. Olmon, and M. B. Raschke, "Femtosecond Nanofocusing with Full Optical Waveform Control," *Nano Lett.*, vol. 11, no. 10, pp. 4309– 4313, Oct. 2011.
- [26] M. Müller, A. Paarmann, and R. Ernstorfer, "Femtosecond electrons probing currents and atomic structure in nanomaterials," *Nature Communications*, vol. 5, no. 1, p. 5292, Oct. 2014.
- [27] S. Sun *et al.*, "Direct imaging of plasma waves using ultrafast electron microscopy," *Structural Dynamics*, vol. 7, no. 6, p. 064301, Nov. 2020.
- [28] D. Ehberger *et al.*, "Highly Coherent Electron Beam from a Laser-Triggered Tungsten Needle Tip," *Phys. Rev. Lett.*, vol. 114, no. 22, p. 227601, Jun. 2015.
- [29] B. Schröder, M. Sivis, R. Bormann, S. Schäfer, and C. Ropers, "An ultrafast nanotip electron gun triggered by grating-coupled surface plasmons," *Appl. Phys. Lett.*, vol. 107, no. 23, p. 231105, Dec. 2015.
- [30] E. Jones, M. Becker, J. Luiten, and H. Batelaan, "Laser control of electron matter waves," *Laser & Photonics Reviews*, vol. 10, no. 2, pp. 214–229, 2016.
- [31] E. Forati, T. J. Dill, A. R. Tao, and D. Sievenpiper, "Photoemission-based microelectronic devices," *Nature Communications*, vol. 7, no. 1, p. 13399, Nov. 2016.
- [32] P. Zhang and Y. Y. Lau, "Ultrafast and nanoscale diodes," *Journal of Plasma Physics*, vol. 82, no. 5, Oct. 2016.
- [33] J. Lin, P. Y. Wong, P. Yang, Y. Y. Lau, W. Tang, and P. Zhang, "Electric field distribution and current emission in a miniaturized geometrical diode," *Journal of Applied Physics*, vol. 121, no. 24, p. 244301, Jun. 2017.
- [34] P. Zhang, A. Valfells, L. K. Ang, J. W. Luginsland, and Y. Y. Lau, "100 years of the physics of diodes," *Applied Physics Reviews*, vol. 4, no. 1, p. 011304, Mar. 2017.
- [35] E. Forati and D. Sievenpiper, "Electron emission by long and short wavelength lasers: Essentials for the design of plasmonic photocathodes," *Journal of Applied Physics*, vol. 124, no. 8, p. 083101, Aug. 2018.
- [36] P. Zhang, Y. S. Ang, A. L. Garner, Á. Valfells, J. W. Luginsland, and L. K. Ang, "Space-charge limited current in nanodiodes: Ballistic, collisional, and dynamical effects," *Journal of Applied Physics*, vol. 129, no. 10, p. 100902, Mar. 2021.
- [37] X. Xiong *et al.*, "Plasmon-Enhanced Resonant Photoemission Using Atomically Thick Dielectric Coatings," *ACS Nano*, vol. 14, no. 7, pp. 8806–8815, Jul. 2020.
- [38] K. L. Jensen, "Field emitter arrays for plasma and microwave source applications," *Physics of Plasmas*, vol. 6, no. 5, pp. 2241–2253, Apr. 1999.

- [39]D. Shiffler *et al.*, "Emission uniformity and emission area of explosive field emission cathodes," *Appl. Phys. Lett.*, vol. 79, no. 18, pp. 2871–2873, Oct. 2001.
- [40] R. J. Barker, N. C. Luhmann, J. H. Booske, and G. S. Nusinovich, "HighPower Microwave Sources," in *Modern Microwave and Millimeter-Wave Power Electronics*, IEEE, 2005, pp. 691–730.
- [41] W. Tang, D. Shiffler, K. Golby, M. LaCour, and T. Knowles, "Field enhancement for fiber emitters in linear and rectangular arrays," *Journal of Vacuum Science & Technology B*, vol. 32, no. 5, p. 052202, Aug. 2014.
- [42] P. Zhang, S. B. Fairchild, T. C. Back, and Y. Luo, "Field emission from carbon nanotube fibers in varying anode-cathode gap with the consideration of contact resistance," *AIP Advances*, vol. 7, no. 12, p. 125203, Dec. 2017.
- [43] P. Zhang *et al.*, "Temperature Comparison of Looped and Vertical Carbon Nanotube Fibers during Field Emission," *Applied Sciences*, vol. 8, no. 7, p. 1175, Jul. 2018.
- [44] S. B. Fairchild *et al.*, "Carbon Nanotube Fiber Field Emission Array Cathodes," *IEEE Transactions on Plasma Science*, vol. 47, no. 5, pp. 2032–2038, May 2019.
- [45] P. Wong, P. Zhang, and J. Luginsland, "Recent theory of traveling-wave tubes: a tutorial-review," *Plasma Res. Express*, vol. 2, no. 2, p. 023001, Jun. 2020.
- [46] H. Yanagisawa *et al.*, "Delayed electron emission in strong-field driven tunnelling from a metallic nanotip in the multi-electron regime," *Scientific Reports*, vol. 6, no. 1, p. 35877, Oct. 2016.
- [47] P. M. Nagel *et al.*, "Surface plasmon assisted electron acceleration in photoemission from gold nanopillars," *Chemical Physics*, vol. 414, pp. 106–111, Mar. 2013.
- [48] J. Vogelsang *et al.*, "Ultrafast Electron Emission from a Sharp Metal Nanotaper Driven by Adiabatic Nanofocusing of Surface Plasmons," *Nano Lett.*, vol. 15, no. 7, pp. 4685–4691, Jul. 2015.
- [49] P. Dombi *et al.*, "Ultrafast Strong-Field Photoemission from Plasmonic Nanoparticles," *Nano Lett.*, vol. 13, no. 2, pp. 674–678, Feb. 2013.
- [50] R. G. Hobbs *et al.*, "High-Yield, Ultrafast, Surface Plasmon-Enhanced, Au Nanorod Optical Field Electron Emitter Arrays," *ACS Nano*, vol. 8, no. 11, pp. 11474–11482, Nov. 2014.
- [51] M. E. Swanwick *et al.*, "Nanostructured Ultrafast Silicon-Tip Optical Field-Emitter Arrays," *Nano Lett.*, vol. 14, no. 9, pp. 5035–5043, Sep. 2014.
- [52] H. Yanagisawa *et al.*, "Optical Control of Field-Emission Sites by Femtosecond Laser Pulses," *Phys. Rev. Lett.*, vol. 103, no. 25, p. 257603, Dec. 2009.

- [53] H. Yanagisawa *et al.*, "Laser-induced field emission from a tungsten tip: Optical control of emission sites and the emission process," *Phys. Rev. B*, vol. 81, no. 11, p. 115429, Mar. 2010.
- [54] B. Piglosiewicz *et al.*, "Carrier-envelope phase effects on the strong-field photoemission of electrons from metallic nanostructures," *Nature Photonics*, vol. 8, no. 1, pp. 37–42, Jan. 2014.
- [55] P. D. Keathley *et al.*, "Vanishing carrier-envelope-phase-sensitive response in optical-field photoemission from plasmonic nanoantennas," *Nature Physics*, vol. 15, no. 11, pp. 1128–1133, Nov. 2019.
- [56] Y. Luo, Y. Zhou, and P. Zhang, "Few-cycle optical-field-induced photoemission from biased surfaces: An exact quantum theory," *Phys. Rev. B*, vol. 103, no. 8, p. 085410, Feb. 2021.
- [57] M. Förster *et al.*, "Two-Color Coherent Control of Femtosecond Above-Threshold Photoemission from a Tungsten Nanotip," *Phys. Rev. Lett.*, vol. 117, no. 21, p. 217601, Nov. 2016.
- [58] W. C.-W. Huang, M. Becker, J. Beck, and H. Batelaan, "Two-color multiphoton emission from nanotips," *New J. Phys.*, vol. 19, no. 2, p. 023011, Feb. 2017.
- [59] T. Paschen *et al.*, "High visibility in two-color above-threshold photoemission from tungsten nanotips in a coherent control scheme," *Journal of Modern Optics*, vol. 64, no. 10–11, pp. 1054–1060, Jun. 2017.
- [60] L. Seiffert, T. Paschen, P. Hommelhoff, and T. Fennel, "High-order above-threshold photoemission from nanotips controlled with two-color laser fields," *J. Phys. B: At. Mol. Opt. Phys.*, vol. 51, no. 13, p. 134001, May 2018.
- [61] Y. Luo and P. Zhang, "Ultrafast strong-field photoelectron emission due to two-color laser fields," *Phys. Rev. B*, vol. 98, no. 16, p. 165442, Oct. 2018.
- [62] Y. Luo and P. Zhang, "Analysis of two-color laser-induced electron emission from a biased metal surface using an exact quantum mechanical solution," *Phys. Rev. Applied*, vol. 12, no. 4, p. 044056, Oct. 2019.
- [63] T. Higuchi, L. Maisenbacher, A. Liehl, P. Dombi, and P. Hommelhoff, "A nanoscale vacuum-tube diode triggered by few-cycle laser pulses," *Appl. Phys. Lett.*, vol. 106, no. 5, p. 051109, Feb. 2015.
- [64] M. Ludwig *et al.*, "Active control of ultrafast electron dynamics in plasmonic gaps using an applied bias," *Phys. Rev. B*, vol. 101, no. 24, p. 241412, Jun. 2020.
- [65] D. R. Ward, F. Hüser, F. Pauly, J. C. Cuevas, and D. Natelson, "Optical rectification and field enhancement in a plasmonic nanogap," *Nature Nanotechnology*, vol. 5, no. 10, pp. 732–736, Oct. 2010.

- [66] M. Turchetti *et al.*, "Impact of DC bias on weak optical-field-driven electron emission in nanovacuum-gap detectors," *J. Opt. Soc. Am. B, JOSAB*, vol. 38, no. 3, pp. 1009–1016, Mar. 2021.
- [67] L. V. Keldysh, "Ionization in the field of a strong electromagnetic wave," Sov. Phys. JETP, vol 20, no. 5, pp. 1307-1314, May 1964.
- [68] R. H. Fowler, "The Analysis of Photoelectric Sensitivity Curves for Clean Metals at Various Temperatures," *Phys. Rev.*, vol. 38, no. 1, pp. 45–56, Jul. 1931.
- [69] L. A. DuBridge, "A Further Experimental Test of Fowler's Theory of Photoelectric Emission," *Phys. Rev.*, vol. 39, no. 1, pp. 108–118, Jan. 1932.
- [70] L. A. DuBridge, "Theory of the Energy Distribution of Photoelectrons," *Phys. Rev.*, vol. 43, no. 9, pp. 727–741, May 1933.
- [71] J. H. Bechtel, W. L. Smith, and N. Bloembergen, "Four-photon photoemission from tungsten," *Optics Communications*, vol. 13, no. 1, pp. 56–59, Jan. 1975.
- [72] D. H. Dowell, F. K. King, R. E. Kirby, J. F. Schmerge, and J. M. Smedley, "In situ cleaning of metal cathodes using a hydrogen ion beam," *Phys. Rev. ST Accel. Beams*, vol. 9, no. 6, p. 063502, Jun. 2006.
- [73] D. H. Dowell and J. F. Schmerge, "Quantum efficiency and thermal emittance of metal photocathodes," *Phys. Rev. ST Accel. Beams*, vol. 12, no. 7, p. 074201, Jul. 2009.
- [74] Y. Zhou and P. Zhang, "A quantum model for photoemission from metal surfaces and its comparison with the three-step model and Fowler–DuBridge model," *Journal of Applied Physics*, vol. 127, no. 16, p. 164903, Apr. 2020.
- [75] H. R. Reiss, "Effect of an intense electromagnetic field on a weakly bound system," *Phys. Rev. A*, vol. 22, no. 5, pp. 1786–1813, Nov. 1980.
- [76] S. V. Yalunin, M. Gulde, and C. Ropers, "Strong-field photoemission from surfaces: Theoretical approaches," *Phys. Rev. B*, vol. 84, no. 19, p. 195426, Nov. 2011.
- [77] F. H. M. Faisal, J. Z. Kamiński, and E. Saczuk, "Photoemission and high-order harmonic generation from solid surfaces in intense laser fields," *Phys. Rev. A*, vol. 72, no. 2, p. 023412, Aug. 2005.
- [78] S. V. Yalunin *et al.*, "Field localization and rescattering in tip-enhanced photoemission," *Annalen der Physik*, vol. 525, no. 1–2, pp. L12–L18, 2013.
- [79] M. Pant and L. K. Ang, "Ultrafast laser-induced electron emission from multiphoton to optical tunneling," *Phys. Rev. B*, vol. 86, no. 4, p. 045423, Jul. 2012.

- [80] J. Li and U. Thumm, "Semiclassical approach for solving the time-dependent Schr\"odinger equation in spatially inhomogeneous electromagnetic pulses," *Phys. Rev. A*, vol. 101, no. 1, p. 013411, Jan. 2020.
- [81] R. H. Fowler and L. Nordheim, "Electron emission in intense electric fields," *Proceedings of the Royal Society of London. Series A, Containing Papers of a Mathematical and Physical Character*, vol. 119, no. 781, pp. 173–181, May 1928.
- [82] L. W. Nordhiem and R. H. Fowler, "The effect of the image force on the emission and reflexion of electrons by metals," *Proceedings of the Royal Society of London. Series A, Containing Papers of a Mathematical and Physical Character*, vol. 121, no. 788, pp. 626–639, Dec. 1928.
- [83] B. Barwick, C. Corder, J. Strohaber, N. Chandler-Smith, C. Uiterwaal, and H. Batelaan, "Laser-induced ultrafast electron emission from a field emission tip," *New J. Phys.*, vol. 9, no. 5, p. 142, May 2007.
- [84] K. E. Priebe *et al.*, "Attosecond electron pulse trains and quantum state reconstruction in ultrafast transmission electron microscopy," *Nature Photonics*, vol. 11, no. 12, pp. 793–797, Dec. 2017.
- [85] B. Ji *et al.*, "Two-color multiphoton emission for comprehensive reveal of ultrafast plasmonic field distribution," *New J. Phys.*, vol. 20, no. 7, p. 073031, Jul. 2018.
- [86] J. W. Gadzuk and E. W. Plummer, "Field Emission Energy Distribution (FEED)," *Rev. Mod. Phys.*, vol. 45, no. 3, pp. 487–548, Jul. 1973.
- [87] P. Zhang, "Scaling for quantum tunneling current in nano- and subnano-scale plasmonic junctions," *Scientific Reports*, vol. 5, no. 1, p. 9826, May 2015.
- [88] A. Chatziafratis, G. Fikioris, and J. P. Xanthakis, "Exact eigenstates of a nanometric paraboloidal emitter and field emission quantities," *Proceedings of the Royal Society A: Mathematical, Physical and Engineering Sciences*, vol. 474, no. 2214, p. 20170692, Jun. 2018.
- [89] R. Haight, "Electron dynamics at surfaces," *Surface Science Reports*, vol. 21, no. 8, pp. 275–325, Jan. 1995.
- [90] F. Reinert and S. Hüfner, "Photoemission spectroscopy—from early days to recent applications," *New J. Phys.*, vol. 7, pp. 97–97, Apr. 2005.
- [91] R. W. Schoenlein, J. G. Fujimoto, G. L. Eesley, and T. W. Capehart, "Femtosecond relaxation dynamics of image-potential states," *Phys. Rev. B*, vol. 43, no. 6, pp. 4688–4698, Feb. 1991.
- [92] M. Weinelt, "Time-resolved two-photon photoemission from metal surfaces," *J. Phys.: Condens. Matter*, vol. 14, no. 43, pp. R1099–R1141, Oct. 2002.

- [93] D. Friedrich, P. Sippel, O. Supplie, T. Hannappel, and R. Eichberger, "Two-Photon Photoemission Spectroscopy for Studying Energetics and Electron Dynamics at Semiconductor Interfaces," *physica status solidi* (a), vol. 216, no. 8, p. 1800738, 2019.
- [94] J. T. Holgate and M. Coppins, "Field-Induced and Thermal Electron Currents from Earthed Spherical Emitters," *Phys. Rev. Applied*, vol. 7, no. 4, p. 044019, Apr. 2017.
- [95] Y. Fu, J. Krek, P. Zhang, and J. P. Verboncoeur, "Evaluating microgap breakdown mode transition with electric field non-uniformity," *Plasma Sources Sci. Technol.*, vol. 27, no. 9, p. 095014, Sep. 2018.
- [96] M. Kildemo, S. Calatroni, and M. Taborelli, "Breakdown and field emission conditioning of Cu, Mo, and W," *Phys. Rev. ST Accel. Beams*, vol. 7, no. 9, p. 092003, Sep. 2004.
- [97] K. Yoshioka *et al.*, "Real-space coherent manipulation of electrons in a single tunnel junction by single-cycle terahertz electric fields," *Nature Photonics*, vol. 10, no. 12, pp. 762–765, Dec. 2016.
- [98] S. H. Jo, J. Y. Huang, S. Chen, G. Y. Xiong, D. Z. Wang, and Z. F. Ren, "Field emission of carbon nanotubes grown on carbon cloth," *Journal of Vacuum Science & Technology B: Microelectronics and Nanometer Structures Processing, Measurement, and Phenomena*, vol. 23, no. 6, pp. 2363–2368, Oct. 2005.
- [99] M. Reutzel, A. Li, and H. Petek, "Coherent Two-Dimensional Multiphoton Photoelectron Spectroscopy of Metal Surfaces," *Phys. Rev. X*, vol. 9, no. 1, p. 011044, Mar. 2019.
- [100] E. C. Welch, P. Zhang, F. Dollar, Z.-H. He, K. Krushelnick, and A. G. R. Thomas, "Time dependent Doppler shifts in high-order harmonic generation in intense laser interactions with solid density plasma and frequency chirped pulses," *Physics of Plasmas*, vol. 22, no. 5, p. 053104, May 2015.
- [101] P. Zhang and A. G. R. Thomas, "Enhancement of high-order harmonic generation in intense laser interactions with solid density plasma by multiple reflections and harmonic amplification," *Appl. Phys. Lett.*, vol. 106, no. 13, p. 131102, Mar. 2015.
- [102] A. L. Fymat, "Jones's Matrix Representation of Optical Instruments. I: Beam Splitters," *Appl. Opt.*, *AO*, vol. 10, no. 11, pp. 2499–2505, Nov. 1971.
- [103] A. Rizea, "Design technique for all-dielectric non-polarizing beam splitter plate," *Opto-Electronics Review*, vol. 20, no. 1, pp. 96–99, Mar. 2012.
- [104] A. Rizea and I. M. Popescu, "Design techniques for all-dielectric polarizing beam splitter cubes, under constrained situations," *Romanian Reports in Physics*, vol. 64, no. 2, pp. 482–491, 2012.

- [105] S. G. Kaplan and M. A. Quijada, "Chapter 4 Fourier Transform Methods," in *Experimental Methods in the Physical Sciences*, vol. 46, T. A. Germer, J. C. Zwinkels, and B. K. Tsai, Eds. Academic Press, 2014, pp. 97–141.
- [106] Y. Luo, J. Luginsland, and P. Zhang, "Interference modulation of photoemission from biased metal cathodes driven by two lasers of the same frequency," *AIP Advances*, vol. 10, no. 7, p. 075301, Jul. 2020.
- [107] H. B. Michaelson, "The work function of the elements and its periodicity," *Journal of Applied Physics*, vol. 48, no. 11, pp. 4729–4733, Nov. 1977.
- [108] S. Schilt and T. Südmeyer, "Carrier-Envelope Offset Stabilized Ultrafast Diode-Pumped Solid-State Lasers," *Applied Sciences*, vol. 5, no. 4, pp. 787–816, Dec. 2015.
- [109] M. Krüger, M. Schenk, P. Hommelhoff, G. Wachter, C. Lemell, and J. Burgdörfer, "Interaction of ultrashort laser pulses with metal nanotips: a model system for strong-field phenomena," *New J. Phys.*, vol. 14, no. 8, p. 085019, Aug. 2012.
- [110] U. De Giovannini, D. Varsano, M. A. L. Marques, H. Appel, E. K. U. Gross, and A. Rubio, "Ab initio angle- and energy-resolved photoelectron spectroscopy with time-dependent density-functional theory," *Phys. Rev. A*, vol. 85, no. 6, p. 062515, Jun. 2012.
- [111] J. Heimerl, T. Higuchi, M. Ammon, M. A. Schneider, and P. Hommelhoff, "Gap-size dependence of optical near fields in a variable nanoscale two-tip junction," *Phys. Rev. B*, vol. 101, no. 12, p. 125403, Mar. 2020.
- [112] D. C. Marinica, A. K. Kazansky, P. Nordlander, J. Aizpurua, and A. G. Borisov, "Quantum Plasmonics: Nonlinear Effects in the Field Enhancement of a Plasmonic Nanoparticle Dimer," *Nano Lett.*, vol. 12, no. 3, pp. 1333–1339, Mar. 2012.
- [113] W. Zhu *et al.*, "Quantum mechanical effects in plasmonic structures with subnanometre gaps," *Nature Communications*, vol. 7, no. 1, p. 11495, Jun. 2016.
- [114] L. Wu, H. Duan, P. Bai, M. Bosman, J. K. W. Yang, and E. Li, "Fowler–Nordheim Tunneling Induced Charge Transfer Plasmons between Nearly Touching Nanoparticles," *ACS Nano*, vol. 7, no. 1, pp. 707–716, Jan. 2013,.
- [115] Y. Zhou and P. Zhang, "Theory of field emission from dielectric coated surfaces," *Phys. Rev. Research*, vol. 2, no. 4, p. 043439, Dec. 2020.
- [116] K. L. Jensen *et al.*, "A photoemission moments model using density functional and transfer matrix methods applied to coating layers on surfaces: Theory," *Journal of Applied Physics*, vol. 123, no. 4, p. 045301, Jan. 2018.
- [117] W. S. Truscott, "Wave functions in the presence of a time-dependent field: Exact solutions and their application to tunneling," *Phys. Rev. Lett.*, vol. 70, no. 13, pp. 1900–1903, Mar. 1993.

- [118] M. L. Goldberger and K. M. Watson, *Collision Theory*, 1st Edition. New York, N.Y.: John Wiley and Sons, 1964.
- [119] I. Adawi, "Theory of the Surface Photoelectric Effect for One and Two Photons," *Phys. Rev.*, vol. 134, no. 3A, pp. A788–A798, May 1964.
- [120] D. Novko, V. Despoja, M. Reutzel, A. Li, H. Petek, and B. Gumhalter, "Plasmonically assisted channels of photoemission from metals," *Phys. Rev. B*, vol. 103, no. 20, p. 205401, May 2021.